Engineering Materials

Ford Lumban Gaol
Jeffrey Webb *Editors*

Recent Trends in Nanotechnology and Materials Science

Selected Review Papers from the 2013 International Conference on Manufacturing, Optimization, Industrial and Material Engineering (MOIME 2013)

Springer

Engineering Materials

For further volumes:
http://www.springer.com/series/4288

Ford Lumban Gaol · Jeffrey Webb
Editors

Recent Trends in Nanotechnology and Materials Science

Selected Review Papers from the 2013 International Conference on Manufacturing, Optimization, Industrial and Material Engineering (MOIME 2013)

Springer

Editors
Ford Lumban Gaol
Bina Nusantara University
Jakarta
Indonesia

Jeffrey Webb
Department of Mechanical, Materials and Manufacturing Engineering
The University of Nottingham Malaysia Campus
Semenyih, Selangor
Malaysia

ISSN 1612-1317 ISSN 1868-1212 (electronic)
ISBN 978-3-319-04515-3 ISBN 978-3-319-04516-0 (eBook)
DOI 10.1007/978-3-319-04516-0
Springer Cham Heidelberg New York Dordrecht London

Library of Congress Control Number: 2014939054

Printed on acid-free paper

Springer is part of Springer Science+Business Media (www.springer.com)

Preface

Nanotechnology and materials science are becoming increasingly important in the modern world. This book presents eight selected reviews from the 2013 international conference on Manufacturing, Optimization, Industrial and Material Engineering, held in Bandung, Indonesia, from 9 to 10 March 2013. The chapters focus on new advances and research results in the fields of Nanotechnology and Materials Science. The reviews were selected for their high quality and in order to cover a range representative of the conference themes; the selected areas mainly concern experimental studies, characterization, and synthesis of micro- and nanoscale materials, studies of their properties, and how they relate to various applications.

The following topics are covered: Surface hardness and wear resistance of carbon steel related to the surface microstructure; ZnO/SnO2 nanocomposites prepared on ZnO coated glass using chemical vapor deposition with applications in humidity sensing; nano-magnesium oxide synthesis: the effect of MgO nano-filler loading on the dielectric layer properties of nano-MgO films; production of nanozeolite by wet milling: a study of their advantages over conventional micron-sized materials; the performance of solid-state dye sensitized solar cells fabricated from CuI thin films deposited using a novel mist-atomization method; impedance tube sound absorption measurements on date palm fiber panels made from the natural waste of date palms; work hardening and tensile strength properties in AZ31 and AZ61 Al-Zn magnesium alloys investigated with quasi-static tensile tests at various strain rates; nanomechanical surface properties of stainless steel, investigated using field emission scanning electron microscopy, universal scanning probe microscopy, and nanoindentation.

These articles will provide a good source of reference material and new ideas for those working in these areas and encourage further exploration. They will also be useful to newcomers to these fields who wish to be informed of some of the latest developments.

Contents

Contributors

S. Abdullah Faculty of Applied Sciences, Universiti Teknologi MARA (UiTM), Shah Alam, Selangor, Malaysia

N. Abdul Latif Department of Mechanical and Materials Engineering, Faculty of Engineering and Built Environment, Universiti Kebangsaan Malaysia, Bangi, Selangor DE, Malaysia; Department of Mechanics, Faculty of Mechanical and Manufacturing Engineering, Universiti Tun Hussein Onn Malaysia, Parit Raja, Johor, Malaysia

M. N. Amalina Faculty of Electrical Engineering, NANO-ElecTronic Centre (NET), Universiti Teknologi MARA (UiTM), Shah Alam, Selangor, Malaysia

Silvia Anggraeni Universiti Teknologi PETRONAS, Tronoh, Malaysia

Raudah Abu Bakar Faculty of Electrical Engineering, NANO-ElecTronic Centre (NET), Universiti Teknologi MARA, Shah Alam, Malaysia

M. Z. Borhan NANO-SciTech Centre Institute of Science, Universiti Teknologi MARA (UiTM), Shah Alam, Selangor, Malaysia; Faculty of Applied Sciences, Universiti Teknologi MARA (UiTM), Shah Alam, Selangor, Malaysia

A. K. Elwaleed Institute of Space Science, Universiti Kebangsaan Malaysia, Bangi, Selangor DE, Malaysia

Patthi Husain Universiti Teknologi PETRONAS, Tronoh, Malaysia

Mokhtar Ismail Universiti Teknologi PETRONAS, Tronoh, Malaysia

Mohamad Rusop Mahmood Faculty of Electrical Engineering, NANO-Elec-Tronic Centre (NET), Universiti Teknologi MARA, Shah Alam, Malaysia

M. H. Mamat Faculty of Electrical Engineering, NANO-ElecTronic Centre (NET), Shah Alam, Selangor, Malaysia

N. D. Md Sin Faculty of Electrical Engineering, NANO-ElecTronic Centre (NET), Shah Alam, Selangor, Malaysia

N. Z. F. Mukhtar NANO-SciTech Centre Institute of Science, Universiti Teknologi MARA (UiTM), Shah Alam, Selangor, Malaysia; Faculty of Applied Sciences, Universiti Teknologi MARA (UiTM), Shah Alam, Selangor, Malaysia

Y. Mutoh Department of Mechanical Engineering, Nagaoka University of Technology, Nagaoka, Niigata, Japan

N. Nikabdullah Institute of Space Science, Universiti Kebangsaan Malaysia, Bangi, Selangor DE, Malaysia

M. J. M. Nor Department of Mechanical and Materials Engineering, Faculty of Engineering and Built Environment, Universiti Kebangsaan Malaysia, Bangi, Selangor DE, Malaysia

Adillah Nurasyikin NANO-ElecTronic Centre (NET), Faculty of Electrical Engineering, Universiti Teknologi MARA, Shah Alam, Malaysia

Lyly Nyl NANO-ElecTronic Centre (NET), Faculty of Electrical Engineering, Universiti Teknologi MARA, Shah Alam, Malaysia

M. Rusop Faculty of Electrical Engineering, NANO-ElecTronic Centre (NET), Shah Alam, Selangor, Malaysia; NANO-Scitech Centre (NST), Institute of Science, Universiti Teknologi MARA (UiTM), Shah Alam, Selangor, Malaysia

Z. Sajuri Department of Mechanical and Materials Engineering, Faculty of Engineering and Built Environment, Universiti Kebangsaan Malaysia, Bangi, Selangor DE, Malaysia

J. Syarif Department of Mechanical and Materials Engineering, Faculty of Engineering and Built Environment, Universiti Kebangsaan Malaysia, Bangi, Selangor DE, Malaysia

Mohamad Fadzil Tahar Faculty of Electrical Engineering, NANO-ElecTronic Centre (NET), Shah Alam, Selangor, Malaysia

M. F. M. Tahir Department of Mechanical and Materials Engineering, Faculty of Engineering and Built Environment, Universiti Kebangsaan Malaysia, Bangi, Selangor DE, Malaysia

Askar Triwiyanto Universiti Teknologi PETRONAS, Tronoh, Malaysia

Habibah Zulkefle NANO-ElecTronic Centre (NET), Faculty of Electrical Engineering, Universiti Teknologi MARA, Shah Alam, Malaysia

R. Zulkifli Department of Mechanical and Materials Engineering, Faculty of Engineering and Built Environment, Universiti Kebangsaan Malaysia, Bangi, Selangor DE, Malaysia

Improving the Surface Hardness and Wear Resistance of S45C Carbon Steel *Via* Various Heat Treatments and pH Values of Electroless Ni-P Deposition

Shih-Hsien Chang, Chih-Chung Chang and Cheng Liang

Abstract This research focused on studying the effects of a surface microstructure on S45C carbon steel using different pH values of electroless Ni-P plating. Meanwhile, the authors make an effort to improve the surface hardness and wear resistance of S45C steels through various heat treatments. The experimental results show that the specimens using acid and alkaline baths of pH5 and pH8 resulted in maximum hardness; the hardness values were the $HV_{0.05}$ 701 and $HV_{0.05}$ 803, respectively. Moreover, pH5 and pH8 of Ni-P deposition after 350 and 300 °C and soaked for 1 h heat treatment, in which the highest hardness appeared, were $HV_{0.05}$ 1027 and $HV_{0.05}$ 1066, respectively. The specimens underwent the main precipitate phase of Ni_3P after heat treatment. Due to precipitation, strengthening of the Ni_3P phase increased the surface hardness of specimens after heat treatment; thus, the wear depth was decreased and wear resistance was enhanced. The optimal wear depth (2.738 μm) and (2.923 μm) appeared in Ni-P deposition by pH5 and pH8 after 350 and 300 °C and soaked for 1 h heat treatment, respectively.

1 Introduction

Electroless deposition is a variety of chemical deposition technology, involving the deposition of metals from solution onto surfaces without applying an external electric voltage and is thought to be the simplest and most economic method to finish steel, aluminum, copper, plastics, and many other materials [1]. Among the plating metals, electroless nickel has exhibited more popularity due to its excellent properties such as high hardness, wear and corrosion resistance and has attracted

S.-H. Chang (✉) · C.-C. Chang · C. Liang
Department of Materials and Mineral Resources Engineering,
National Taipei University of Technology, 1, Sec. 3, Chung-Hsiao E. Rd,
Taipei, 10608 Taiwan
e-mail: changsh@ntut.edu.tw

F. L. Gaol and J. Webb (eds.), *Recent Trends in Nanotechnology and Materials Science*, Engineering Materials, DOI: 10.1007/978-3-319-04516-0_1,

Table 1 Chemical composition of the S45C carbon steel (wt%)

C	Si	Mn	S	P	Fe
0.46	0.21	0.72	≦0.04	≦0.03	Bal.

extensive interests from the academe and the industry. Electroless Ni-P plating technique, as an effective surface treatment method, has been widely used in a variety of environments due to its excellent corrosion resistance. In recent years, electroless Ni-P plating technology has been used in steel industry [2, 3].

S45C carbon steel (S45C) has been widely used in industrial applications, such as crank shafts, gears, main spindles of machine tools, connecting rods, etc., because of its distinguished mechanical property [4, 5]. However, how to enhance the surface hardness and wear resistance for S45C is the object work in the industry. Several surface hardening of S45C have been carried out and discussed [6, 7]. The aim of this study was to evaluate surface microstructure, wear resistance, and optimal parameters of heat treatment of electroless Ni-P plating in regard to S45C carbon steel.

2 Experimental

In this study, JIS S45C carbon steel was used as a substrate, the specimen size is Ø36 × D5 mm; chemical compositions are listed in Table 1. S45C carbon steel is equivalent to SAE1045 and is widely used in mechanical parts and structural steel. In order to improve its microstructure and mechanical properties, S45C is oil quenched at 850 °C, tempered at 400 °C, and the tempering process is repeated twice to reach a hardness of $HV_{0.05}$ 421.

The processes involving electroless Ni-P deposition are described as follows. First, the substrate (S45C) is processed by grinding and polishing in order to finish the specimen surface and then is immersed in the acetone solution using an ultrasonic vibrator for 20 min; it is then cleaned and rinsed with deionized water. Second, it is immersed in 15 % hydrochloric acid for 20 min to remove the oxide film. It is cleaned and rinsed with deionized water again, allowing the electroless Ni-P plating to be performed. In this study, the plating bath is divided into an acid and alkaline bath (pH4, 5, 6, 8, 9, and 10); sulfuric acid and ammonia were used to adjust the pH value. The bath compositions, concentration and operational conditions are listed in Table 2.

In this study, all the specimens were plated with six different pH values of Ni-P deposition, and then used five different heat treatment temperatures (300, 350, 400, 450, 500 °C, and soaked for 1 h) to evaluate the effects on Ni-P deposition. The vacuum was kept 10^{-1} atmosphere and the heating rate was 10 °C min^{-1}. After completion of the heat treatment, the specimens were slowly cooled to room temperature in a furnace and then removed. In order to evaluate the improvement in surface hardness and wear resistance on S45C carbon steel via different pH

Table 2 Bath composition and operating conditions of S45C carbon steel by electroless Ni-P

Process	Bath composition	Concentration (g/L)	Condition
Acid bath	$NiSO_4 \cdot 6H2O$	30	84 ± 1 °C
	$NaH_2PO_2 \cdot H_2O$	15	1 h
	$Na2C4H4O_4 \cdot 6H_2O$	12	pH4, 5, 6
Alkaline bath	$NiSO_4 \cdot 6H_2O$	30	84 ± 1 °C
	$NaH_2PO_2 \cdot H_2O$	10	1 h
	$NaC_6H_5O_7 \cdot 2H_2O$	40	pH8, 9, 10

values and heat treatments of Ni-P deposition, hardness and wear tests, SEM XRD, and microstructure inspections were performed.

Microstructural features of the specimens were examined by scanning electron microscopy. Hardness of the specimens was measured by Vickers indenter (HV) with loading of 50 g, which complied with the ASTM E384-08a standard method. The wear resistance of specimens was evaluated in a ball-on-disk test. The wear parameters are: specimen size is Ø36 × D5 mm, diameter of Cr ball is 6 mm, axial load is 4.9 N, disc rotation is 100 rpm, sliding speed is 0.031 ms^{-1}, and total rotation is 3,000 revolutions. The coefficient of friction was obtained from POD-FM406 software and the wear depth was measured by α-step equipment (ET-4000A).

3 Results and Discussion

This study investigated the growth mechanism and effects of electroless Ni-P deposition under different pH values and heat treatments. As the pH value increases (pH4 → pH10), the surface morphology of the deposition will display a slight variation from more continuous and smooth into a larger gathering of precipitation. A cluster of rough surface particles is shown in Fig. 1a–f. H. Matsubara et al. [8] showed that the different pH values clearly affect the flatness of precipitate particles in Ni-P deposition. In this study, the initial plating of Ni-P deposition generated nuclear particles which dispersed on the S45C surface and then integrated the nuclear particles and small-scale clusters into the growing phenomenon. Many small-scale clusters contact with each other to produce a rough surface and uneven-continuous layers. It is agreed with the previous literatures [8−10]. SL Chow et al. [11] also indicated that phosphorus is present in the polycrystalline nickel by solid solution; therefore, the higher phosphorus content will affect the crystal structure, which is detrimental to the crystallization. Thus, the precipitate particles are more slowly grown. On the other hand, the lower phosphorus content will result in a larger grain size. In this study, the EDS analysis showed that the phosphorus content tends to decrease (from 8.74 wt% to 2.61 wt%) as the pH value increased.

Figure 1a–c shows the surface morphology of electroless Ni-P deposition by pH4, pH5, and pH6 baths. These depositions with higher phosphorus content thus

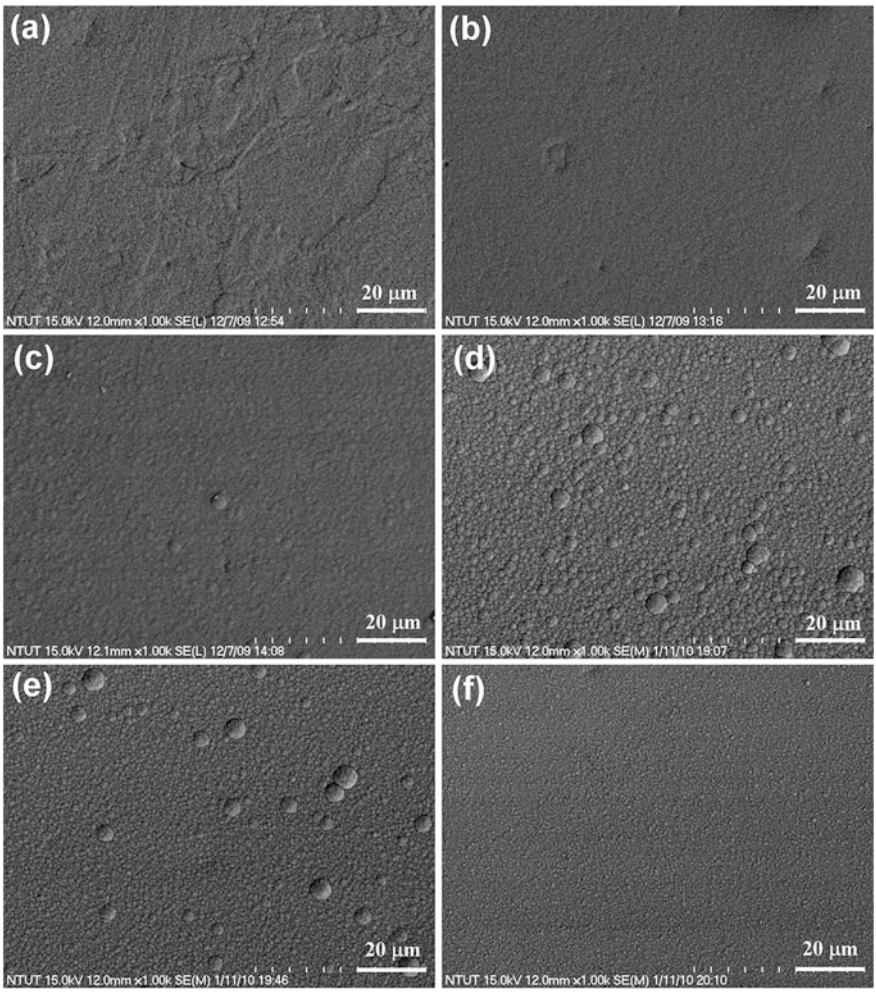

Fig. 1 SEM observation of surface morphology on the electroless Ni-P deposition by different pH values **a** pH4, **b** pH5, **c** pH6, **d** pH8, **e** pH9, **f** pH10

had undermined the original catalytic properties of nickel. Consequently, they can get a better dispersion of precipitation which is uniformly distributed in the S45C surface. As the pH value increases, the deposition shows lower phosphorus content. Figure 1d–f show the surface morphology of electroless Ni-P deposition in pH8, pH9, and pH10 baths, the lower phosphorus content of Ni-P deposition; they have a strong catalytic property which allows their precipitate particles to generate agglomeration and exhibit growth. Therefore, the precipitate particles of Ni-P deposition were larger and more obvious. The results can be further compared with the pH6 and pH9 baths; the catalytic properties of pH6 precipitate particles are detrimental to grain growth. The precipitate particles show slow continued growth

but generate more nuclear particles. Nuclear particles contact with each other and then form a smooth surface to make a continuous deposition, as shown in Fig. 1c. The precipitate particles of pH6 grow more slowly than does pH9. On the other hand, the precipitate particles of pH9 form many small agglomerations in the initial stage; the agglomeration continued to grow due to its catalytic property. Thus, the precipitate particles contact neighboring particles to form a continuous and rough surface of Ni-P deposition, as shown in Fig. 1e.

Figure 2 shows the SEM observation of the cross-section on the electroless Ni-P deposition by different pH values. Matsubara et al. [8] suggest that the pH value affects the deposition rate. Figure 2 represents the uniform deposition and thickness between the S45C and Ni-P layer. Meanwhile, the thickness of the Ni-P deposition seems to increase as the pH value increases (pH4 → pH5). Figure 2a shows the cross-section of Ni-P deposition by pH4; due to a higher content of phosphorus, the catalytic properties of nickel are poor and will result in a slower deposition rate and thinner deposition. By increasing the pH value, as shown in Fig. 2b–e, the phosphorus content was decreased and the catalytic properties of nickel were improved. As a result, we can get a much thicker layer. Furthermore, Fig. 2f shows the cross-section of Ni-P deposition by pH10; the pH value is too high to result in an adverse reaction and precipitation of the deposition. Since the pH value of bath is higher, it shows that the nickel ions cannot elicit a reduction. As the plating time increased, the ammonia of bath was evaporated, which resulted in the pH value descending. Therefore, it is one of the main factors causing the thickness of the Ni-P deposition to decrease. The deposition rate of Ni-P deposition by different pH values is shown in Fig. 3; the highest deposition rate of acid and alkaline baths appeared in pH5 (16.5 μmh^{-1}) and pH8 (15.0 μmh^{-1}), respectively. In this study, it is reasonable to suggest that the higher pH values (pH9 and pH10) were adverse reactions as was the precipitation of Ni-P deposition.

Table 3 shows the micro-hardness of non heat-treated and different heat treatment temperatures, of electroless Ni-P deposition. In this study, the hardness of substrate (S45C) was $HV_{0.05}$ 421. It was clearly shown that all of the hardness of the Ni-P deposition was higher than the substrate after electroless Ni-P deposition (non heat-treatment); both acid and alkaline plating of Ni-P deposition can enhance the hardness of the substrate. In the acid bath, the pH5 specimen has a higher level of hardness ($HV_{0.05}$ 701). Furthermore, compared to the alkaline bath, the pH8 specimen is highest; the hardness increases to $HV_{0.05}$ 803. In this study, the author's major concern was the microstructure and thickness of Ni-P deposition; thus, the heat treatment was performed. The hardness of Ni-P deposition was clearly enhanced after different heat treatments, as shown in Table 3. The highest levels of hardness ($HV_{0.05}$ 927) of pH4 and ($HV_{0.05}$ 1027) pH5 were 400 and 350 °C heat treatment, respectively. However, the increased temperature results in the hardness level decreasing; moreover, pH6, pH8, pH9, and pH10 layers can elicit the highest level of hardness after 300 °C, 1 h heat treatment. From above the test results, it is shown that the pH5 and pH8 of Ni-P deposition exhibit an optimal hardness, microstructure and deposition rate (Fig. 3); thus, we have selected them to perform further analysis, heat treatment and wear tests.

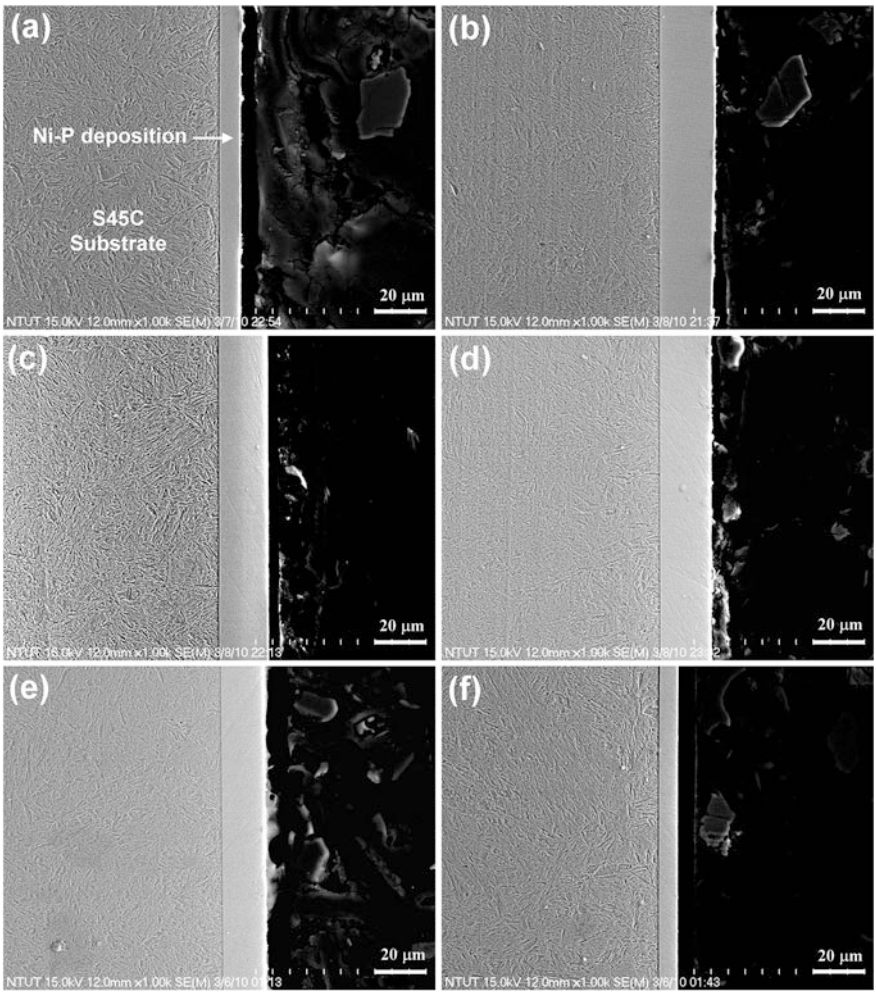

Fig. 2 SEM observation of crosses-section on the electroless Ni-P deposition by different pH values **a** pH4, **b** pH5, **c** pH6, **d** pH8, **e** pH9, **f** pH10

Figure 4 shows the SEM observation of surface morphology on the Ni-P deposition by pH5 after different heat treatments. The non heat-treated specimen represents a smoother deposition, as shown in Fig. 4a. With the heat treatment temperature increasing, the continuity of a smooth morphology will gradually transform into one that is rougher, with slightly increased agglomeration. When the temperature was raised to 350 °C, the particles contact each other, thus forming large areas of uneven surface, as shown in Fig. 4b. When the temperature rose to 400 °C, the agglomeration of particles made contact with each other, thus forming large areas of uneven surface, as shown in Fig. 4c. Moreover, when the

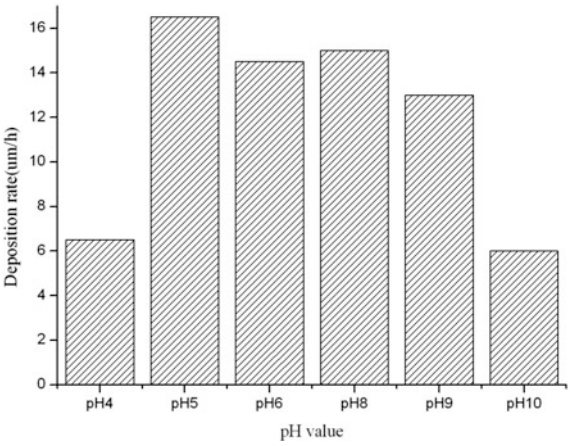

Fig. 3 Comparison of the deposition rate on Ni-P deposition by different pH values

Table 3 Compare the microhardness ($HV_{0.05}$) of non heat-treated and different heat treatment temperatures of electroless Ni-P deposition

pH value	4	5	6	8	9	10
Non heat-treated	539	701	690	803	766	700
300 °C	766	960	927	1066	986	816
350 °C	841	1027	845	960	933	549
400 °C	927	986	701	857	733	498
450 °C	713	917	623	711	644	426
500 °C	593	791	585	549	473	383

temperature was raised to 500 °C, the precipitate particles on the surface showed more obvious agglomeration and also become denser, as shown in Fig. 4d.

Figure 5 shows the SEM image of surface morphology on the Ni-P deposition by pH8 after different heat treatments. Due to the lower phosphorus content, the surface deposition is rougher and more uneven. When increasing the heat treatment temperature, the surface morphology changed minimally; there was a slight but noticeable difference at 300 °C, 1 h heat treatment. As shown in Fig. 5a and b, the particle size of precipitation shows a trend toward a smaller and denser outcome. With an increase in the heat treatment temperature (400 °C and above), the particle size of precipitation gradually became larger and more agglomerated, as shown in Fig. 5c and d. As compared with Figs. 4 and 5, the precipitate particles of pH8 Ni-P deposition appeared significantly larger in the surface structure after heat treatment.

Figure 6a shows the XRD pattern of electroless Ni-P deposition by different pH values. The initial plating of Ni-P deposition is amorphous and in coexistence with the microcrystalline structure of the nickel phase. The diffraction peak of nickel tends to increase as the pH value increases. The result agrees with the relevant literature (PS Kumar and PK Nair) [12]. Acidic plating of Ni-P deposition has relatively broad diffraction peaks; the higher phosphorus content results in lower

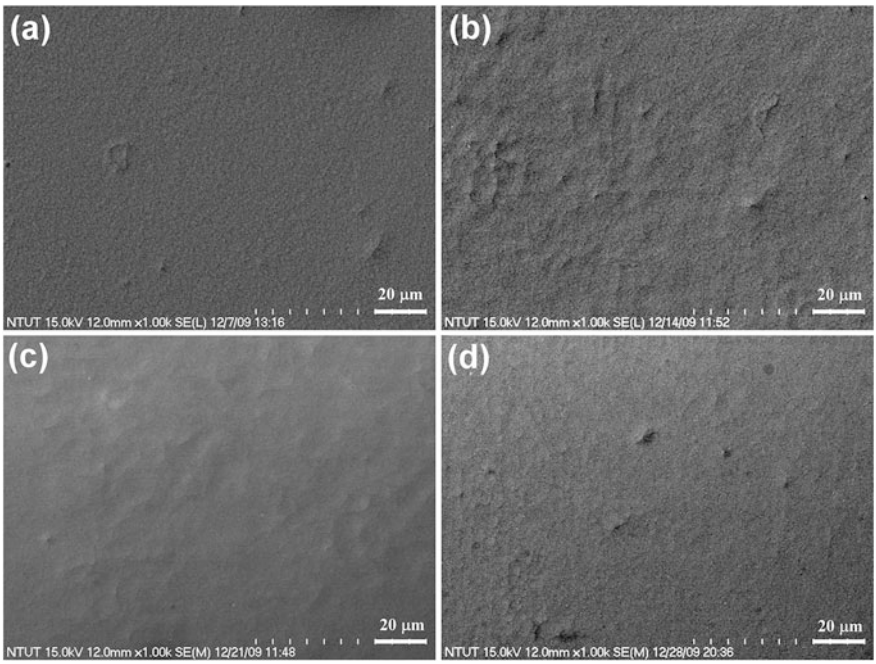

Fig. 4 SEM observation of surface morphology on the electroless Ni-P deposition by pH5 after different heat treatments **a** non heat-treated, **b** 350 °C, **c** 400 °C, **d** 500 °C

Ni diffraction peaks. However, the alkaline bath of Ni-P deposition has very clear diffraction peaks. As such, increasing the phosphorus content will produce a more disordered lattice. It is reasonable to suggest that the acidic plating of Ni-P deposition is closer to the amorphous structure, while the alkaline plating obtains better crystallization. In this study, Ni (111) plane is the main diffraction peak of electroless Ni-P deposition by different pH values.

Figure 6b and c show the XRD patterns of electroless Ni-P deposition by pH5 and pH8 after different heat treatments. It can be observed that the Ni-P deposition clearly generated phase transformation (Ni → Ni_3P) after heat treatment. With increasing temperatures, the Ni_3P phase will start to precipitate and grow. When the heat treatment temperature increased, Ni_3P began to precipitate. Finally, the Ni-P deposition produced the Ni crystalline phase in coexistence with Ni_3P precipitation. Figure 6b and c shows that the pH value increases and phosphorus content decreases; the crystallization of nickel was improved after heat treatment. In contrast, when the phosphorus content is high, the crystallization of the Ni_3P phase is better. XRD analysis indicated that two different kinds of structure were provided by the different pH values of electroless Ni-P deposition after heat treatment, namely, the crystalline structures of Ni and Ni_3P precipitations. It is agreed with the literature [13]. They belong to the Ni (111) plane, and (301) (231) (204), and (411) of the Ni_3P plane, respectively.

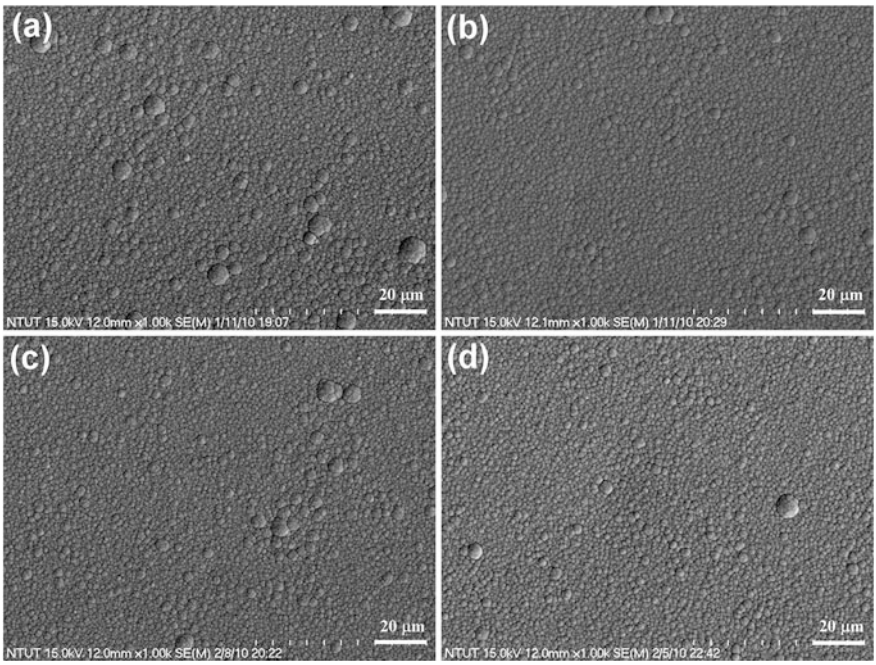

Fig. 5 SEM observation of surface morphology on the electroless Ni-P deposition by pH8 after different heat treatments **a** non heat-treated, **b** 300 °C, **c** 400 °C, **d** 500 °C

Figure 7 compares the coefficient of friction of electroless Ni-P deposition by pH5 and pH8 after different heat treatments. The substrate (S45C) has a low coefficient of friction at the beginning, but the coefficient of friction began to rise when the smooth surface was worn by the chrome ball. Conversely, the Ni-P depositions after heat treatments (pH5 350 and pH8 300 °C) have a higher coefficient of friction in the initial test but the coefficient of friction was decreased, began to change due to static friction, and maintained a stable value after sliding 25 m. Table 4 shows the average coefficient of friction and wear-depth of electroless Ni-P deposition by pH5 and pH8 at different heat treatment temperatures after the wear test. Most of the test results show that the sample with the higher level of hardness possesses a lower coefficient of friction and wear depth. The hardness of Ni-P deposition by pH5 ($HV_{0.05}$ 701) was lower than pH8 ($HV_{0.05}$ 803) after electroless treatment, but the pH5 has a lower coefficient of friction (0.357) instead. However, from the viewpoint of wear resistance, the pH8 of Ni-P deposition still has the lower wear depth (10.246 μm) because the oxygen atoms react with debris during the wear test and produce large amounts of oxide film. The oxide film has a lubricating effect, which will cause a lower coefficient of friction. As a result, the Ni-P deposition by pH5 plating has a better coefficient of friction than does the pH8, but lower hardness still results in weak wear resistance.

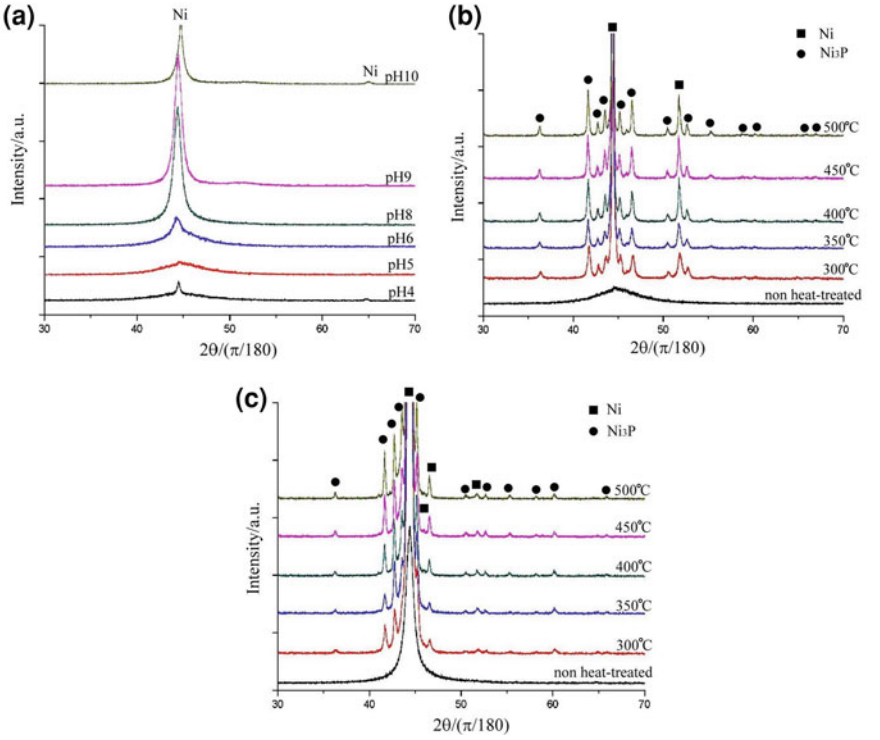

Fig. 6 XRD patterns of the electroless Ni-P deposition by different pH values **a** non heat-treated, **b** pH5 after different heat treatments, **c** pH8 after different heat treatments

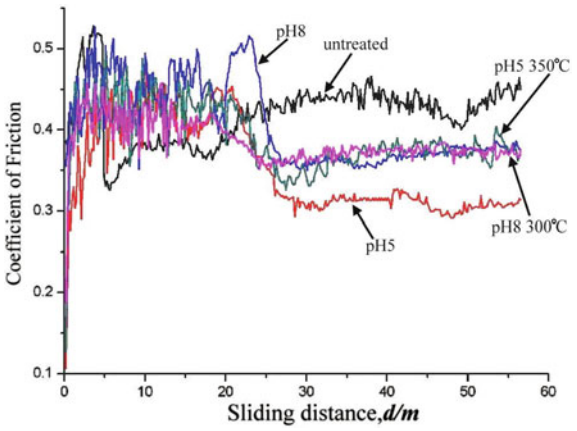

Fig. 7 Comparison of the coefficient of friction on electroless Ni-P deposition by pH5 and pH8 and different heat treatments

The average wear depth of the substrate was 5.429 μm, pH5 was 13.294 μm and pH8 was 10.246 μm after the wear test, respectively. Although the hardness of Ni-P deposition by pH5 and pH8 was higher than the substrate, the wear depth was

Table 4 Compare the average coefficient of friction and wear depth of electroless Ni-P deposition by pH5 and pH8, and different heat treatment temperatures after wear test

	Average coefficient of friction	Average wear depth (μm)
Un-treated (S45C)	0.433	5.429
pH5	0.357	13.294
pH8	0.408	10.246
pH5 350 °C	0.391	2.738
pH8 300 °C	0.385	2.923

deeper. Notably, the lubricating effect of the oxide film is a major concern. In addition, the heat treatment can improve the adhesion between the substrate and deposition. Regarding the specimens of Ni-P deposition by pH5 and pH8 after 350 and 300 °C and soaked for 1 h heat treatment, respectively, the hardness can be significantly improved so that it will result in the lower wear depth. The wear depths of pH5 and pH8 were 2.738 and 2.923 μm, respectively. These results can be further confirmed in Fig. 8a–e.

Figure 8a shows the wear morphology of un-treated S45C. Because the hardness (HRC 61) of the chrome ball is higher than the substrate, the S45C surface caused large areas of deep abrasive wear. It also can be found that the S45C produces large amounts of debris. Due to the chrome ball grinding and extrusion during the wear test, the debris of the substrate will bond the substrate together. Therefore, this generates adhesive wear. The arrow indicates the adhesive wear of S45C, as shown in Fig. 8a. The EDS analysis shows that the composition of the arrow area is 21.63 wt% O and 78.37 wt% Fe. The debris had a larger contact area with the air and frictional heat, leading to significant oxidation.

Figure 8b shows the wear morphology of Ni-P deposition by pH5. It is similar to Fig. 8a, and shows some of the adhesive wear. In addition to adhesive wear, the wear surface also exhibits some fine, long scratches. It is reasonable to suggest that in addition to the adhesive wear, some of the abrasive wear is also included. Figure 8c represents the wear morphology of Ni-P deposition by pH5 after 350 °C, 1 h heat treatment. Compared to Fig. 8b, it clearly shows shallow traces and better wear resistance. Figure 8d shows the wear morphology of Ni-P deposition by pH8. It represents significant adhesive wear. During the wear test, the grinding material will produce plastic deformation like a *bulge* phenomenon, as shown in Fig. 8b and d. Furthermore, with respect to the wear test, the *bulge* through the repetition of brittle deformation that will produce a hardening effect, eventually led to a rupture, as shown in Fig. 8b and d. In addition, Fig. 8e shows the wear morphology of Ni-P deposition by pH8 after 300 °C, 1 h heat treatment. Obviously, the wear resistance is better than that without heat treatment of pH8 Ni-P deposition. The wear mechanism included both abrasive and adhesive wear. According to the coefficient of friction and wear morphology analysis, it is reasonable to suggest that the best wear resistance appeared in the Ni-P deposition by pH5 and pH8 after 350 and 300 °C and soaked for 1 h heat treatment, respectively.

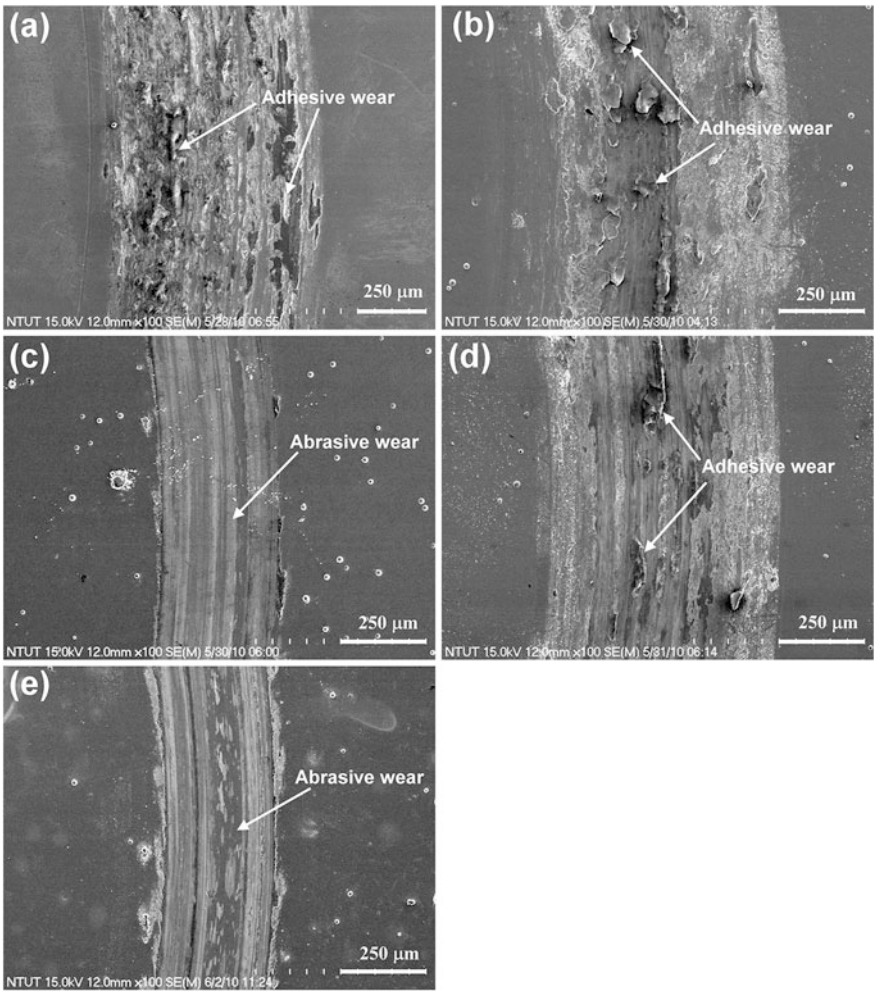

Fig. 8 SEM images of electroless Ni-P deposition by different pH values and heat treatments after 60 m of wear test **a** un-treated, **b** pH5, **c** pH5 and 350 °C heat treatment, **d** pH8, **e** pH8 and 300 °C heat treatment

4 Conclusions

XRD analysis shows that the S45C surface in the acidic plating easily generates close to the amorphous structure of deposition, and that in the alkaline plating of Ni-P deposition good crystallization was obtained. Furthermore, regardless of acid or alkaline bath of the Ni-P deposition, the S45C surface significantly occurs in the phase transformation after heat treatment, resulting in the precipitation of the Ni_3P phase.

In this study, the specimens used for the pH5 and pH8 of Ni-P depositions have an optimal hardness, structure and deposition rate. The higher level of hardness of acid bath is pH5 ($HV_{0.05}$ 701) and alkaline bath is pH8 ($HV_{0.05}$ 803) before heat treatment. Moreover, the maximum hardness ($HV_{0.05}$ 1027) of the specimen appeared in the pH5 Ni-P deposition through 350 °C, 1 h heat treatment, while the level of hardness treated with pH8 was $HV_{0.05}$ 1066 via 300 °C, 1 h heat treatment, respectively.

The optimal wear depth (2.738 μm) and (2.923 μm) appeared in Ni-P deposition by pH5 and pH8 after 350 and 300 °C and soaked for 1 h heat treatment, respectively; however, the untreated specimen shows the deeper (5.429 μm) level of wear morphology. Consequently, the surface hardness and wear resistance could be improvement by the electroless Ni-P deposition via suitable pH values and heat treatment.

References

1. Zhang, W.X., et al.: Electroless Ni-P layer with a chromium-free pretreatment on AZ91D magnesium alloy. Surf. Coat. Technol. **201**, 4594–4600 (2007)
2. Zhanga, H., et al.: Electroless Ni-P plating on Mg-10Li-1Zn alloy. J. Alloy. Compd. **474**, 306–310 (2009)
3. Elsentriecy, H.H., Azumi, K.: Electroless Ni-P deposition on AZ91 D magnesium alloy prepared by molybdate chemical conversion coatings electrochemical/chemical deposition and etching. J. Electrochem. Soc. **156**, D70–D77 (2009)
4. Yoo, Y.T., et al.: Welding characteristics of S45C medium carbon steel in laser welding process using a high power CW Nd: YAG laser. J. Mater. Sci. **396**, 117–6119 (2004)
5. Chino, Y., et al.: Mechanical and corrosion properties of a medium carbon steel (S45C) recycled by solid recycling process. J. Mater. Sci. Lett. **21**, 1695–1697 (2002)
6. Shin, H.J., et al.: Laser surface hardening of S45C medium carbon steel using ND: YAG laser with a continuous wave. J. Mater. Process. Technol. **187–188**, 467–470 (2007)
7. Lin, Y.C., Wang, S.W., Chen, T.M.: The observation of the nucleation and growth of electrolessly plated nickel deposited from different bath pH by TEM and QCM method. J. Mater. Process. Technol. **120**, 126–132 (2002)
8. Matsubara, H., et al.: The observation of the nucleation and growth of electrolessly plated nickel deposited from different bath pH by TEM and QCM method. Electrochim. Acta **52**, 402–407 (2006)
9. Homma, T., et al.: Tapping mode atomic force microscopy analysis of the growth process of electroless nickel-phosphorus films on nonconducting surfaces. J. Electrochem. Soc. **144**, 4123–4127 (1997)
10. Matsubara, H., et al.: Observation of initial deposition process of electroless nickel plating by quartz crystal microbalance method and microscopy. Electrochim. Acta **47**, 4011–4018 (2002)
11. Chow, S.L., Hedgecock, N.E., Schlesinger, M.: Electron microscope study of the nucleation and growth of electroless cobalt and nickel. J. Electrochem. Soc. **119**, 1614–1619 (1972)
12. Kumar, P.S., Nair, P.K.: Studies on crystallization of electroless Ni-P deposoits. J. Mater. Process. Technol. **56**, 511–520 (1996)
13. Wu, F.B., Li, J.J., Duh, J.G.: Evaluation of the mechanical properties and tribological behavior of the CrN coating deposited on mild steel modified with electroless Ni interlayer. Thin Solid Films **377–378**, 354–359 (2000)

Enhancement of Nanocomposite for Humidity Sensor Application

N. D. Md Sin, Mohamad Fadzil Tahar, M. H. Mamat and M. Rusop

Abstract This chapter investigates the improvement of nanocomposited ZnO/SnO_2 that was prepared on ZnO coated glass using thermal chemical vapor deposition (CVD). The sensor properties were characterized using current-voltage (*I–V*) measurement (Keithley 2400). The results analyzed were for ZnO agglomerate nanoparticle, SnO_2 nanorod, and ZnO/SnO_2 composite nanorods. The structural properties were characterized using field emission scanning electron microscopy (FESEM) (JEOL JSM 6701F). The thins films were tested using two-point probe and the sensors characterized using *I–V* measurement (Keithley 2400) in a clean humidity chamber (ESPEC SH-261). The chamber was set at the same room temperature (25 °C) with percent relative humidity (RH%) varied in the range of 40–90%RH. ZnO/SnO_2 composite nanorods performed the highest sensitivity with 265 ratio compared to the ZnO agglomerate nanoparticle and SnO_2 nanorod. The response and recovery time for ZnO/SnO_2 composite nanorods were 227 s and 34 s respectively.

1 Introduction

Humidity sensors have been important for the precise control and reliable estimate of water vapors content in atmospheres from industrial processes to the general improvement in the quality of life [1, 2]. Generally a humidity sensor has to possess fast response and recovery time, high sensitivity, good stability, negligible

N. D. Md Sin (✉) · M. F. Tahar · M. H. Mamat · M. Rusop
Faculty of Electrical Engineering, NANO-ElecTronic Centre (NET),
40450 Shah Alam, Selangor, Malaysia
e-mail: nordiyana86@yahoo.com

M. Rusop
NANO-Scitech Centre (NST), Institute of Science, Universiti Teknologi MARA (UiTM),
40450 Shah Alam, Selangor, Malaysia

F. L. Gaol and J. Webb (eds.), *Recent Trends in Nanotechnology and Materials Science*, Engineering Materials, DOI: 10.1007/978-3-319-04516-0_2,

hysteresis over periods of usage, and possibly a large operating range for both humidity and temperature [3]. As an *n*-type wide bandgap semiconductor (Eg = 3.6 eV) tin dioxide (SnO_2) nanostructures having rutile structure attracted great interest in recent years. SnO_2 has good characteristics in optical, electrical, chemical, and thermal stability [4]. ZnO is one of the most important group of II–VI semiconductor materials. It is an *n*-type and a wide bandgap material with a direct bandgap (3.37 eV) and large excitation binding energy of 60 MeV. ZnO also comes from Wurtzite-structured semiconductors that can help to mix with SnO_2 [5]. Zinc and tin compounds have recently attracted considerable attention because they display technological properties [6], such as high capacity anode material, which can also be used for oxygen separation acting as a photo catalyst under the visible light, humidity and gas sensors action [7, 8]. Doping is an attractive and effective method for manipulating various applications of semiconductors.

Using single materials can cause low sensitivity of sensor [9] due to the insufficient exposing surface area and low electron transportation due to the surface morphology. This is because nanogenerators, sensors, and piezoelectric tubes based on nanostructures strongly depend on the strength and stiffness of the materials [10]. Combining ZnO and SnO_2 on thin film can produce high sensitivity due to the heterogeneous interfaces between them.

Sensitivity, selectivity, response time, recovery time, and stability can be improved by combining different additives to SnO_2 [11]. Composite type sensors were suggested to improve thermal reliability because they contain many heterogeneous boundaries between different phases [12, 13]. For example ZnO/CuO, SnO_2/CuO, SnO_2/ZnO composites showed increased sensitivities in comparison to single-phase materials [14, 15]. Composites are beneficial because the combination of materials tend to be more porous. Especially, SnO_2 can be made more porous with addition of small amount of ZnO [16]. This porosity may play an imperative role in humidity sensing because the pores of the materials serve as adsorption sites. The sensitivity of the sensor directly depends on these pore sizes.

In this chapter, we introduce the technique of chemical vapor deposition method to prepare ZnO/SnO_2 composite nanorod on a glass substrates cover with ZnO thin film for humidity sensor applications. This technical paper investigates the effect of nanocomposited ZnO/SnO_2 on the surface morphology and humidity sensor application. The growth mechanism of ZnO/SnO_2 composite nanorod has been discussed.

2 Methodology

The glass substrates were cleaned with acetone, methanol, and deionized water in the ultrasonic device using several steps before the experiment began. At first, ZnO thin film was deposited on glass substrates using the radio frequency (RF) magnetron sputtering method. ZnO coated glass were deposited (high purity (99.999 %)) on glass substrate using RF magnetron system at RF power 200 W.

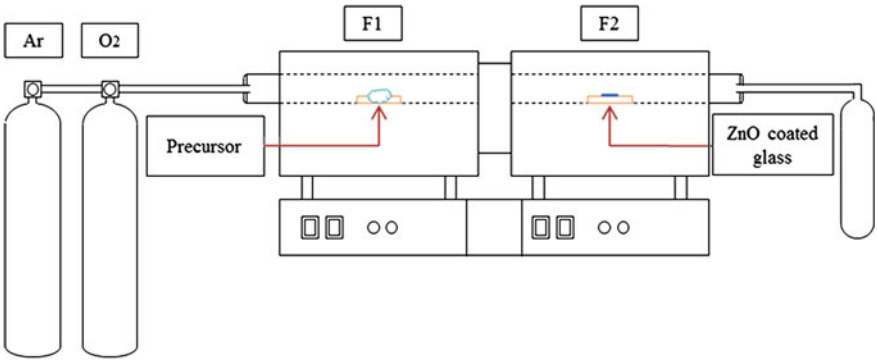

Fig. 1 CVD process

The pressure of the system was maintained at 7 m Torr and the sputter chamber was pumped at 5×10^{-4} Pa using a molecular pump. The gases were injected into the chamber with ratio of flow rate argon to oxygen (45:5) sccm. The ZnO thin films were deposited for 60 min with substrate temperature 500 °C.

In the second process, these ZnO films act as the template for ZnO/SnO_2 composite nanorod deposition. Two furnaces were used to grow doped ZnO/SnO_2 composite nanorods thin film as shown in Fig. 1. Furnace 1 was used to place precursor and Furnace 2 was used to place ZnO coated glass. Both precursor and glasses use a single Quarzt tube. Zinc nitrate and tin chloride act as the precursor, Argon (Ar) as the carrier gas, and oxygen (O_2) as the reactor gas. The flow rates of the gases were 20 sccm for Ar and 5 sccm for O_2. Both precursors were measured with 3 g. The substrate temperature was deposited at 500 °C and the deposition time was set at 1 h.

The humidity sensor measurement was conducted on Au metal contact deposited on the thin film as the electrode using thermal evaporation. The thin films were tested using two-point probe and the sensor was characterized using *I–V* measurement system (Keithley 2400) in a clean humidity chamber (ESPEC SH-261). The chamber had been set at the same room temperature (25 °C) with percent relative humidity (RH%) varied in the range of 40–90%RH. Structural properties were characterized using FESEM (JEOL JSM 6701F). Then the *I–V* was plotted using the Leios TMXpert software.

3 Result and Discussion

3.1 Structural Properties

Figure 2a shows the FESEM image of nanoparticle of ZnO template at 30,000 times magnification. The size of nanoparticle is in range of 75–85 nm. This ZnO template acts as a holder for ion zinc in thermal CVD method. The FESEM image at

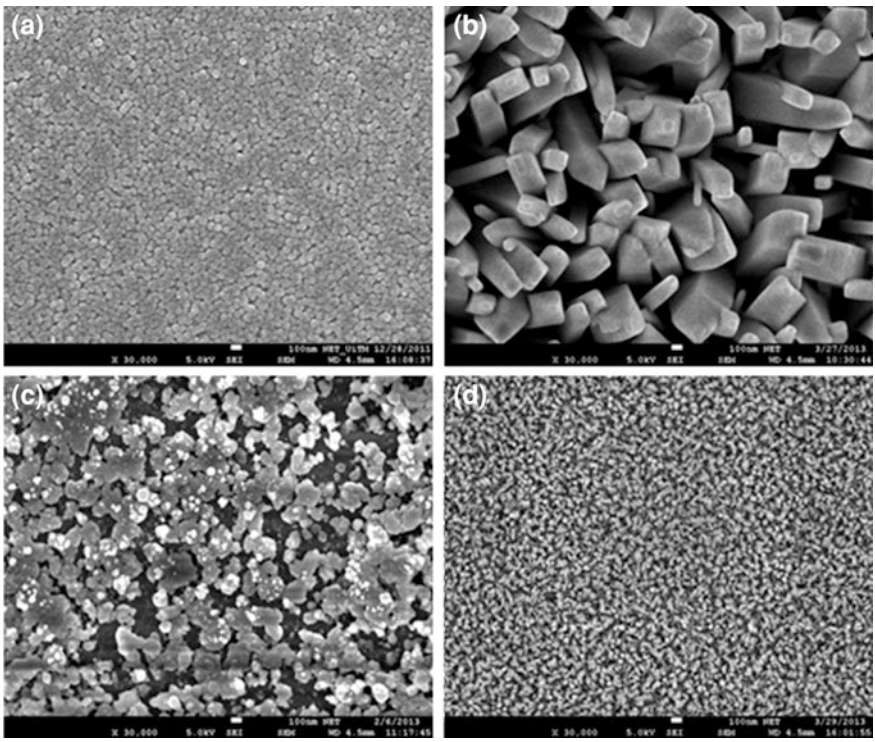

Fig. 2 FESEM images for **a** ZnO template **b** ZnO nanoparticle **c** SnO_2 nanorod and **d** ZnO/SnO_2 composite nanorods at magnification 30 kx

30 K magnification, as shown in Fig. 2b–d, shows the SnO_2 nanorods, ZnO agglomerate particle, and ZnO/SnO_2 composite nanorods. The surface images show that all films are uniformly deposited on ZnO template layer. The size of tip of SnO_2 nanorods was around 80–110 nm while the size of ZnO/SnO_2 composite nanorods was in the range of 35–50 nm. From the surface image, the size of nanorod of ZnO/SnO_2 composite nanorods reduces compared with SnO_2 nanorods as shown in Fig. 2c and d. This reduction of size enhances the high surface area that can increase the sensitivity because of larger site area to absorb the water vapor [17, 18, 19]. Besides, Fig. 3a and b shows the cross-sectional view of the SnO_2 nanorods and ZnO/SnO_2 composite nanorods respectively. The image shows the growth of well-aligned SnO_2 nanorods and ZnO/SnO_2 composite nanorods on ZnO template. It can be observed that the thickness of the SnO_2 nanorods is on average 5.4 μm. The thickness of ZnO/SnO_2 composite nanorods was on average 840 nm. The growth of SnO_2 nanorods on ZnO template for humidity sensor is come newly in this study. The growth of aligned SnO_2 nanorods is promoted by ZnO template as shown in Fig. 3a. Although it is hard to grow the SnO_2 nanorods on ZnO template since both materials are not in the same lattice group of structure, it is still possible for growth due to homogeneous nucleation [20, 21]. Salehi et al. [22] fabricated

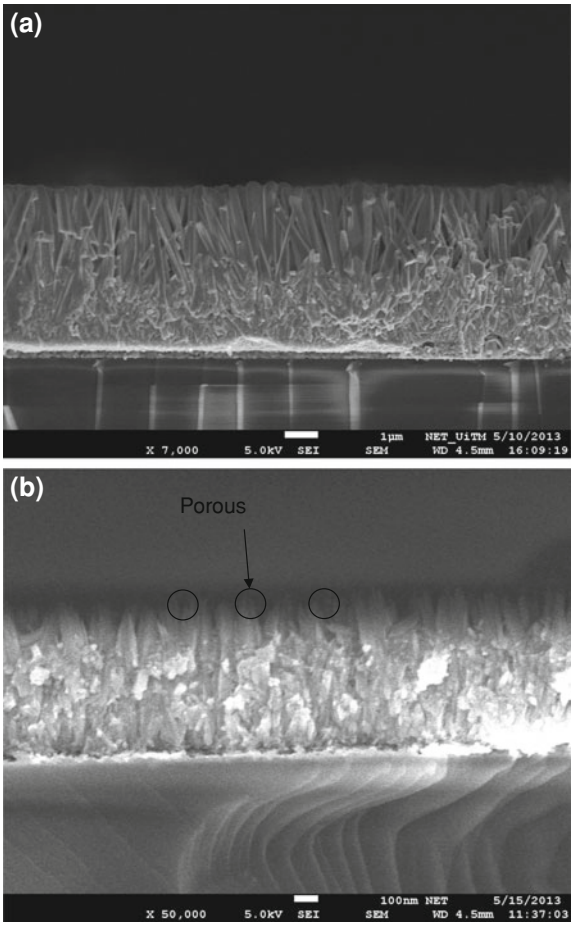

Fig. 3 The cross-sectional view of **a** SnO_2 nanorods and **b** ZnO/SnO_2 composite nanorods

SnO_2 pore structure-based gas sensor deposit on glass substrate using chemical vapor deposition method and SnCl4 as the precursor. Based on the ZnO/SnO_2 composite nanorods cross-sectional view, a porous structure is observed, as indicated in Fig. 3b, that promotes improvement in sensor performance [23–25]. Compared to other findings, Wang et al. [26] prepared Zn_2SnO_4 nanowire using thermal evaporation method by heating Sn and Zn powder as the precursor without any catalyst with diameter thickness of 50 nm. The use of two precursor of ZnO and SnO_2 deposit on ZnO template became a novelty in this study.

Table 1 shows the atomic percent for all the samples, refer to the EDS spectrum images in Fig. 4 (a) SnO_2 nanorods (b) ZnO agglomerate particle and (c) ZnO/SnO_2 composite nanorods. Table 1 and Fig. 4 show the possible corresponding chemical composition. It reveals that zinc (Zn), oxygen (O), and tin (Sn) are the

Table 1 Atomic percent of ZnO nanoparticle, SnO_2 nanorod, and ZnO/SnO_2 composite nanorods thin films

Atomic percent (%)	Zn	Sn	Si	O	C
SnO_2	0	28.47	5.28	66.26	0
ZnO	11.32	0	20.72	62.89	5.07
ZnO/SnO_2	0.87	71.59	3.75	23.79	0

constituent parts of ZnO/SnO_2 composite nanorods. The EDS measurements show that the dominant compositions for ZnO/SnO_2 composite nanorods thin film are Zn (0.87 %), Sn (71.59 %), and O (23.79 %).

The XRD patterns of SnO_2 nanorods, ZnO agglomerate particle, and ZnO/SnO_2 composite nanorods show polycrystalline as depicted in Fig. 5. The diffraction of SnO_2 nanorods contained diffraction peaks from tetragonal SnO_2 (JCPDS card no. 41-1445). While the ZnO agglomerate particle match with hexagonal wurzite ZnO (JCPDS card no. 36-1451). ZnO/SnO_2 composite nanorods diffraction peaks can be indexed with the tetragonal SnO_2 and hexagonal wurzite ZnO. It is observed that the peaks of SnO_2 nanorods reveal at diffraction peaks (101) (211) (002) (301). The higher intensity is at (101) and (002) of SnO_2 compared to other peaks. This indicates that SnO_2 nanorods enhance to the (002) peak that are preferably orientated in [001] direction [27, 28]. The diffraction peak of ZnO agglomerate particle depict at (100) (002) (101) (102) (110), and (103). However, ZnO/SnO_2 composite nanorods perform peak of ZnO at (100) orientation whereby the dominant peaks belong to tetragonal SnO_2 show at peaks (110) (101) (211) (002), and (301). The (100) peaks of ZnO indicate that the ZnO precursor acts as the holder to the ZnO/SnO_2 composite nanorods.

The possible growth of ZnO/SnO_2 composite nanorods is discussed as indicated in Fig. 6. In this study, no metal catalyst has been used. The growth of ZnO/SnO_2 composite nanorods was influenced with ZnO thin film that acts as the template layer. The growth mechanism can be understood based on vapor solid growth (VS) process. The chemical reaction can be explained as:

$$SnCl_2 + O_2 \rightarrow SnO_2 + Cl_2 \quad (1)$$

$$2Zn(NO_3)_2 \rightarrow 2ZnO + 4NO_2 + O_2 \quad (2)$$

$SnCl_4$ and $Zn(NO_3)_2$ were reduced to Sn and Zn vapor by reaction at 500 °C. The source $SnCl_4$ and Zn were carried by the flowing Ar gas and react with O_2 gas (Eqs. (1) and (2)). The Zn was directly deposited on the ZnO template. Then the ZnO templates act as the nucleation sites for the growth of ZnO nanostructures. Once the initial nucleation starts, the crystal grows in epitaxial ways, which results in the preferential orientation of ZnO/SnO_2 composite nanorods in the end.

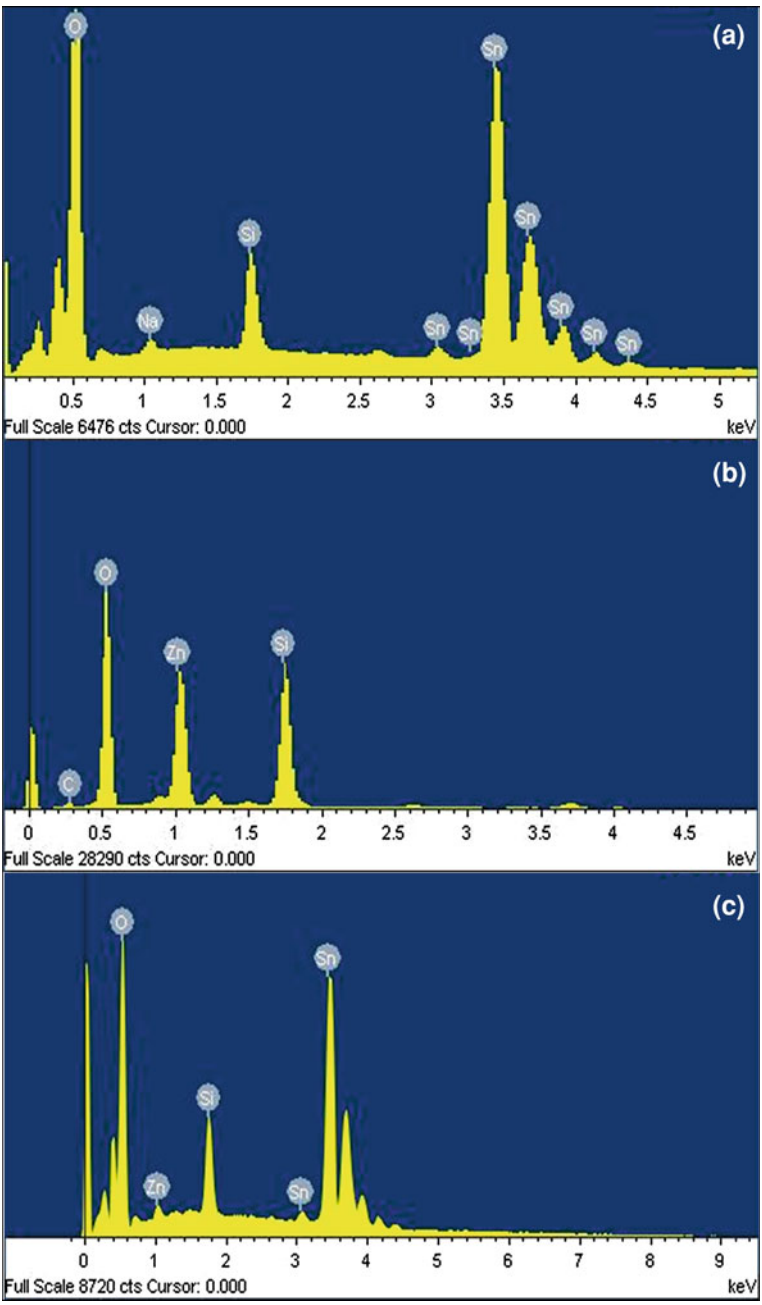

Fig. 4 EDS spectrum images for **a** ZnO nanoparticle, **b** SnO_2 nanorod, and **c** ZnO/SnO_2 composite nanorod thin films

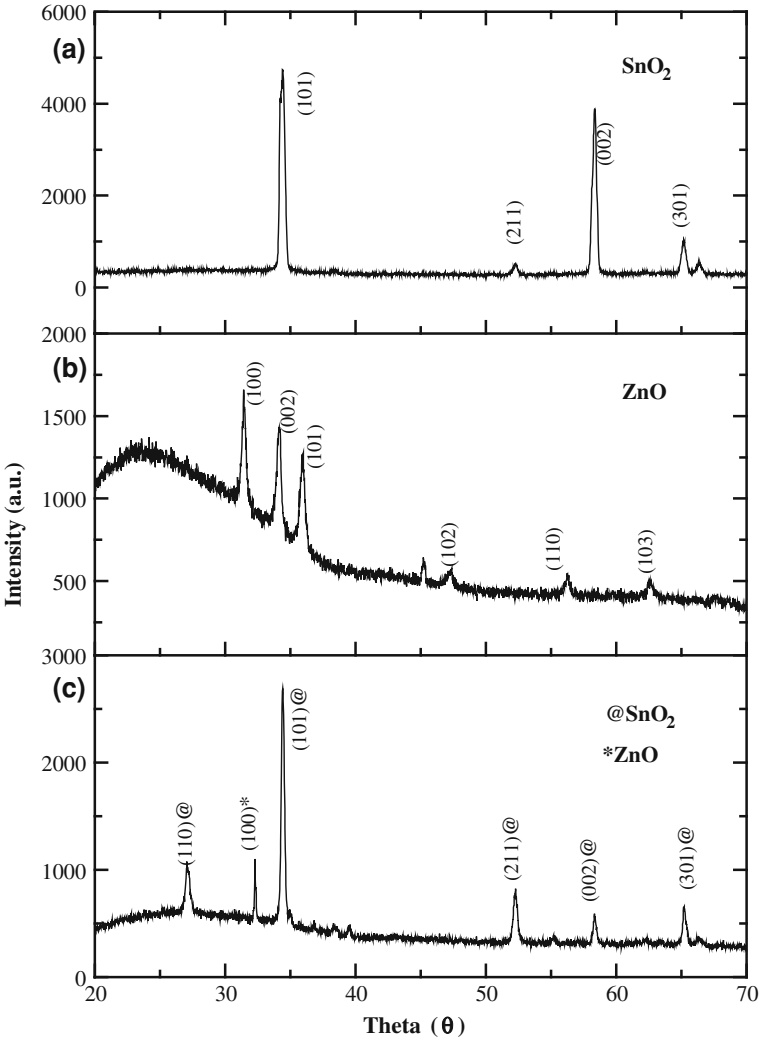

Fig. 5 The XRD pattern of **a** SnO2 nanorods, **b** ZnO nanoparticle, and **c** ZnO/SnO_2 composite nanorods

3.2 Optical Properties

Figure 7 shows PL spectra of (a) SnO_2 nanorods (b) ZnO agglomerate nanoparticle, and (c) ZnO/SnO_2 composite nanorods excited by He-cd laser operating at 325 nm. The SnO_2 nanorods show a broad peak at around 630 nm as the ZnO agglomerate nanoparticle and ZnO/SnO_2 composite nanorods depict two emission bands at ultraviolet (UV) emission and broad visible region. The UV emission and

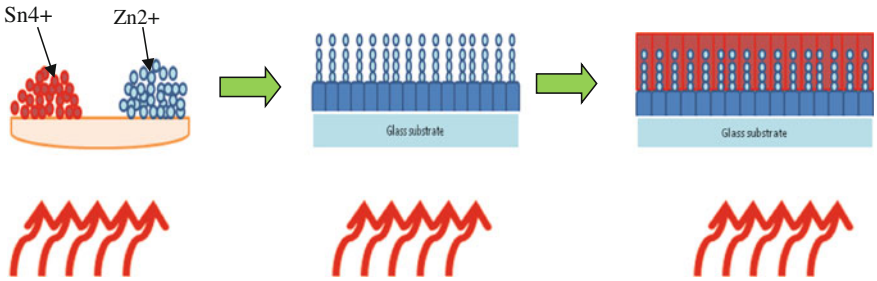

Fig. 6 The possible growth mechanism of ZnO/SnO_2 composite nanorods on ZnO template

visible region of ZnO agglomerate nanoparticle is indicated at around 400 nm and 650 nm, respectively, while the ZnO/SnO_2 composite nanorod signifies at around 380 nm and 585 nm respectively. Both samples show a weak peak at UV region and a dominant peak at visible area. The UV emission corresponds to the recombination of free excitons of ZnO [29]. The visible peak corresponds to existence of the Zn and Sn interstitial defect, oxygen vacancies in ZnO and SnO_2, and residual strain tempt during the growth process. These prominence peaks may contribute to better interaction between the adsorbed water vapor and the active layer [30]. From the graph, the peaks of ZnO/SnO_2 composite nanorods move to the left (blue shift) from the peaks of ZnO agglomerate nanoparticle and SnO_2 nanorods. The blue shift can be explained due to the transition of electron transition, mediated by oxygen vacancies [31]. The high intensity level of ZnO/SnO_2 composite nanorods was high compared with ZnO agglomerate nanoparticle and SnO_2 nanorods. It may contribute by the rougher surface of ZnO/SnO_2 composite nanorods.

3.3 Humidity Sensor Fabrication

Figure 8a–c shows *I–V* plots for thin films for ZnO nanoparticle, SnO_2 nanorod, and ZnO/SnO_2 composite nanorods with relative humidity of 40–90 % at 25 °C. The samples were given supplied voltage from −5 to 5 V. The current increases when relative humidity increases so the resistance is decreased. This is because the water vapor on the surface of thin films was absorption. This water vapor can increase the flow of the current through the thin film with less resistance. The water vapor in air has a strong influence on the conductivity of the thin films [32]. In any RH atmosphere, *I–V* curves of the device exhibit good linear behavior, which proves a good ohmic contact between the surfaces and Au electrodes.

The composite ZnO/SnO_2 composite nanorods sensor exhibited significantly higher sensitivity than sensor constructed solely from ZnO nanoparticle or SnO_2 nanorod itself due to the heterogeneous interfaces between them and more adsorption site was created that can help more water vapor to be absorbed [16].

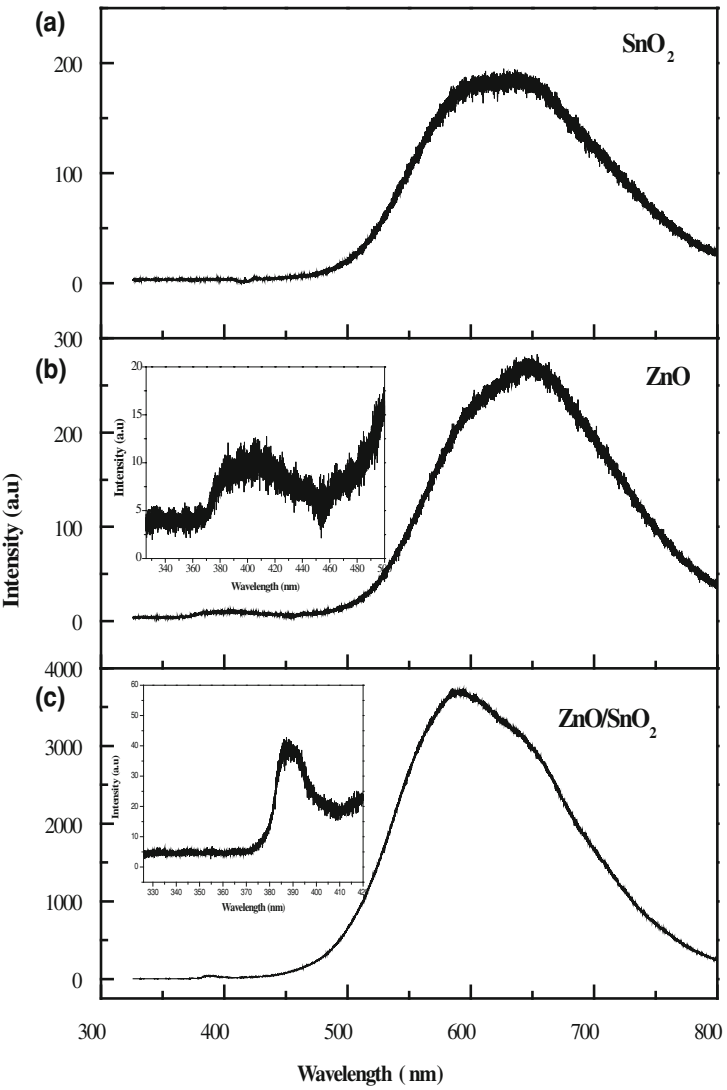

Fig. 7 Photoluminescence spectra **a** SnO_2 nanorods, **b** ZnO agglomerate nanoparticle, and **c** ZnO/SnO_2 composite nanorods

The graph in Fig. 8 shows that sensitivity increases when RH increases. This phenomenon is related to water adsorption on the thin films. At low RH, water adsorbing on the surfaces will not donate electrons to sensing layers and will significantly lower the sensitivity of thin films. The larger the surface area, the larger the content of water adsorbed, so the density of charge carrier becomes larger and hence the sensitivity increases [33]. The sensing mechanism is based on the absorption and desorption process between the surface structure and humidity [34].

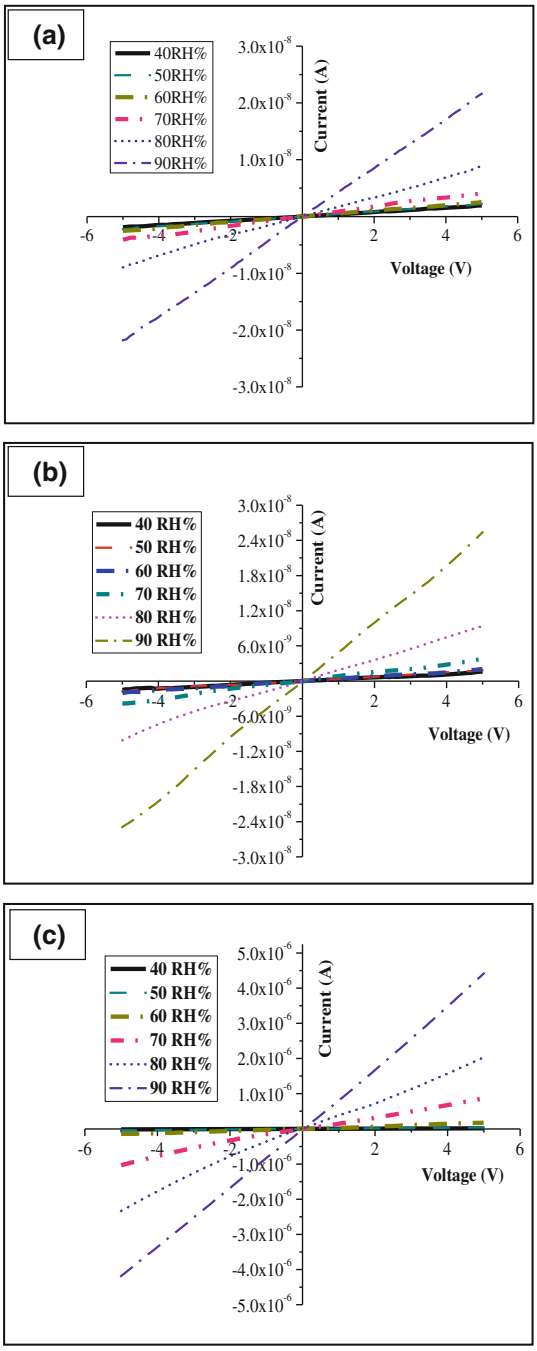

Fig. 8 **a** *I–V* measurement at different RH% of Md Sin SnO_2 nanorods, **b** ZnO nanoparticle, and **c** ZnO/SnO_2 composite nanorods

Table 2 The value of sensitivity and response and recovery times of SnO_2 nanorods, ZnO agglomerate nanoparticle and ZnO/SnO_2 composite nanorods are summarized

Sample (ZnO/SnO_2)	Sensitivity	Response (s)	Recovery (s)
SnO_2	16	371	114
ZnO	11	392	259
ZnO/SnO_2	265	227	34

For sensitivity, the value was calculated using Eq. (3) [35]:

$$S = \frac{I_{90\,\mathrm{RH\%}}}{I_{40\,\mathrm{RH\%}}} \tag{3}$$

where S as sensitivity, $I_{40\mathrm{RH\%}}$ as current of the sensor in dry condition, and $I_{90\mathrm{RH\%}}$ as current at 90RH% (relative humidity). The sensitivity values are listed in Table 2. The sensor current of SnO_2 nanorods and ZnO agglomerate nanoparticle at 40%RH were 1.94×10^{-9} A and 1.61×10^{-9} A respectively. Whereas at 90%RH, the current of SnO_2 nanorods and ZnO agglomerate nanoparticle was 2.16×10^{-8} A and 2.54×10^{-8} A respectively. The changes in current are based on the equation performed 11 and 16 times for SnO_2 nanorods and ZnO agglomerate nanoparticle respectively. The changes in current at about two orders at 40%RH is 1.67×10^{-8} A is 265 times than 90%RH is 4.42×10^{-6} A of ZnO/SnO_2 composite nanorods. From Table 1, the ZnO/SnO_2 composite nanorods sensor exhibited significantly higher sensitivity than sensor constructed solely from ZnO agglomerate nanoparticle and SnO_2 nanorod itself due to the heterogeneous interfaces between them and more adsorption site was created that could help more water vapor to be absorbed [16]. Besides, the high surface area facilitates the reaction with water vapor and sensing layer of ZnO/SnO_2 composite nanorods sensor [36, 37]. Moreover, the advantage of one-dimensional structure (1D) of ZnO/SnO_2 composite nanorods sensor could assist the electron to transverse along the rods' structure [37].

Figure 9 shows the response and recovery time of (a) SnO_2 nanorods, (b) ZnO agglomerate nanoparticle, and (c) ZnO/SnO_2 composite nanorods with the time taken for the transition total current to become constant from 40 to 90%RH (adsorption process) is assigned as response time and 90 to 40%RH (desorption process) for the recovery time. The sensor was given bias 5 V. Table 1 shows the calculated response and recovery time using Eq. (4) [38]:

$$I(t) = I_0\left(1 - e\left(-\frac{t}{t_r}\right)\right) \quad \text{for the response time (absorption process)} \tag{4}$$

$$I(t) = I_0 e\left(-\frac{t}{t_d}\right) \quad \text{for the recovery time (desorption process)}$$

where I is the magnitude of current, I_0 is saturated current, t is time, t_r is response time constant, and t_d is the recovery time constant. When the thin films were

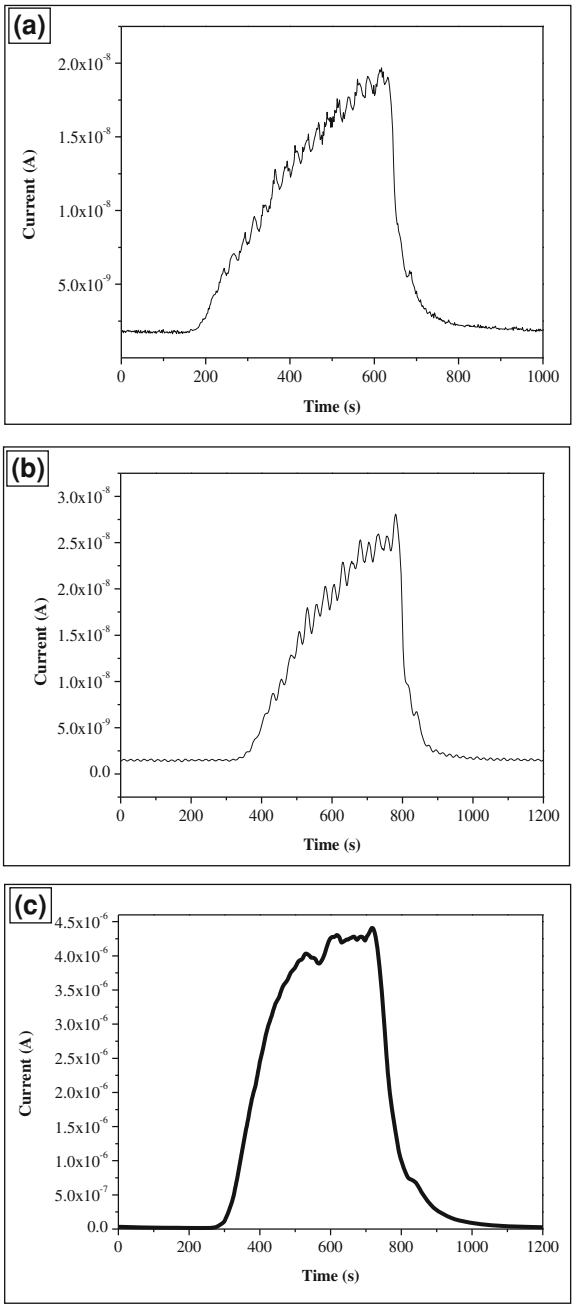

Fig. 9 The response and recovery characteristics curve of **a** SnO_2 nanorods, **b** ZnO nanoparticle, and **c** ZnO/SnO_2 composite nanorods obtained by changing the RH% between 40 and 90

exposed to the 90%RH, the current through the sensors increased. When the thin films switched to dry condition again (40%RH), the current decreased and reached a relatively stable value. According to Table 2, the response times of the SnO_2 nanorods and ZnO agglomerate nanoparticles were 371 s and 392 s, respectively, while the recovery time of the SnO_2 nanorods and ZnO agglomerate nanoparticles were 114 s and 259 s respectively. ZnO/SnO_2 composite nanorod has the fastest time to response and recovery time with 227 s and 34 s respectively.

The sensing mechanism is based on the absorption and desorption process between the surface structure and humidity [34]. At low humidity, the tips and defects of the thin films present a high local charge density and a strong electrostatic field, which promotes water dissociation. The dissociation provides protons as charge carriers of the hopping transport [39]. At high humidity, one or several serial water layers are formed among thin films, and electrolytic conduction between sensing materials takes place along with photonic transport and becomes dominating in the transport process [39].

4 Conclusion

In this chapter, ZnO/SnO_2 composite nanorods were successfully synthesized using thermal CVD. The SnO_2 nanorods, ZnO agglomerate nanoparticle, and ZnO/SnO_2 nanoflower were successfully grown on ZnO template layer. The SnO_2 nanorod and ZnO agglomerate nanoparticles produce sensitivity with 16 and 11 ratios of times. The ZnO/SnO_2 composite nanorods give the highest sensitivity with ratio of 265 times. The response and recovery time for these ZnO/SnO_2 composite nanorods are the fastest among ZnO nanoparticles and SnO_2 nanorods with 227 s and 34 s respectively.

References

1. Pelino, M., Cantalini, C., Faccio, M.: Principles and applications of ceramic humidity sensors. Act. Passiv. Elect. Compon. **16** (1994)
2. Shimizu, Y., Yamazoe, N.: Humidity Sensors: Principles and Applications. Sens. Actuators **10**, 379–398 (1986)
3. Regtien, P.P.L.: Humidity sensors. Meas. Sci. Technol. **23**(1) (2012)
4. Z. Chen CL (2005). Humidity sensors: a review of materials and mechanisms, Sens
5. Z.L. Wang ZCK (1998) Functional and Smart Materials Structural Evolution and Structure Analysis
6. Wang, C., Wang, X., Zhao, J., Mai, B., Sheng, G., Peng, P., Fu, J.: Synthesis, characterization and phtocatalytic property of nano-sized Zn_2SnO_4. J. Mater. Sci. **37**, 2898–2996, (2002)
7. Young, D.L., Williamson, D.L., Coutts, T.J.: Structural characterization of zinc stannate thin films. J. Appl. Phys. **91**, 1464 (2002)

8. Stambolova, I., Konstantinov, K., Kovacheva, D., Peshev, P., Donchev, T.: Spray pyrolysis preparation and humidity sensing characteristics of spinel zinc Stan-nate thin films. J. Solid State Chem. **128**, 5 (1997)
9. Zhu, C.L., Chen, Y.J., Wang, R.X., Wang, L.J., Cao, M.S., Shi, X.L.: Synthesis and enhanced ethanol sensing properties of α-Fe_2O_3/ZnO heteronanostructures. Sens. Actuat. **140**, 185–189 (2009)
10. Yu GJXZD: Effect of surface morphology on the mechanical properties of ZnO nanowires (2010)
11. Chengxiang Wang, L.Y., Luyuan, Z., Dong, X., Rui, G.: Sensors. Metal Oxide Gas Sensors: Sensitivity and Influencing Factors (2010)
12. De Lacy Costello, B.P.J., Ewen, R.J., Jones, P.R.H., Ratcliffe, N.M., Wat, R.K.M.: A study of the catalytic and vapour-sensing properties of zinc oxide and tin dioxide in relation to 1-butanol and dimethyldisulphide. Sens. Actuat. B **61**, 199–207 (1999)
13. Yu, J.H., Choi, G.M.: Electrical and CO gas sensing properties of ZnO–SnO_2 composites. Sens. Actuat. B. **52**, 251–256 (1998)
14. Moon, W.J., Yu, J.H., Choi, G.M.: Selective CO gas detection of SnO_2–Zn_2SnO_4 composite gas sensor. Sens. Actuators B **80**, 21–27 (2001)
15. Zhang YSSaTS: Preparation, structure and gas-sensing properties of ultramicro $ZnSnO_3$ powder. Sensors and Actuators B **12**, 5–9 (1993)
16. Wagh LAP, M.S., Seth, T., Amalnerkar, D.P.: Surface cupricated SnO_2–ZnO thick film as a H_2S gas sensor. Mater. Chem. Phys. **84**, 228–233 (2004)
17. Jamil, H., Batool, S.S., Imran, Z., Usman, M., Rafiq, M.A., Willander, M., Hassan, M.M.: Electrospun titanium dioxide nanofiber humidity sensors with high sensitivity. Ceram. Int. **38**(3), 2437–2441 (2012)
18. Kuang, Q., Lao, C., Wang, Z.L., Xie, Z., Zheng, L.: High-sensitivity humidity sensor Based ON a single SnO_2 nanowire. J. Am. Chem. Soc. **129**(19), 6070–6071 (2007). doi:10.1021/ja070788m
19. Song, X., Qi, Q., Zhang, T., Wang, C.: A humidity sensor based on KCl-doped SnO_2 nanofibers. Sens. Actuators B: Chem **138**(1), 368–373 (2009)
20. Feder, J., Russell, K., Lothe, J., Pound, G.: Homogeneous nucleation and growth of droplets in vapours. Adv. Phys. **15**(57), 111–178 (1966)
21. Oxtoby, D.W.: Homogeneous nucleation: theory and experiment. J. Phys.: Condens. Matter **4**(38), 7627 (1992)
22. Salehi, A.: A highly sensitive self heated SnO_2 carbon monoxide sensor. Sens. Actuators B: Chem. **96**(1–2), 88–93
23. Kim, H., Sathaye, S.D., Hwang, Y.K., Jhung, S.H., Hwang, J., Kwon, S.H., Park, S., Chang, J.: Humidity sensing properties of nanoporous TiO_2–SnO_2 ceramic sensors. Bull. Korean Chem. Soc. **26**(11), 1881 (2005)
24. Wang, W., Tian, Y., Li, X., Wang, X., He, H., Xu, Y., He, C.: Enhanced ethanol sensing properties of Zn-doped SnO_2 porous hollow microspheres. Appl. Surf. Sci. (2012)
25. Yuan, Q., Li, N., Tu, J., Li, X., Wang, R., Zhang, T., Shao, C.: Preparation and humidity sensitive property of mesoporous ZnO–SiO_2 composite. Sens. Actuators B: Chem. **149**(2), 413–419 (2010)
26. Wang, L., Zhang, X., Liao, X., Yang, W.: A simple method to synthesize single-crystalline Zn_2 SnO_4 (ZTO) nanowires and their photoluminescence properties. Nanotechnology **16**(12), 2928 (2005)
27. Jiang, Q., Li, Y., Du, G., Liu, Y., Zhao, H.: A novel structure of SnO_2 nanorod arrays synthesized via a hydrothermal method. Mater. Lett. **94**, 100–103 (2013)
28. Wang, Y.-L., Guo, M., Zhang, M., Wang, X.-D.: Hydrothermal preparation and photoelectrochemical performance of size-controlled SnO_2 nanorod arrays. CrystEngComm **12**(12), 4024–4027 (2010). doi:10.1039/c0ce00201a
29. Asokan, K., Park, J., Choi, S.-W., Kim, S.: Nanocomposite ZnO–SnO_2 nanofibers synthesized by electrospinning method. Nanoscale Res. Lett. **5**(4), 747–752 (2010). doi:10.1007/s11671-010-9552-y

30. Kannan, P.K., Saraswathi, R., Rayappan, J.B.B.: A highly sensitive humidity sensor based on DC reactive magnetron sputtered zinc oxide thin film. Sens. Actuators A **164**(1–2), 8–14 (2010)
31. Wang, Z., Huang, B., Liu, X., Qin, X., Zhang, X., Wei, J., Wang, P., Yao, S., Zhang, Q., Jing, X.: Photoluminescence studies from ZnO nanorod arrays synthesized by hydrothermal method with polyvinyl alcohol as surfactant. Mater. Lett. **62**(17), 2637–2639 (2008)
32. Parthibavarman, M., Hariharan, V., Sekar, C.: High-sensitivity humidity sensor based on SnO_2 nanoparticles synthesized by microwave irradiation method. Mater. Sci. Eng. **31**, 840–844 (2011)
33. Qin, K., Lao, C., Zhong Lin, W., Xie, Z., Lansun, Z.: High-sensitivity humidity sensor based on a single SnO_2 nanowire (2007)
34. Md Sin, N.D., Mamat, M.H., Musa, M.Z., Abdul Aziz, A., Rusop, M.: Effect of growth duration to the electrical properties of Zn doped SnO_2 thin film toward humidity sensor application (2012)
35. Qi Qia, T.Z., Yi, Z., Haibin, Y.: Sensors and actuators humidity sensing properties of KCl-doped Cu. Sens. Actuators, B **137**, 21–26 (2009)
36. Gu, L., Zheng, K., Zhou, Y., Li, J., Mo, X., Patzke, G.R., Chen, G.: Humidity sensors based on ZnO/TiO_2 core/shell nanorod arrays with enhanced sensitivity. Sens. Actuators B: Chem. **159**(1), 1–7 (2011)
37. Song, Xiaofeng, Liu, Li: Characterization of electrospun ZnO–SnO_2 nanofibers for ethanol sensor. Sens. Actuators, A **154**(1), 175–179 (2009)
38. Mamat, M.H., Khusaimi, Z., Musa, M.Z., Malek, M.F., Rusop, M.: Fabrication of ultraviolet photoconductive sensor using a novel aluminium-doped zinc oxide nanorod–nanoflake network thin film prepared via ultrasonic-assisted sol–gel and immersion methods. Sens. Actuators, A **171**(2), 241–247 (2011)
39. Xu, L., Wang, R., Xiao, Q., Zhang, D., Liu, Y.: Micro humidity sensor with high sensitivity and quick response/recovery based on ZnO/TiO_2 composite nanofibers. Chin. Phys. Lett. **28**, 070702 (2011)

Chemical Solution-Based Synthesis of Nano-Magnesium Oxide Dielectrics

Habibah Zulkefle, Adillah Nurasyikin, Lyly Nyl, Raudah Abu Bakar and Mohamad Rusop Mahmood

Abstract The effect of MgO nano-filler loading to the dielectric layer properties of nano-Mgo films has been studied. By using FESEM, the particle size of nano-MgO dielectrics was found in nanometer dimension with the range of 42 to 92 nm. The addition of MgO nano-filler resulted in surface modification in which it lead to the changes in dielectrics properties. From impedance analysis it shows that there were only small changes in relative permittivity value since the filler and the matrix were the same material. The result also revealed that the dielectrics with 1 wt% filler loading has good electrical properties while dielectrics 2 wt% filler loading was very uniform and compact.

1 Dielectrics Mechanism

Dielectric is an important medium in parallel plate capacitor where the charge storage ability per unit voltage (capacitance) increases by a factor of relative permittivity, ε_r. The relationship between capacitance and relative permittivity is given by the following equation [1]:

$$C = \frac{\varepsilon_o \varepsilon_r A}{d} \tag{1}$$

where ε_o (8.8542×10^{-12} F/m) is vacuum permittivity, ε_r is the relative permittivity of dielectric material, A is the electrode area, and d is the thickness of the dielectric layer. Theoretically, the relative permittivity of the dielectric material

H. Zulkefle (✉) · A. Nurasyikin · L. Nyl · R. A. Bakar · M. R. Mahmood
NANO-ElecTronic Centre (NET), Faculty of Electrical Engineering,
Universiti Teknologi MARA, 40450 Shah Alam, Malaysia
e-mail: habibahzulkefle@yahoo.com

F. L. Gaol and J. Webb (eds.), *Recent Trends in Nanotechnology and Materials Science*, Engineering Materials, DOI: 10.1007/978-3-319-04516-0_3,

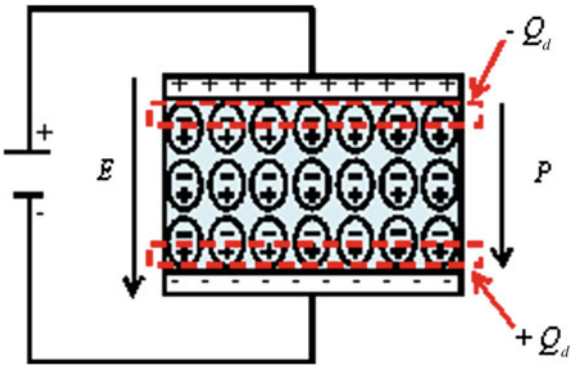

Fig. 1 Schematic diagram of polarization in dielectrics medium

depends strongly on the frequency of the alternate electric field which can be expressed by the following complex permittivity equation:

$$\varepsilon = \varepsilon' - j\varepsilon'' = \varepsilon_o \varepsilon_r - j\varepsilon'' \tag{2}$$

where ε' and ε'' refers to real and imaginary permittivity. The energy storing capacity of the dielectric material depends on the polarization, *P,* of the dielectrics by applied field, *E*. When dielectric material is placed in between two parallel plated with applied field, the dielectrics atom or molecule become polarized which results in dipole moment. Induced dipole moment is in the same direction with applied field and the dipole is aligned negative charge, $-Q_d$ to positive charge $+Q_d$. Besides, for each positive charge has a negative charge next to it and vice versa which results in not net charge in the dielectric material. However, the negative charge is not canceled by any positive charge of dipole at the interface of dielectric layer and the similar situation happen at the other side of dielectric layer. These bound charges at the interface that resulted from the polarization were known as surface polarization charges. Figure 1 reveals the polarization process occurred in the dielectrics by applied field.

As being explained in previous paragraph, space charge polarization involves trapped charges at the interface of the dielectric layer. In addition, this type of polarization mainly occurs in amorphous or polycrystalline solids or material consisting of traps. In thin film dielectric technology, polarization occurs is in terms of space charge polarization. Space charge polarization involved hopping and interfacial polarization, which is commonly present at 10^{-2}–10^{6} Hz.

A good dielectrics film should have high relative permittivity, thermal and chemical stability contact with semiconductor, low leakage current, and high quality interface [2]. For thin film dielectrics, relative permittivity also depends on chemical structure and defect of the film. Generally, silicon dioxide, SiO_2, with dielectric constant of 3.9 has been used as dielectric layer in the electronic component fabrication such as in transistor and capacitor. Normally, the size of electronic devices becomes smaller while its performance is improved. The current technology has archived 6 nm ultrathin of SiO_2 dielectric layer. However, the

thickness cannot be reduced anymore due to the leakage current. Hence, higher relative permittivity materials need to be used to replace SiO_2 and enhance the overall device performances [3, 4].

The oxide materials with wide bandgap ($E_g > 5$ eV) are mostly considered to be used as dielectric material in the past few decades [5]. There are several materials that have wide energy bandgap such as alkali halides and the best candidate to be used as the dielectric material is magnesium oxide, MgO. MgO cubic in structure form by ionic bonding between Mg^{2+} and O^{2-} ions and it is a source of magnesium. The physical properties of MgO such as hardness, high resistivity, and high melting point are due to the strong electrostatic force between magnesium and oxygen ion. Other than that, chemical inertness, electrical insulation, optical transparency, high temperature stability, and high thermal conductivity are the properties of magnesium oxide. Besides, the unique properties of MgO such as high relative permittivity and high breakdown field have made this oxide material possible to replace commercially available SiO_2 as dielectrics.

Particle size with nanometer dimension has attracted much attention in thin film fabrication due to its excellent properties, which will enhance film properties such as in electrical insulation, breakdown strength, and dielectrics properties [6, 7]. One of the promising methods in development of nanoparticle is by introducing nano-filler [8] during deposition process. There are several researches been done on using magnesium oxide, MgO as filler in order to improve the electrical [7, 9] and dielectric properties [10]. Although the inclusion of nano-filler could lead to outstanding thin film properties, the source of the improvement and the effects of nano-MgO filler on the MgO film properties are still being investigated [11]. The deposition of nano-MgO can be utilized by several techniques such as spin coating [12–15], sol–gel spin coating has its own advantages such as simple and cost effective. In this research work, we investigate the effect of nano-MgO filler loading on the dielectric properties of MgO film via simple chemical solution technique which is sol–gel spin coating method.

2 Experimental Procedure

All chemicals used were analytical reagent grade and utilized without any purification. The chemicals used were Magnesium Acetate Tetrahydrate (Merck), Magnesium Oxide Nano-Powder (<50 nm, Aldrich Chemistry), Ethanol (95 %, HmbG Chemicals), and Nitric Acid (69 %, Friendemann Schmidt).

Magnesium oxide, MgO solution was prepared by dissolving (CH_3COO_2) Mg*$4H_2$ in C_2H_6O solution with a small addition of HNO_3. The MgO nano-powder used as filler was added into the MgO solution with the amount of MgO nano-powder that varied from 0 to 3 wt%. The prepared solutions were then sonicated at 50 °C for 20 min followed by heating, stirring, and aging process. For the deposition process, the prepared MgO solutions were deposited on a cleaned glass substrate with speed rotation and time were set to 3200 rpm and 30 s,

respectively. Then, the films were dried at 200 °C for 10 min and both deposition and drying processes were repeated for 10 times. Finally, the films were annealed in the furnace chamber with temperature of 500 °C for 1 h. The characteristic of the deposited MgO films at different weight percentage of MgO nano-filler were determined in terms of it electrical, dielectric, and morphological properties. The two points probe *I–V* measurement (Bukoh Keiki) and impedance spectroscopy analyzer (Solartron S1 1260A-1296) were used to investigate the electrical and dielectric properties of the MgO films. Atomic force microscopy (AFM-Park System XE 100) and field emission scanning electron microscopy (FESEM-JEOL JSM 7600F) were used to observe the morphological of MgO films.

3 Nano-Magnesium Oxide Dielectrics Properties

The growth of nano-MgO films was measured in terms of its thickness using surface profiler and the data were tabulated in Table 1. The changes of the thickness show a significant effect of the nano-filler loading. Increase of film thickness with nano-filler loading was due to increase of growth rate of thin film [16]. As stated by Hu et al. surface roughness of the produced films was determined from the surface texture by means, the root mean square (RMS) value of the surface height [17]. Highest RMS value was obtained for film with 1 wt%, however, 2 wt% nano-MgO film resulted in the lowest RMS value (Table 1). As mentioned by Thomas et al., the surface roughness of film tends to increase as the amount of filler increase, which was due to the formation of agglomerated particle [10]. This finding was proved by surface morphology images as shown in Fig. 2, where sample with 1 and 3 wt% have nonuniform and agglomerated particle, which lead high surface roughness.

Figure 2 shows the surface morphology of deposited nano-MgO films at different nano-filler loading. From the FESEM images obtained the surface modifications of the deposited nano-MgO films that occurred in terms of changes in the grain boundary, particle size, as well as porosity. It was observed that, as the amount of nano-filler increased from 0 to 3 wt%, more compact film were produced. This was due to increment in particle size and reduction of grain boundaries. Agglomerated particle was formed for nano-MgO film with 3 wt% filler loading.

Excessive MgO particle at higher nano-filler loading resulted in the formation of agglomerated particle on the film. Figure 3a and b shows the illustration for diffusion of nano-filler with small and high amount, respectively. Average of particle produced for nano-MgO films with 0, 1, 2, and 3 wt% were 42.2, 47.1, 59.4, and 91.8 nm, respectively. Moreover, FESEM images also revealed that film with 2 wt% nano-filler loading produced very uniform and dense in structure, compared to others. We expect film with 2 wt% nano-filler loading was enough to fill up all the pores, and act as catalyst to improve the surface morphology of the film.

Table 1 Thickness and surface roughness of the nano-MgO films at different nano-filler content

Nano-filler content (wt%)	Capacitance at 40 kHz (pF)	Thickness (nm)	Surface roughness (nm)	
			Average value, Ra	Root mean square value, Rq
0	6.72	256	14.572	23.474
1	7.33	344	25.266	32.737
2	6.95	633	3.022	4.395
3	7.18	964	23.826	30.316

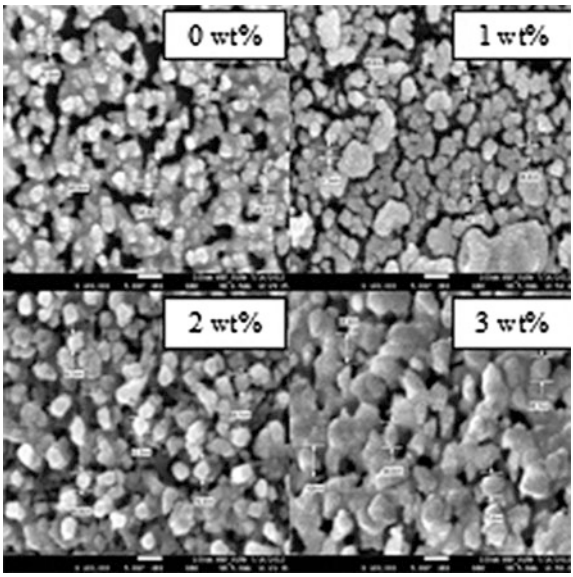

Fig. 2 Dependence of the MgO nano-filler content on the films surface morphology

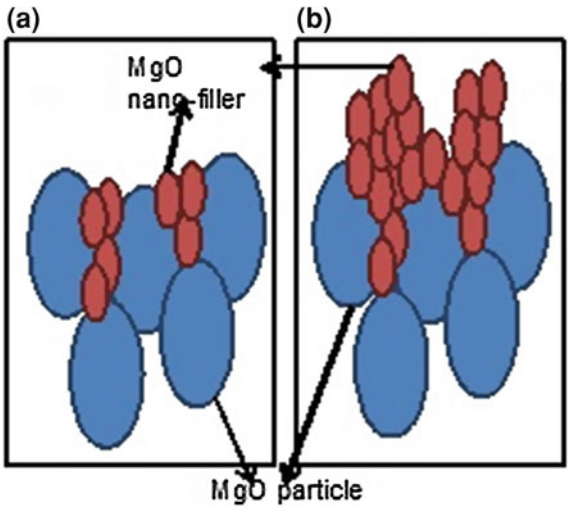

Fig. 3 Illustration on filler dispersion at **a** low and **b** high nano-filler content

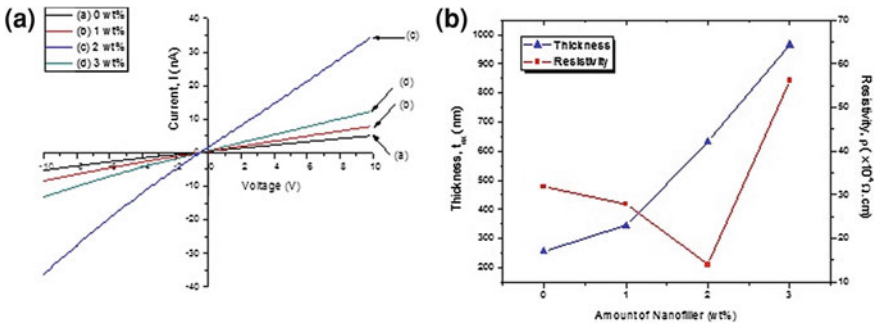

Fig. 4 Electrical behavior in terms of **a** *I–V* Characteristic and **b** Resistivity of deposited nano-MgO films

Figure 4a shows the current-voltage (*I–V*) behavior of deposited Nano-MgO films at different loading of MgO nano-filler with applied voltage from −10 to 10 V. *I–V* curve for sample with 2 wt% nano-filler loading does not cross the zero axis. However, the reason behind this occurrence is still being investigated. From the graph it shows that the resistance of the films change as the amount of nano-fillerwas varied. The value of resistivity (Fig. 4b) for each film was then calculated by using $\rho = \frac{wt}{l}R$ equation, where ρ is the resistivity; w and t are the width and the length of the metal contact; t is the film thickness, and R is the film resistance [18].

The result shows that by introducing nano-filler, results in decrement of the resistivity value from 31.9×10^4 to 27.9×10^4 Ω cm. Further, increase in the amount of nano-filler (2 wt%), the resistivity value was found to continuously decrease to 14.0×10^4 Ω cm. The reduction in resistivity values were due to the nano-size particle added that further reduced the grain boundary area of the films (Fig. 2). As nano-filler being introduced, the surface area to volume ratio of the film produced was increased and [19] later improved carrier's transport properties. As a result, the carrier scattering was reduced while carrier mobility was enhanced. This observation was supported by Mary et al. where their conductivity value increased with the addition of nano-filler [20]. The resistivity values at room temperature obtained has similar order ($\sim 10^4$ Ω cm) with reported value by Patil et al. for microwave component [21].

However, when the nano-filler content was increased to 3 wt%, the resistivity value was drastically increased to 56.2×10^4 Ω cm. The increase in the resistivity value was due to higher filler loading of MgO nano-powder, which may increase the insulation properties of the prepared film. As stated by Kaushal et al., the increase in resistivity value was due to the pores generated in the film that may absorb and trap the mobile carrier [22]. It can be observed that agglomerated particle was formed on the surface of 3 wt% nano-filler film, which results in formation of intergranular pore, as proved by FESEM. As stated by Hessien et al. the inter-granular pores occurred due to the abnormal grain growth where pores are trapped insides the grains [23]. This suggested that, MgO nano-filler act as a catalyst at 2 wt% loading.

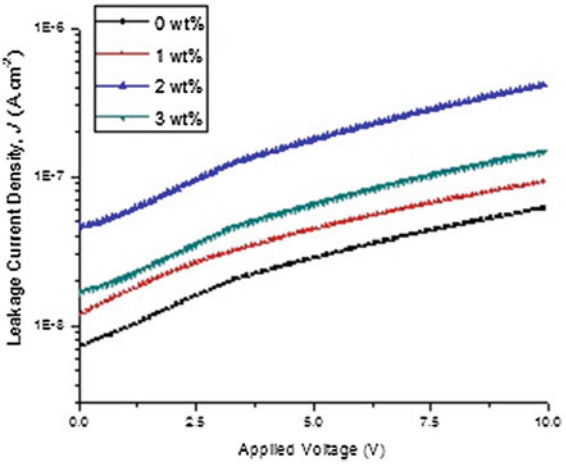

Fig. 5 Leakage current density, J plots with 0.09 cm^2 contact area of deposited nano-MgO at various nano-filler content

The leakage current density, J for the deposited nano-MgO films was shown in Fig. 5 with voltage varied from 0 to 10 V. J values obtained were below than $1E^{-7}$ A cm^{-2}, which was two orders of magnitude lower than common dielectric layer ($SiO_2 \sim 4 \times 10^{-4}$ A cm^{-2}). One of the important characteristics of good dielectric layer is that the J value should be in the order of 10^{-8} A cm^{-2} [24]. Since there are improvements in the J value compared to SiO_2, MgO should be considered to be used as dielectric layer. Study by Bondoux et al. supported this suggestion where their MgO film leakage current density has one order of magnitude lower than SiO_2 [3].

Furthermore, the J values were increased as the loading of the nano-filler increased from 0 to 2 wt%. This was due to its high carrier mobility of the film as proved by resistivity values obtained. Yang et al. reported on the increment in leakage current density of their films as the filler loading were increased [25]. Nevertheless, the J value was slightly decreased when the amount of nano-filler was increased to 3 wt%.

The relative permittivity, ε_r' were measured in frequency ranging from 100 Hz to 10 kHz using Impedance Spectroscopy Analyzer and were measured at room temperature. The results are shownin Fig. 6a. It is apparent from this figure the addition of MgO nano-filler leads to the improvement in the ε_r' value where the ε_r' value increased from 6.72 to 7.33 observed at 40 kHz. Since the filler is in nanometer dimension, the interfacial region becomes dominant where density and charge trapped in the film were improved. Nevertheless, further increase in nano-filler loading to 2 wt% resulted in reduction of ε_r' value to 6.95. However, ε_r' value was slightly increased to 7.18 when the nano-filler loading reached 3 wt%. The changes observed in ε_r' value were due to the changes in the surface morphologies of the prepared films. As can be seen in FESEM images in Fig. 2, nano-MgO film with 2 wt% has less porosity compared to 3 wt% film. Zheng et al. and Praveen Kumar stated that pores in the film obstruct the movement of carriers [26] as well

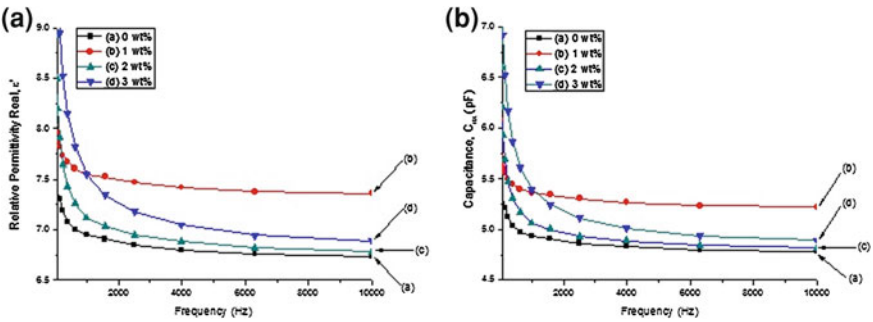

Fig. 6 Variation of **a** Relative Permittivity, ε_r' and **b** Capacitance with respect to frequency

as porosity in the film will reduce the density of the material [27]. Additionally, increased in the ε_r' value with 3 wt% nano-filler loading was due to the defect caused by agglomerated particle produced in the film where more charge was trapped in the film. Agus Purwanto et al. also reported on the large ε_r' value produced in large grain size [28].

Moreover, we also observed that, MgO nano-filler consist of 1 wt% nano-filler has highest ε_r' value compared to others. The enhancement in ε_r' value is most probably due to the inhomogeneous particle formed on the surface of the film. As mentioned before, nanosize particle promotes high surface area and large particle will produce high carrier density. Based on conventional composites rule, the ε_r' value of compound must be higher than matrix ε_r' value [10]. Therefore, in this study, even if there are changes in ε_r' value however, the changes were insignificant because the filler added (MgO nano-powder) was the same type of material with the matrix (MgO film).

From the plotted graph, the frequency were divided into two regions as low frequency region (<10 kHz) and high frequency region (>10 kHz). At low frequency region, the ε_r' values were affected by the interfacial polarization of the material [10, 29]. In this region, the ε_r' values were drastically decreased as the frequency was increased. This was due to dipole moments produced in the film that was caused by the charge trapped at the interface of inhomogeneous particle. At high frequency region, the ε_r' starts to be constant and generally lower compared to the lower frequency, which suggested that at high frequency, dipoles oscillated at a faster speed, thus reducing the time required for polar switching, resulting in the dipole unable to follow the rapid change of applied field. Capacitance versus frequency (*C–F*) was shown in Fig. 6b, which shows quite similar trend observed in ε_r' (Fig. 6a). The obtained capacitance values in this work taken at 20 kHz were tabulated in Table 1. Equation 2, indicated that, capacitance performance was positively related with the ε_r value.

4 Conclusion

The influence of MgO nano-filler loading on the nano-MgO dielectrics properties has been investigated. MgO particle size with nanometer dimension in the range of 42–92 nm were observed using FESEM. It is revealed that the nano-MgO film has good electrical properties with addition of 1 wt% nano-filler. Impedance analysis shows that, there are only small changes in the relative permittivity value since filler and matrix is the same material which is MgO. The surface morphology obtained for 2 wt% film was very uniform and compact.

Acknowledgment The authors were grateful to the financial support from Excellent Grant UiTM (600-RMI/ST/DANA 5/3 Dst (2011/401)) from Research Management Institute (RMI), Universiti Teknologi MARA, UiTM Shah Alam and Ministry of Higher Education (MOHE) Malaysia.

References

1. Ciofi, I., Baklanov, M.R., Tókei, Z., Beyer, G.P.: Capacitance measurements and k-value extractions of low-k films. Microelectron. Eng. **87**, 2391–2406 (2010)
2. Jones, M.N., Kwon, Y.W., Norton, D.P.: Dielectric constant and current transport for HfO_2 thin films on ITO. Appl. Phys. A Mater. Sci. Process. **81**, 285–288 (2005)
3. Bondoux, C., Prené, P., Belleville, P., Guillet, F., Lambert, S., Minot, B., Jérisian, R.: Sol-gel MgO thin films for insulation on SiC. Mater. Sci. Semicond. Process. **7**, 249–252 (2004)
4. Miranda, E., O'Connor, E., Hughes, G., Casey, P., Cherkaoui, K., Monaghan, S., Long, R., O'Connell, D., Hurley, P.K.: Soft breakdown in MgO dielectric layers. In: 2009 IEEE International Reliability Physics Symposium, pp. 688–691 (2009)
5. Raj, A.M.E., Jayachandran, M., Sanjeeviraja, C.: Fabrication techniques and material properties of dielectric MgO thin films—a status review. CIRP J. Manufact. Sci. Technol. **2**, 92–113 (2010)
6. Yi Yin, X.D., Wang, Y., Wang, Q., Li, X.: Charge carrier transportation in the composite of Nano-MgO and cross-linking polyethylene. In: Proceedings of the 9th International Conference on Properties and Applications of Dielectric Materials, pp. 761–764 (2009)
7. Okuzumi, S., Murakami, Y., Nagao, M., Sekiguchi, Y., Reddy, C.C., Murata, Y.: DC Breakdown strength and conduction current of MgO/LDPE composite influenced by filler size. In: Annual Report Conference on Electrical Insulation and Dielectric Phenomena 2008. CEIDP 2008, pp. 722–725 (2008)
8. Murakami, Y., Okazaki, T., Nagao, M., Sekiguchi, Y., Reddy, C.C., Murata, Y.: Space charge formation in low-density polyethylene up to breakdown influenced by addition of MgO nano-filler under DC ramp voltage. In: IEEE Conference on Electrical Insulation and Dielectric Phenomena. CEIDP '09, pp. 685–688 (2009)
9. Murata, Y., Murakami, Y., Nemoto, M., Sekiguchi, Y., Inoue, Y., Kanaoka, M., Hozumi, N., Nagao, M.: Effects of nano-sized MgO-filler on electrical phenomena under DC voltage application in LDPE. In: 2005 Annual Report Conference on Electrical Insulation and Dielectric Phenomena, 2005. CEIDP '05, pp. 158–161 (2005)
10. Singha, S., Thomas, M.J.: Dielectric properties of epoxy nanocomposites. IEEE Trans. Dielectr. Electr. Insul. **15**, 12–23 (2008)
11. Ishimoto, K., Kanegae, E., Ohki, Y., Tanaka, T., Sekiguchi, Y., Murata, Y., Reddy, C.: Superiority of dielectric properties of LDPE/MgO nanocomposites over microcomposites. IEEE Trans. Dielectr. Electr. Insul. **16**, 1735–1742 (2009)

12. Yanjie Su, H.W., Zhou, Z., Yang, Z., Wei, L., Zhang, Y.: Rapid synthesis and characterization of magnesium oxide nanocubes via DC arc discharge. Mater. Lett. **65**, 100–103 (2011)
13. Alavi, M.A., Morsali, A.: Syntheses and characterization of $Mg(OH)_2$ and MgO nanostructures by ultrasonic method. Ultrason. Sonochem. **17**, 441–446 (2010)
14. Xiong, L.M., Chen, Y.P., Lee, J.D.: Atomistic measure of the strength of MgO nanorods. Theoret. Appl. Fract. Mech. **46**, 202–208 (2006)
15. Yacob, A.R., Mustajab, M.K.A.A., Samadi, N.S.: Physical and basic strength of prepared nano structured MgO. In: 2010 2nd International Conference on Mechanical and Electrical Technology (ICMET), pp. 20–23 (2010)
16. Pan, S.S., Ye, C., Teng, X.M., Li, G.H.: Optical properties of MgO–TiO_2 amorphous composite films. J. Appl. Phys. **102**, 013520–013520-5 (2007)
17. Hu, G., Orkoulas, G., Christofides, P.D.: Regulation of film thickness, surface roughness and porosity in thin film growth using deposition rate. Chem. Eng. Sci. **64**, 3903–3913 (2009)
18. Schroder, D.K.: Semiconductor material and device characterization, 3rd edn. Wiley, New Jersey (2005)
19. Simth, C.L.R.C., Landry, M., Nelson, J.K., Schandler, L.S.: The mechanism leading to the useful electrical properties of polymer nanodielectrics. IEEE Trans. Dielectr. Electr. Insul. **15**, 187–196 (2008)
20. Mary, D., Malee, D., Nguyen, M.Q., Werynski, P. Gornicka, B., Therese, L., Guillot, P.: DC conduction current, dielectric strength and electroluminescence of standard, nanofilled and microfilled polyetherimide varnishes. In: IEEE Conference on Electrical Insulation and Dielectric Phenomena, 2009. CEIDP '09, pp. 678–681 (2009)
21. Patil, S., Puri, V.: Oxidation temperature dependent properties of MgO thin film on alumina. Appl. Surf. Sci. **258**, 1535–1540 (2011)
22. Kaushal, A., Kaur, D.: Effect of Mg content on structural, electrical and optical properties of Zn1−xMgxO nanocomposite thin films. Sol. Energy Mater. Sol. Cells **93**, 193–198 (2009)
23. Hessien, M.M., Rashad, M.M., El-Barawy, K., Ibrahim, I.A.: Influence of manganese substitution and annealing temperature on the formation, microstructure and magnetic properties of Mn-Zn ferrites. J. Magn. Magn. Mater. **320**, 1615–1621 (2008)
24. Toomey, B., Cherkaoui, K., Monaghan, S., Djara, V., O'Connor, D., O'Connell, Oberbeck, L., Tois, E., Blomberg, T., Newcomb, S.B., Hurley, P.K.: The structural and electrical characterization of a HfErOx dielectric for MIM capacitor DRAM applications. Microelectron. Eng. **94**, 7–10 (2012)
25. Yang, W., Yu, S., Sun, R., Du, R.: Nano- and microsize effect of CCTO fillers on the dielectric behavior of CCTO/PVDF composites. Acta Mater. **59**, 5593–5602 (2011)
26. Zeng, T., Dong, X., Mao, C., Zhou, Z., Yang, H.: Effects of pore shape and porosity on the properties of porous PZT 95/5 ceramics. J. Eur. Ceram. Soc. **27**, 2025–2029 (2007)
27. Kumar, B.P., Kumar, H.H., Kharat, D.K.: Effect of porosity on dielectric properties and microstructure of porous PZT ceramics. Mater. Sci. Eng. B **127**, 130–133 (2006)
28. Purwanto, A., Wang, W.-N., Lenggoro, I.W., Okuyama, K.: Formation of $BaTiO_3$ nanoparticles from an aqueous precursor by flame-assisted spray pyrolysis. J. Eur. Ceram. Soc. **27**, 4489–4497 (2007)
29. Dang, Y., Wang, Y., Deng, Y., Li, M., Zhang, Y., Zhang, Z.-W.: Enhanced dielectric properties of polypropylene based composite using $Bi2S_3$ nanorod filler. Prog. Nat. Sci. Mater. Int. **21**, 216–220

Nanozeolite Produced by Wet Milling at Different Milling Time

N. Z. F. Mukhtar, M. Z. Borhan, M. Rusop and S. Abdullah

Abstract Recently, there has been a considerable growing interest in utilizing nanozeolites due to their advantages over conventional micron-sized materials. Zeolite particle may be reduced by mechanical treatment such as ball milling or grinding in order to get smaller particles. In this chapter, the effect of milling time on particle size and surface morphology of Zeolite were investigated by a few designed experiments in aqueous environment. Zeta-sizer Nano series of particle sizer, Field Emission Scanning Electron Microscopy (FESEM), and Fourier Transform Infrared Spectroscopy (FTIR) have been used to characterize this nanozeolite. Results shown that, there were changes of particle size and also the surface morphology of Zeolite, while the FTIR spectra showed not much difference; thus, it is confirmed that the milling process does not alter the chemical bonding of this nanozeolite.

1 Introduction

Zeolite is a large group of crystalline materials and has a framework of linked tetrahedral that consists of four oxygen atoms around their cation. Zeolites are also known as molecular sieves and aluminosilicate materials that are characterized by their open structure of interconnected cavities that can be accessed by molecules, atoms, and ions species [1]. The properties and uses of zeolites are being explored in many scientific disciplines: modern inorganic chemistry, physical chemistry,

N. Z. F. Mukhtar (✉) · M. Z. Borhan · M. Rusop
NANO-SciTech Centre Institute of Science, Universiti Teknologi MARA (UiTM), 40450 Shah Alam, Selangor, Malaysia
e-mail: n.zahidatul@gmail.com

N. Z. F. Mukhtar · M. Z. Borhan · S. Abdullah
Faculty of Applied Sciences, Universiti Teknologi MARA (UiTM), 40450 Shah Alam, Selangor, Malaysia

F. L. Gaol and J. Webb (eds.), *Recent Trends in Nanotechnology and Materials Science*, Engineering Materials, DOI: 10.1007/978-3-319-04516-0_4,

colloid chemistry, biochemistry, mineralogy, geology, surface chemistry, oceanography, crystallography, catalysis, and also in chemical engineering process technology [2].

Ball milling treatment, as a cost-lowering and environmentally friendly method has been used in this project at aqueous environment. Ball milling refers to the use of friction, collision, impingement, shear, or other mechanical actions to modify the structures and properties of the Zeolite [3]. The reduction of the particle size of Zeolite causes larger external surface areas available for interaction, shorter diffusion path lengths reducing mass and heat transfer resistances in catalytic and sorption applications, decreasing of reactions, enhancing selectivity, as well as lowering tendencies to coke formation in some catalytic reactions [4, 5].

Therefore, the objective of this study is to investigate the effect of milling time on particle size and surface morphology of Zeolite by wet ball milling treatment through Zeta-sizer Nano series of particle sizer, Field Emission Scanning Electron Microscopy (FESEM) and also Fourier Transform Infrared Spectroscopy (FTIR).

2 Methodology

2.1 Materials

The commercial powders of Zeolite was purchased from Fluka with means size about $\geq$45 μm.

2.2 Ball Milling Treatment

Wet grinding has been selected in this study because it has some advantages over dry grinding such as the higher energy efficiency, lower magnitude of excess enthalpy, and the elimination of dust formation [6]. The milling process was performed by means of a planetary ball mill with some parameters that have been highlighted with respect to size reduction. Grinding time was varied for different experiments between 2 and 8 h while the rotational speeds were constant at 550 rpm for each experiment. All of the experiments were carried out in a 50 mL stainless steel jar with protective jacket of zirconium oxide and 2 mm of zirconium oxide balls were used for this milling process respectively. The grinding jar was set up and arranged eccentrically on the sun wheel of the planetary ball mill and the direction of movement of the sun wheel being opposite to that of grinding jars was selected with the ratio of 1:1. A certain amount of Zeolite: 0.5 g, water: 10 ml, and balls: 45 g were weighted accurately and placed in the jar at room temperature also at atmospheric pressure. The jar was then sealed and imposed to milling. After milling, all samples were carried out, and then allowed to be cooled down at 40 °C for 24 h. Then, all samples were continuing milling for 15 min and then were characterized.

2.3 Characterization

Particles size measurements were carried out using Zeta Nano Sizer S at 25 °C and the reading was taken at 173° scattering angle. Prior to the measurement, 1 ml of nanosuspensions for each samples was taken out and introduced in the disposable cuvette to be measured. The samples were measured in triplicate. The dried powders were taken for FESEM analysis with 50 k in magnification. The freeze dried powders also were taken for FTIR analysis. All measurements were done at 4000–400 cm^{-1} range by Spectrum 400, Perkin Elmer with 30 scans and 110–120 pressure gauges.

3 Results and Discussion

3.1 Particle Sizer

The effects of milling time on particle size of Zeolite were investigated by a few designed experiments in aqueous environment and different time. The particle size distributions of all the Zeolite samples prepared were obtained by Zeta Nano Sizer S, as mentioned before. Figure 1 showed the influences of milling time on zeolite particle. The particle size without milling, the Z-average (mean value in nm) was 1889 nm; then, after milling treatment at 2 h the Z-average was 211.6 nm while for 4, 6 and 8 h were 185.2, 171.4, and 164.9 nm, respectively.

From original Zeolite, it reduced to about 88.80 % of particle size when imposed to milling time at 2 h. Then, the particle size of Zeolite continued to reduce when continuously imposed to milling process until 8 h. Eight hours of milling time showed the smallest average of Zeolite particle size compared to others with reduction about 91.27 % from the original size. From these sizes produced, we observed that the particles size was inversely proportional with grinding time. This closely related to the generation of energy over time during grinding process.

As we can see from Fig. 1, the shorter grinding time will produce larger mean particles compared to the longer grinding time. This result is consistent with the finding by Takatsuka et al. [7], which has found that the particles size reduces with the increasing of running time of grinding. This can be understood from the interaction of particles and the grinding ball.

Interaction occurs between frictional and impact forces due to the collision of ball and inner wall of jar, which move at different speeds, and which will unleash a high dynamic of energies. For a ‘nano’ process to take place, energy in the jar should be sufficient. Fadda et al. [8] have proposed that the particles breakage happens at initial stage of milling; then, equilibrium between re-agglomeration and de-agglomeration occurs.

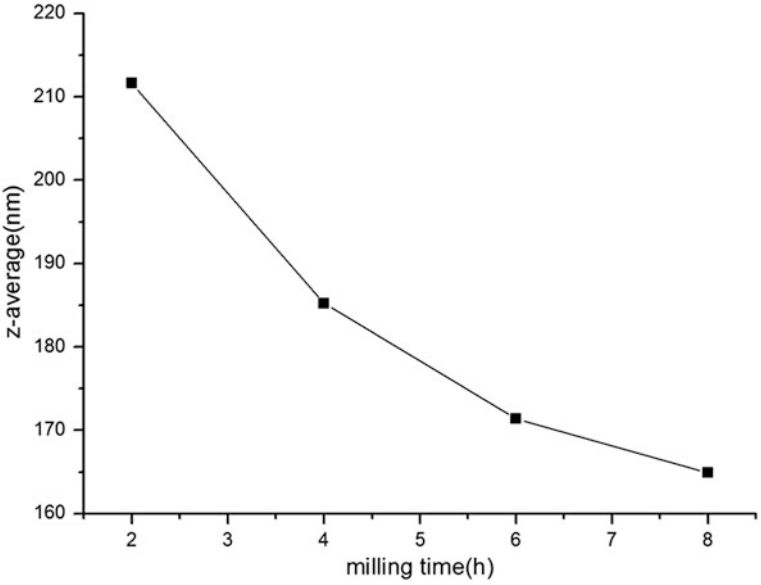

Fig. 1 Average particle size of Zeolite at different milling time

3.2 Surface Morphology

To study probable changes of morphology for ground powders of Zeolite after milling, as well as to confirm the particle size results, all samples were subjected to Field Emission Scanning Electron Microscopy (FESEM). Some of the FESEM images of samples were shown in Fig. 2. FESEM images indicated that almost in all samples, nanozeolite powder with particles size less than 100 nm might be recognized as small particles or in the form of larger grouping particles.

Amir Charkhi et al. [4] also reported the similar phenomenon when grinding Clinoptilolite by a wet ball milling treatment. Moreover, most particles have lost their initial cubic shape (Fig. 2a) and converted into spherical and also irregular shapes after imposed to the milling process with varied in milling times (Fig. 2b–e).

Moreover, Chunlong et al. [9, 10] hypothesized that fractures or de-agglomerations easily happen at the defects, impurities, and at the interface of the intergrowth within large Zeolite particles. Thus, the mechanical stress that was generated by the jar ball mill randomly fractured or de-agglomerated the Zeolite particles into smaller fragment with varying size distribution and different morphology. The larger fragments were of typically irregular shape, whereas the small fragments tended to be spherical. From this observation of Zeolite morphology, we could summarize that FESEM results were in accordance with the characterization results by the particle size analyser that have been explained before.

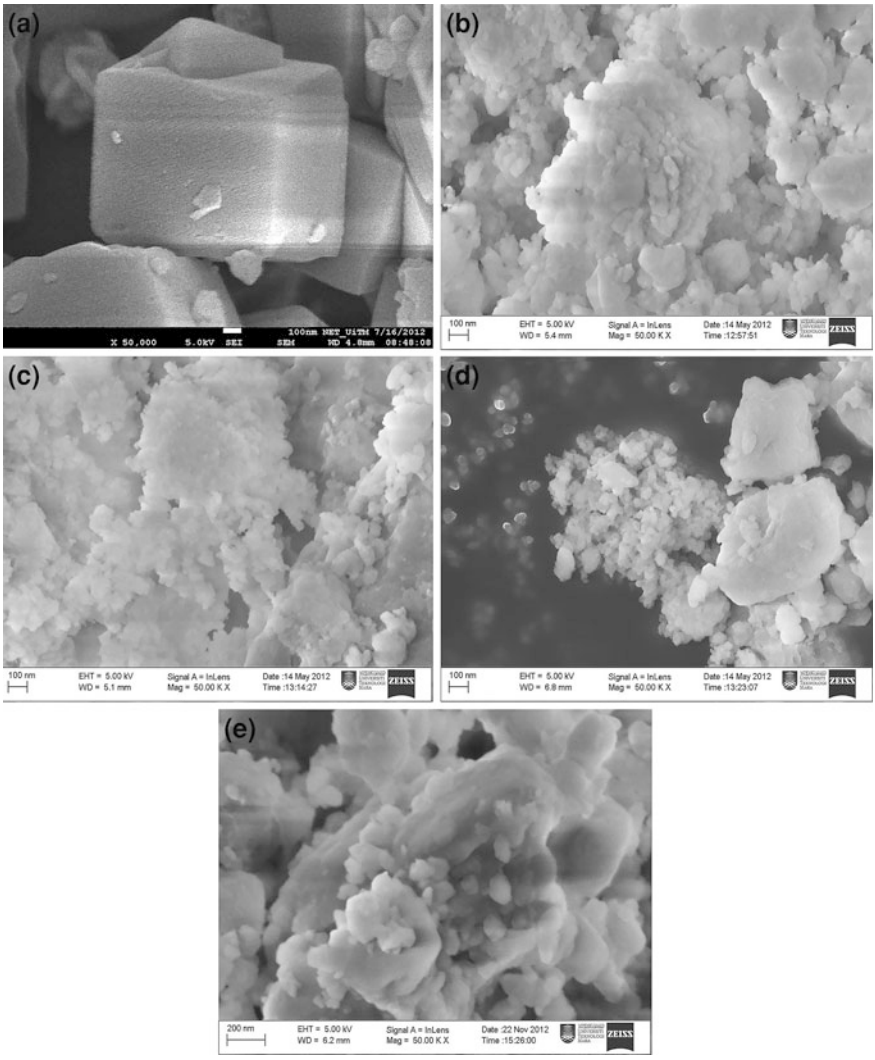

Fig. 2 The surface morphology of nanozeolite as a function of milling time: **a** 0 h, **b** 2 h, **c** 4 h, **d** 6 h, and **e** 8 h

3.3 Structural Information

The structural information of the Zeolite was obtained by FTIR spectroscopy. All measurements were done at 4000–400 cm^{-1} range by Spectrum 400, Perkin Elmer with 30 scans and 110–120 pressure gauges. From the Fig. 3, we can see that the FTIR spectra line for original Zeolite (without milling process) showed four peaks of transmittance vs wavelength at 3360, 1641, 977, and 716 cm^{-1}. Then, after

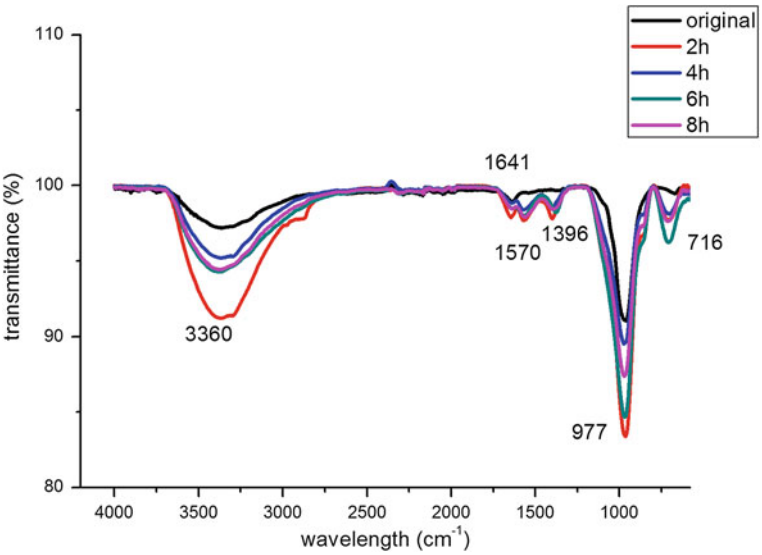

Fig. 3 The FT-IR spectra of nanozeolite at different milling times in range of 700–3400 cm^{-1}

imposed to the wet milling process at 2–8 h, the peaks occurred at 3360, 1641, 1570, 1396, 977, and 716 cm^{-1}. From this spectra, there was no much difference in appearance between the original sample and after milling at the varied times except at 1600–1300 cm^{-1}.

Peaks related with H–bonded O–H stretching at 3,360 cm^{-1} and H_2O bending at 1641 cm^{-1}, respectively [11]. For peak at 1570 and 1396 cm^{-1}, Yuzay et al. [12] and Aronne A et al. [13] stated that this wavelength can be attributed to the asymmetric stretching of the Si–O and Al–O bonds belonging to the SiO_4 and AlO_4 tetrahedral. While T–O stretching at 977 and external T–O at 716 cm^{-1} [11]. From this FT-IR spectroscopy, we expected that the chemical bonding of Zeolite did not change over the milling process with different milling times.

4 Conclusion

As a conclusion for this study we can conclude that at milling time 8 h, the particle size is smaller than others, while for surface morphology, we can observe that the nanozeolite tends to be spherical and also irregular in shape after milling treatment. Therefore, ball milling is a powerful mechanical method to reduce the size of Zeolite particles. The use of FTIR in this study prove that FTIR is a powerful method for checking of chemical bonding. We propose that the condition of milling should be carefully selected to get the nanozeolite powder.

Acknowledgment The authors would like to thank Universiti Teknologi MARA for the financial support. We are grateful to all the staffs of NANO SciTech Centre (NST) and also NANO ElecTronic Centre (NET) for their technical support in this study.

References

1. Vladimir, V.M., Mary, A.W.: Thermal properties of zeolites: effective thermal conductivity of dehydrated powdered zeolite 4A. Mater. Chem. Phys. **75**, 178–180 (2002)
2. Kanokorn, H., et al.: Synthesis of zeolite A from by-product of aluminium etching process: Effects of reaction temperature and reaction time on pore volume. Am. J. Environ. Sci. **7**(1), 35–42 (2011)
3. Tian, Y.L., et al.: The effect of ball milling treatment on structure and porosity of maize starch granule. Innovative Food Sci. Emerg. Technol. **12**, 586–593 (2011)
4. Amir, C., et al.: Optimized experimental design for natural clinoptilolite zeolite ball milling to produce nano powders. Powder Technol. **203**, 389–396 (2010)
5. Kazemian, H., et al.: Synthesis of nano particles of LTA zeolite by means of microemulsion technique. Iran. J. Chem. Chem. Eng. (IJCCE) (2011)
6. Kani, A., et al.: Wet ball milling of zeolite HY. Powder Technology **142**, 121–128 (2004)
7. Takatsuka, et al.: Chem. Pharm. Bull. **57**(10), 1061–1067 (2010)
8. Fadda, et al.: Powder Technol. **194**(3), 207–216 (2009)
9. Chunlong, K., et al.: Zeolite nanocrystas prepared from zeolite microparticles by a centrifugation—assisted grinding method. Chem. Eng. Process. **49**, 809–814 (2010)
10. Pankaj, S., et al.: Synthesis and morphological studies of nanocrystalline MOR type zeolite material. J. Colloid Interface Sci. **325**, 547–557 (2008)
11. Caglar Duverci, O., et al.: Thermal behavior of a zeolitic tuff. Ceram. Int. **33**, 795–801 (2007)
12. Yuzay, I.E., et al.: Effects of synthetic and natural zeolites on morphology and thermal degradation of poly (lactic acid) composites. Polym. Degrad. Stab. **95**, 1769–1777 (2010)
13. Aronne, A., et al.: FTIR study of the thermal transformation of barium-exchanged Zeolite A to celsian. J. Mater. Chem. **12**(10), 3039–3045 (2002)

The Performance of Solid-State Dye Sensitized Solar Cells with Mist-Atomized CuI as the Hole Conductors

M. N. Amalina and M. Rusop

Abstract This research is carried out to investigate the properties of copper (I) iodide (CuI) thin films deposited by using a novel-mist atomization method. The new deposition method of CuI thin films which is by using mist-atomization technique is carried out in order to find the suitability of CuI thin films as a p-type hole conductor for the fabrication of solid-state dye sensitized solar cells. Therefore, in order to understand the cells, behaviour, two different parametric studies of TiO2 porosity and CuI doping are conducted. The optimum porosity of TiO2 was observed to be at 0.24 g of PEG content. Then, for the fabricated device, 0.05M of CuI solution concentration gives the best device efficiency of 1.05% compared to other parameters. While low device efficiency for cells fabricated with doped CuI thin films was observed when compared to the undoped CuI thin films. From the results, it can be concluded that the nano sized CuI particles, which matched to the porous structures of TiO2 layer and electrical conductivity, are the main properties that contributed to the ss-DSSCs device efficiency.

1 Introduction

The solar cells revolution has introduced a series of solar cell generation which brings along the first generation of solar cells (conventional silicon solar cells) to the third generation until now [1]. Among the series of solar cells, the most economical beneficial to develop the solar cell as an alternative to the conventional

M. N. Amalina (✉) · M. Rusop
Faculty of Electrical Engineering, NANO-ElecTronic Centre (NET),
Universiti Teknologi MARA (UiTM), 40450 Shah Alam, Selangor, Malaysia
e-mail: aamalina.muhamad@gmail.com

M. Rusop
NANO-SciTech Centre (NST), Institute of Science, Universiti Teknologi MARA (UiTM),
40450 Shah Alam, Selangor, Malaysia

F. L. Gaol and J. Webb (eds.), *Recent Trends in Nanotechnology and Materials Science*, Engineering Materials, DOI: 10.1007/978-3-319-04516-0_5,

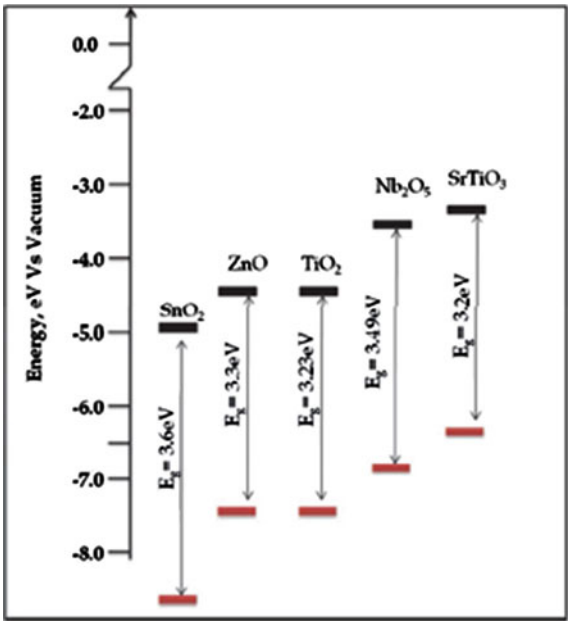

Fig. 1 Energy band diagrams of metal oxides versus vacuum [16]

solar cell is preferable. In the last few years, new concepts of solar cells were conceived and realized. The dye-sensitized solar cells have become an interdisciplinary scientific 'playground' which introduces the separates function of solar light harvesting and charge carrier transport [2]. These technologies mainly include dye-sensitized solar cells (DSSCs), polymer solar cells, and nanocrystalline solar cells, all of which are now known as third generation photovoltaics.

The very first dye sensitized solar cells had been successfully fabricated in 1991 by O'Regan and Gratzel with an efficiency of 7.1–7.9 % under stimulated solar light [3]. This area of work was then become a major attraction since they can be made by using cheap material and do not required a stringent fabrication procedures. This solar cell was constructed with three main element in the cell which is the electron transport, light absorption and hole transport [4, 5]. The paper entitled 'A Low-Cost, High Efficient Solar Cell Based on Dye-Sensitized Colloidal TiO_2 Films' by O'Regan and Gratzel utilizes the anchored dye on a wide band gap of mesoporous TiO_2 semiconductors for the light absorption and redox couple of (I^-/I_3^-) to neutralize the state of oxidized dye and for positive charge transport to the platinized counter electrode [3].

The electron transport material of dye sensitized solar cells usually uses a wide band gap oxide semiconductor such as TiO_2, ZnO, SnO_2, etc. [6–8]. The wide band gap metal oxide semiconductors of above 3 eV of is favorable as the photoanode of DSSC since it have the suitable band position relative to dye sensitizer. Figure 1 shows the several energy levels of metal oxides versus vacuum for DSSCs application. The TiO_2 semiconductor is the most researched material among others. The TiO_2 is the material of choice because it has the lowest

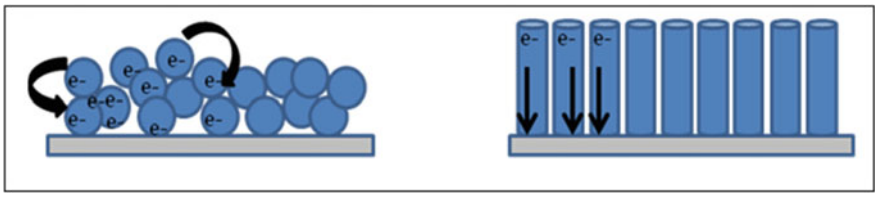

Fig. 2 The electron path of nanoparticles TiO_2 and 1-D nanostructures TiO_2

recombination rate constant in all the oxides [9]. Other wide band gap oxides such as ZnO and SnO_2 are also used due to their higher electron mobility [10]. In DSSCs, the porosity of photoanode is crucial to achieve an optimum dye loading. Therefore, porous nanoparticle structures of oxide materials are one of the most useful materials in use until now [11, 12]. The nanoparticles oxide semiconductor is the heart of DSSC since it will enhance the surface area vacant for dye adsorption. However, usually the porous structures of nanoparticles metal oxides are not densely packed and thus will increase the electron path to the conducting substrate, which might cause interfacial losses. Therefore, research has been done to improve the electron path of photoanode materials by synthesizing 1-D nanostructures such as nanorods and nanotubes, which is vertically aligned to the conductive substrate to cater this issue [13–15]. However, the low surface area of the nanorods has circumvented to obtain high efficiencies of solar cells. Figure 2 shows the electron path of nanoparticles TiO_2 and 1-D nanostructures TiO_2. In this work, the mesoporous structure of TiO_2 was employed in the fabrication of ss-DSSCs. The suitable properties of hole conductors was the aim of this work in order to fabricate an efficient ss-DSSCs.

Another important element in dye sensitized solar cells is the monolayer of dye attached to the metal oxides. The dye molecules are the backbone of the device as it used as the light absorption material. The most commonly used dyes belong to the ruthenium-based metal-organic complexes of polypyridyl ligands. There are three types of dye widely used in the DSSCs research. They are most often referred to with trivial names such as N-3 dye (red dyes), N-749 (red dyes), and Z-907 as black dyes. Currently, other than Ru-based dyes the metal-free organic dyes as has attracted great attention due to its advantages [17]. The examples of organic dyes are coumarin, indoline, squaraine, polyene, cyanine, hemicyanine, oligothiophene, perylene, porphyrin, phthalocyanine, carbazole, benzodithiadiazole, and truxene [18, 19]. Among these dyes, the N3 dyes is used in this research since it possess superior photovoltaic performance [20, 21].

Next, the state of the art of DSSCs device is not complete without the hole transport material (HTM). The HTM is used as the material to regenerate the oxidized state of dye after the photoinjection process to the TiO_2 occurred upon the absorption of photon. There are three types of hole conductor which are liquid electrolyte, quasi solid electrolyte, and solid electrolyte. In the liquid electrolyte solar cells, the iodide-triiodide redox (I^-/I^{3-}) couple is typically used. The achievable efficiency up to date for DSSCs with iodide-triiodide redox (I^-/I^{3-})

couple is about 13.4 % [22]. Despite its high efficiency, liquid electrolyte suffers several technical problems such as solvent evaporation, degradation, and seal imperfection. This organic liquid electrolyte is, however, highly corrosive, volatile, and photo reactive [23]. Besides that, it is also facing a leakage problem due to the interaction between the electrolytes and the sealing materials [23]. Therefore, the stability of using liquid-based DSSCs is limited by the electrolyte encapsulation and its inertness toward the iodine. To cope with this problem, efforts have been done to find the less volatile electrolytes with sufficient hole transport. Hence, ionic liquids, polymer-based electrolytes, and p-type semiconductors are the possible options to replace the liquid electrolyte of redox couple. The quasi solid-state dye-sensitized solar cells used ionic liquid and polymer based as the electrolytes, while for solid-state dye-sensitized solar cells (ss-DSSCs) uses p-type semiconductors as the hole conductors.

2 Solid-State Dye Sensitzed Solar Cells (ss-DSSCs)

The recent progress of ss-DSSCs has reached the power conversion efficiency of about 4–4.8 % [24–26]. Solid-state dye sensitized solar cells (ss-DSSCs) uses solid-state hole conductor for regeneration of dye to replace the liquid electrolytes. The solid-state hole transport material (HTM) includes inorganic and organic material such as CuBr [27], CuSCN [28] and CuI [29]. The first ss-DSSC fabricated by Tennakone had achieved efficiency of 2.4 % by using CuI as the HTM [29]. The low efficiency of solid state based DSSC compared to liquid electrolytes based DSSC is due to the high viscosity of solid-state electrolytes which harden the infiltration between the solid electrolytes and the mesoporous structure of TiO_2. Dye-sensitized solar cells are majority charge carrier devices in which the electron transport occurs in the TiO_2 and the hole transport in the electrolyte. Recombination processes can therefore only occur in the form of surface recombination at the interface.

Despite the challenge faces in the ss-DSSCs, the solid-state DSSC offers workable way for achieving higher efficiency because the quasi Fermi level (QFL) of HTM can be adjusted and hence affect the open circuit voltage of the ss-DSSC. The open circuit voltage can be increased by enlarging the difference between the QFL of TiO_2 and QFL of HTM. However, there are some drawbacks and challenges facing for the ss-DSSC fabrication such as [30]: (1) the need to have HTM with high diffusion and mobility, (2) the need to have low viscosity of HTM for better penetration between the TiO_2 and HTM, (3) improved interfacial junction between the dyed TiO_2 and HTM for appropriate band bending to increase the open circuit voltage (Voc) and short circuit current (Isc). These challenges are the main area of research for ss-DSSC.

The third issue which is to improve the interfacial junction was highlighted. The insufficient pore filling of hole conductor in the porous TiO_2 network is the major challenge in fabrication of ss-DSSCs [31–33]. The intimate contact between

the dyed nanoporous TiO_2 and hole conductor is crucial in order to obtain high efficiency of solar cells. Poor pore filling of nanoporous TiO_2 layer leads to incomplete dye regeneration and hence reduce the photocurrent. Besides that higher series resistance will take place from the bad contact of dyed TiO_2 and hole conductor. Therefore, the reduction of crystallite sizes of hole conductors may help improving the interfacial of photoanode and solid-state hole conductor, which will consequently overcome the problem of hole penetrating the porosity of TiO_2. Besides that, the recombination state in ss-DSSCs is another major issue. Therefore, there is the need to enhance the electron transport to avoid the recombination of electrons and holes [34]. The low electron transport will lead to a less photocurrent since electrons are transported through the structure not fast enough, thus the recombination with positively charged holes in the hole transport material will happen rather electrons moving to electrode to generate electrical current. Therefore, as more hole conductor material is found in the nanopores, the smaller chance for recombination. This is due to the shorter pathway for the chargers toward the electrode are available.

There are two ways of solving this matter which are by increasing the pore size of TiO_2 nanostructures and also by developing a new way of deposition of HTM to increase the penetration percentage of porous TiO_2. Lee et al. had optimized the performance of plastic 'solid-state' dye sensitized solar cells by increase the nanopore filling of solid electrolyte. This is done by fluorine plasma treatment which can increase the size of nanopores and nanochannels and at the same time can passivate the TiO_2 surfaces [23]. Other than enlarging the nanopores, several reports have been made on improving pore filling fraction between the TiO_2 and HTM including by employing counter- strategy which instead filling the HTM into the porous TiO_2 structure, the sensitized TiO_2 was dispersed into the HTM solution [35].

Here the new deposition method of HTM is introduced to form intimate contact between the TiO_2 network and the hole conductor. The mister atomizer is essentially the same film processing technique as so-called spray pyrolysis technique. The most commonly used precursors for spraying technique for an inorganic compound are nitrate, carbonate, sulfate, and chloride [36]. Copper (I) Iodide (CuI) was selected as the solid-state electrolyte since the deposition condition for better properties of CuI is achievable at low temperature (below 150 °C). The low temperature for deposition of HTM is crucial because the monolayer of dye is easily degraded when exposed to high temperature. The aim of this work is to engineer the interface between the mesoporous TiO_2 structure and CuI as the HTM with new novel deposition of CuI which is by mist-atomization method. This is done to overcome insufficient pore filling of mesoporous TiO_2. The morphological properties of CuI play an important role in improving the solid-state dye sensitized solar cells (SSDSSC) performance since it determines the interfacial connection between the dyed TiO_2 and CuI so that dye regeneration can occur.

Many approaches have been done to improve the overall efficiency of ss-DSSC. Doping of hole conductors might give the idea of the materials behavior. In this research, the iodine was used as a dopant for the deposition of CuI. The anionic nonmetal dopants are favorable than cationic dopant because the related impurity

Table 1 Mass variation of polyethylene glycol (PEG) 20,000 in TiO_2 solution

Sample	Mass of PEG 20,000 (g)
S_1	No PEG added (Reference sample)
S_2	0.24
S_3	0.48
S_4	0.72

states are near the valence band edge and do not act as charge carriers [37]. Furthermore, their function as recombination centers might be minimized as compared to cation doping [37]. Besides that, the anionic dopant can act as an electron acceptor that creates holes in the valence band [38]. Other than that, this research also proposed a new method to deposit hole conductor, which is by mister atomizer technique that will hope to improve the pore filling problem between the porous layer of dyed TiO_2 and HTM. This is because, the recombination rate also can be reduced by improved the pore filling fraction between the nano porous layer of TiO_2 and the HTM [34, 39]. Various methods had been done to improve the pore filling penetration, including solution casting, soaking in precursor solution, spin coating, and many more [29, 35, 40].

3 Experimental Procedures

The porous layer of TiO_2 was deposited on the ITO-coated glass by the following method. The TiO_2 paste was made by adding TiO_2 nanopowder (<25 nm, Sigma Aldrich) and absolute ethanol (99 %). After stirred the solution for 30 min, titanium isopropoxide (TTIP, 99.99 %) and polyethylene glycol (PEG) 20,000 were added and stirred for 1 day to obtain a well-dispersed solution. The amount of PEG studied was shown in Table 1. The TiO_2 paste was coated on the ITO coated glass by using spin coating method. The TiO_2 paste was spun at 500 rpm and 2,000 rpm for 15 s and 45 s, respectively. The TiO_2 paste deposition was repeated twice to obtain a thickness of around 6 μm. The TiO_2 film was then annealed at 450 °C for 60 min.

Then, the CuI solution was formed by mixing the precursor of copper (I) iodide powder (ALDRICH, 98 %) with acetonitrile as a solvent and was stirred for 3 h at room temperature. All chemicals were used without any further purification. The iodine which acts as dopant was varied at 10, 20, 30, and 40 mg. Before the deposition, the substrates were preheated at 50 °C in the furnace before the deposition process. This solution was then deposited by mister atomizer to form fine droplets using argon as a carrier gas. The solution volume sprayed was 50 ml for all samples. Then, after deposition process, the films were heated for about 5 min at 50 °C to evaporate the solvent. For the fabrication of TiO_2/dye/CuI solar cells, the TiO_2 thin film was immersed into an ethanolic solution of 0.5 mM N719 dye and was kept at room temperature for 24 h. The CuI was deposited onto the dyed TiO_2

thin film at varied doping concentrations from 10 to 40 mg. The platinized ITO-coated glass substrate was used as the counter electrode. The surface morphology of the films was observed with a field emission scanning electron microscope (JEOL JSM-J600F). The elemental analysis of the cell was carried by energy dispersive X-ray (EDX) spectrometer attached to FESEM (JEOL JSM-J600F). While, the TiO_2 surface area, pore volume, and pore diameter were measured using N_2 gas-adsorption data by Brunauer–Emmett–Teller (BET) method. The electrical properties of CuI thin films have been characterized by 2-point probe current-voltage (*I–V*) measurement by solar simulator CEP 2,000 Spectral Sensitivity Analyzing System. Au was used as metal contacts for *I–V* measurement and deposited using sputter coater (EMITECH K550X). The DSSCs performance was measured using solar simulator device (CEP 2,000). The current density-voltage (*J–V*) characteristics of the solar cells were measured under illumination at 100 mW/cm^2 by using an AM 1.5 solar simulator CEP 2,000 Spectral Sensitivity Analyzing System. The device active area is 0.28 cm^2. The IPCE measurement was done from wavelength 350 nm to 800 nm by using AM 1.5 solar simulators CEP 2,000 Spectral Sensitivity Analyzing System. All of the measurements were done in room ambient.

4 The Porosity Properties of TiO_2 Thin Films for Solid-State Dye Sensitized Solar Cells

The surface morphology of TiO_2 thin films prepared from sol-gel precursor of TiO_2 nanopowder with different percentage of PEG is shown in Fig. 3. From the FESEM images, it is observed that less pores and dense agglomerated particle of TiO_2 particles seen in the Fig. 3a as no PEG was introduced to the TiO_2 solution. Then, as the PEG gradually added to the TiO_2 solution, many fine pores with different sizes and less dense films appear in the PEG modified films. The increased of pore size modified films PEG might be due to the strong photocatalytic activity of TiO_2 thin films [41]. Meanwhile, the shape of TiO_2 crystallites did not change with the addition of PEG. Therefore, it is clearly shows that the TiO_2 films with PEG greatly influence the morphology of the thin films. However, the morphology of pores becomes less different after an optimum weight of PEG content as shown in Fig. 3d. The porosity properties of TiO_2 thin films were crucial in determining the overall performance of ss-DSSCs. The porosity properties will determine the amount of dye loading of the cell as well as the volume of pore penetration between the TiO_2 and hole conductors (e.g., CuI). The effect of porosity to the DSSC cell performance was investigated by Saito et al [42]. They suggest that the morphology especially electrode porosity has great effect to the cells efficiency.

The TiO_2 surface area, pore volume, and pore diameter was determined by using BET method. Table 2 shows the BET analysis of TiO_2 at different PEG content. The results show that the surface area varies significantly, which were

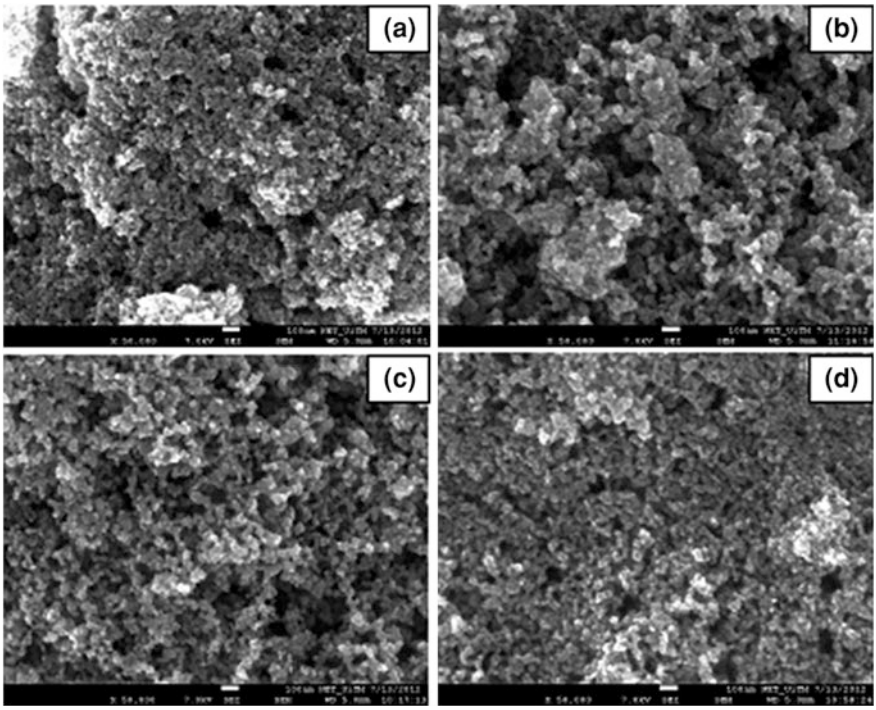

Fig. 3 The FESEM images of TiO_2 at **a** 0 g **b** 0.24 g **c** 0.48 g and **d** 0.72 g of PEG content

Table 2 BET analysis of different TiO_2 samples at different PEG content

Sample of TiO_2	BET surface area (m^2/g)	Pore volume (cm^3/g)	Pore diameter (nm)
Without PEG	50.57	0.29	21.9
PEG 0.24	51.69	0.37	27.5
PEG 0.48	47.10	0.30	24.1
PEG 0.72	51.57	0.33	24.5

around 47.10 m^2/g–51.69 m^2/g. Other than that, the nitrogen adsorption/desorption measurement shows the larger pore volume of 0.37 cm^3/g was obtained for TiO_2 samples with 0.24 g of PEG content. The same trends were also observed for pore diameter results, where the highest pore diameter was observed for 0.24 g PEG content in TiO_2 films. While the TiO_2 films without PEG shows the lowest pore volume and pore diameter. This finding supports the result by FESEM of which by adding the PEG into the TiO_2 colloidal, the porosity properties of the films could be enhanced. The larger diameters and pore size of TiO_2 when PEG was added to the solution was due to the pyrolzation of PEG due to the annealing process [12]. In ss-DSSC application, the optimum point of porosity properties such as surface area, pore volume and pore diameter were crucial in determining the amount of dye

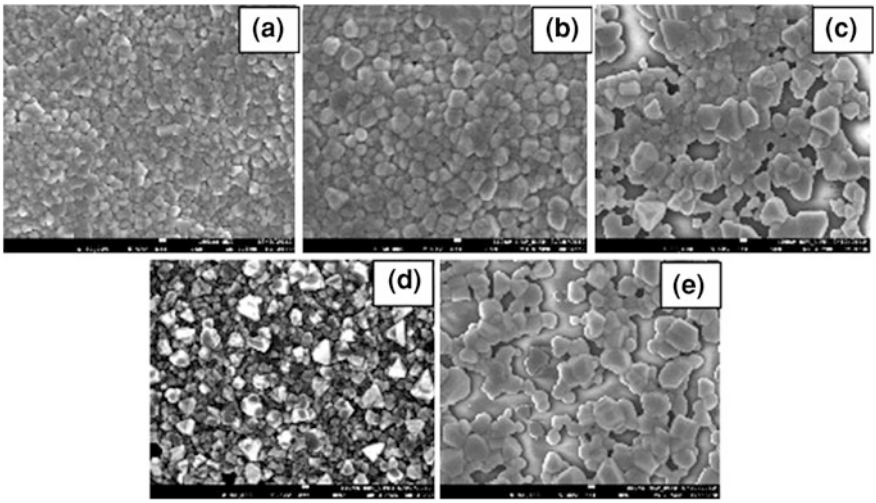

Fig. 4 FESEM images of CuI thin films at **a** undoped thin films and at different weight of I_2 dopant of **b** 10 mg **c** 20 mg **d** 30 mg, and **e** 40 mg

adsorb as well as the suitable properties of hole conductors to filled the porous layer of TiO_2 films. Here, the TiO_2 with 0.24 g added PEG was chosen as the best samples since it has the optimum value of surface area, pore volume, and pore diameter.

5 The Properties of CuI Thin Films for Solid-State Dye Sensitized Solar Cells

The study of the morphology and electrical properties of CuI thin film can be helpful for explaining its suitability in fabrication of ss-DSSC. Figure 4 shows surface morphology of SEM images of CuI thin films at various doping concentration for undoped and doped thin films. It can be seen that, the undoped thin films in Fig. 4a shows good distribution of CuI particle with crystal grains of about 80–150 nm. The existence of brick—like crystals with smooth facets and sharp corners was observed for the doped thin films as shown in Fig. 4b–e. Larger crystal grains of 10 and 20 mg thin films were obtained compared to the undoped thin films. The 20 mg films show poor uniformity of films by having large and small CuI brick-like crystals in the films. When the I_2 dopant increases to 40 mg, the films composed of small brick-like crystals with sharp edges with sizes of about 75–90 nm compared to other doping concentration. This is due to the CuI nuclei formed simultaneously when the iodine concentration was higher, which preferred the growth of the integrated polyhedral CuI crystals on the surface [43].

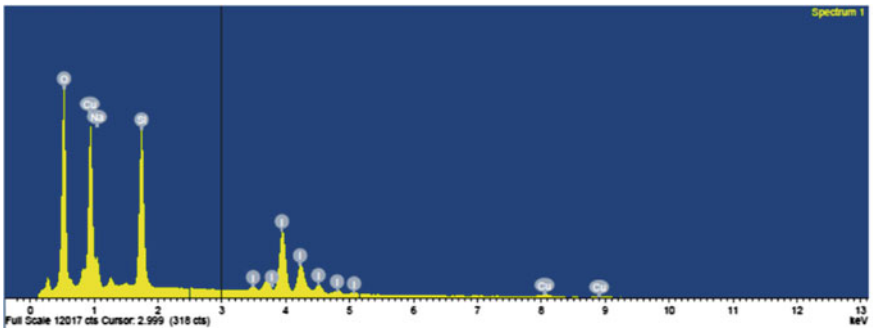

Fig. 5 EDX patterns of the CuI thin films at 40 mg doped CuI thin films

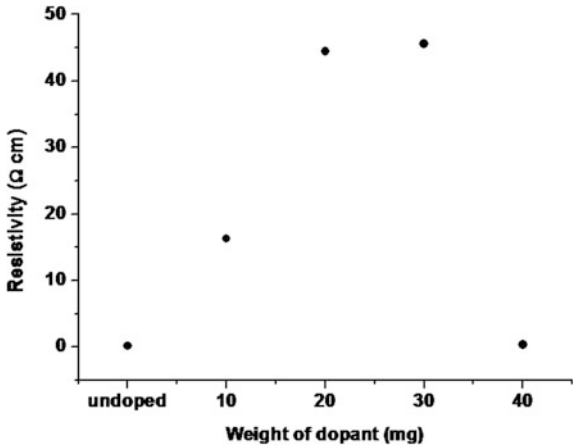

Fig. 6 Resistivity of CuI thin films at different weight of I_2 dopant

Figure 5 shows the EDX spectra of CuI thin films at 40 mg doping concentration. The Na and Si element corresponds to the glass substrate and O element shows the potential of oxidation of the CuI solutions by air. While the Cu:I elements of ratio 27.85:40.89 confirm the existence of CuI thin films.

Figure 6 shows the parabolic resistivity curve of CuI thin films deposited at various doping concentration. It is observed that the resistivity increased up to optimum point at 30 mg and then decreased at doping concentration of 40 mg. The lowest resistivity of 1.8×10^{-1} Ω cm was obtained for undoped samples, while 30 mg iodine doped thin films shows the highest resistivity of 4.56×10^{1} Ω cm. This result is contradictory to the purpose of doping which is to enhance its conductivity. This is may be due to the natural behavior of CuI, which its conductivity is depends on the excess of iodine in the stoichiometric excess due to the acceptor-type copper vacancies (V_{cu}). Therefore, the increment of resistivity for doped thin films may be due to surface traps created above the valence band upon the introduction of iodine atoms. The excess of I_2 atoms in the lattice will create

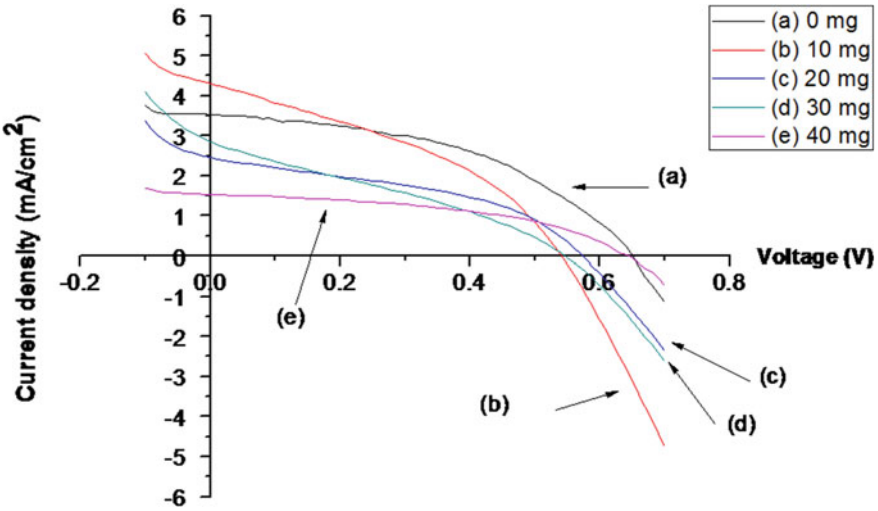

Fig. 7 The *J–V* curves of the TiO_2/dye/CuI solar cell at different weight of I_2 dopant

layer of electrons charge trapping and thus will reduce its mobility. The surface trapping sites is 0.2 eV above the valence band of CuI [44]. However, the low resistivity of CuI thin films at 40 mg of doping concentration may be due to the morphology of the thin film. The low grain boundaries lead to better less carrier scattering and enhances the carrier mobility of CuI atoms.

6 The Photovotaic Performance of TiO_2/Dye/CuI Solid-State Solar Cells

Figure 7 shows current- density (*J–V*) curves of ss-DSSC fabricated at different weight of I_2 doped CuI thin films. The highest efficiency of 1.05 % was recorded for the sample fabricated for undoped CuI thin films. While the lowest conversion efficiency was obtained for solar cells device with the I_2 content of 40 mg with efficiency of 0.45 %. Supposedly, the undoped CuI thin films and 40 mg doped films shows high efficiency compared to others as has been reported earlier in the electrical properties section. The contradictory finding of *I–V* characterization and solar cell performance of 40 mg of I_2 content in CuI thin film may be due the structural properties of the doped films.

From the FESEM images as shown in Fig. 4, the 40 mg doped CuI thin films shows high crystallization of CuI crystals. Even though, low resistivity of CuI thin films was observed at this condition, these 40 mg of I_2 content showed strong tendency to crystallize compared to undoped thin films. The high crystallization of

CuI atoms attributed to the formation of crystal boundaries which will act as barriers of hole transport [45]. The fill factor of the solar cell curves is another point that we can discussed on. Even though the 40 mg fabricated DSSC shows low conversion efficiency, the fill factor of this device is comparable to the undoped CuI which is 0.46 which is the highest fill factor among other samples. The high fill factor indicates low recombination reaction caused by the high conductivity observed for both CuI thin films. From Fig. 7, it could be seen that, as we increased the amount of dopant, the overall performance of the device was slightly decreased. The main factor contributes to the decrease of cell performance is attributed to the pore penetration of CuI onto the dyed TiO_2 layer as well as its hole conductor transfer yield. Hence, the low efficiency of fabricated device at 10, 20 and 30 mg of doped CuI thin films is due to the bigger crystallite size of CuI which will gives poor pore filling between the porous TiO_2 layer and thus increases the recombination reaction in the solar cell device.

7 Conclusion

The properties of hole conductor was important in order to understand the performance of ss-DSSCs. The proper pore filling of hole conductor in the TiO_2 layer can greatly enhanced the regeneration of dye and hence the overall cells efficiency. The optimum porosity properties of TiO_2 were highly favorable to be employed in ss-DSSCs application. The TiO_2 with 0.24 g content of PEG was found to be the optimum value in the fabrication of ss-DSSCs. Then, we have successfully deposited I_2 doped CuI thin films by mist atomization technique at different weight of I_2 dopant to the solar cell performance. The surface and electrical characterization of I_2 doped CuI thin films was determined in order to understand its behavior for the fabrication of ss-DSSC. The FESEM images of CuI thin films reveal the brick-like crystal structure with smooth faces and sharp edges as the I_2 amount increases. Smaller grain sizes were obtained for undoped and 40 mg doped thin films. Meanwhile, for electrical characterization, the smallest resistivity of 10^{-1} Ω cm was shown for undoped thin films and sample doped at 40 mg of I_2 content. The solar cell performance shows the decrement of conversion efficiency as the I_2 dopant increases from 0 to 40 mg. The highest efficiency was obtained for undoped CuI of 1.05 %. The pore filling of porous TiO_2 layer and CuI as well as the crystallization of CuI crystals affects the device performance.

Acknowledgment The authors would like to thank Universiti Teknologi Mara (UiTM) and Ministry of Higher Education (MOHE) and UiTM for the financial support.

References

1. Green, M.A.: Third generation photovoltaics: solar cells for 2020 and beyond. Physica E: Low-Dimens. Syst. Nanostructures **14**, 65–70 (2002)
2. Grätzel, M.: Perspectives for dye-sensitized nanocrystalline solar cells. Prog. Photovoltaics Res. Appl. **8**, 171–185 (2000)
3. Brian O'regan, M.G.: Low cost and highly efficient solar cells based on the sensitization of colloidal titanium dioxide. Nature **353**, 737–740 (1991)
4. Grätzel, M.: Photoelectrochemical cells. Nature **414**, 338–344 (2001)
5. Hagfeldt, A., Grätzel, M.: Molecular photovoltaics. Acc. Chem. Res. **33**, 269–277 (2000)
6. Sauvage, F., et al.: Dye-sensitized solar cells employing a single film of mesoporous TiO_2 beads achieve power conversion efficiencies over 10 %. ACS Nano **4**, 4420–4425 (2010)
7. Bian, J.M., et al.: Preparation of high quality MgO thin films by ultrasonic spray pyrolysis. Appl. Surf. Sci. **228**, 297–301 (2004)
8. Birkel, A., et al.: Highly efficient and stable dye-sensitized solar cells based on SnO_2 nanocrystals prepared by microwave-assisted synthesis. Energy Environ. Sci. **5**, 5392–5400 (2012)
9. Shankar, K., et al.: Recent advances in the use of TiO2 nanotube and nanowire arrays for oxidative photoelectrochemistry. J. Phys. Chem. C **113**, 6327–6359 (2009)
10. Ko, S.H., et al.: Nanoforest of hydrothermally grown hierarchical ZnO nanowires for a high efficiency dye-sensitized solar cell. Nano Lett. **11**, 666–671 (2011)
11. Joshi, P.H., et al.: Optimum oxide thickness for dye-sensitized solar cells—effect of porosity and porous size. A numerical approach. Ionics **19**, 571–576, (2013)
12. Abdullah, M.H., et al.: The influence of TiO_2 photoanode morphology for scattering enhanced properties of dye-sensitized solar cell. Adv. Mater. Res. **667**, 425–434 (2013)
13. Wang, M., et al.: Solid-state dye-sensitized solar cells using ordered TiO_2 nanorods on transparent conductive oxide as photoanodes. J Phys. Chem. C **116**, 3266–3273 (2012)
14. Shalan, A., et al.: A facile low temperature synthesis of TiO_2 nanorods for high efficiency dye sensitized solar cells. Appl. Phys. A **110**, 111–122 (2013)
15. Lee, J.-G., et al.: Photovoltaic performance of dye-sensitized solar cell low temperature growth of Zno nanorods using chemical bath deposition. J. Nanosci. Nanotechnol. **12**, 3469–3472 (2012)
16. Lee, J.-J., et al.: Metal oxides and their composites for the photoelectrode of dye sensitized solar cells. Compos. Mater. Med. Nanotechnol. **8**, 181–210 (2008)
17. Ooyama, Y., Harima, Y.: Molecular designs and syntheses of organic dyes for dye-sensitized solar cells. Eur. J. Org. Chem. **2009**, 2903–2934 (2009)
18. Zeng, W., et al.: Efficient dye-sensitized solar cells with an organic photosensitizer featuring orderly conjugated ethylenedioxythiophene and dithienosilole blocks. Chem. Mater. **22**, 1915–1925 (2010)
19. Mishra, A., et al.: Metal-free organic dyes for dye-sensitized solar cells: from structure: property relationships to design rules. Angew. Chem. Int. Ed. **48**, 2474–2499 (2009)
20. Jang, S.R., et al.: Linkage of N3 dye to N3 dye on nanocrystalline TiO_2 through trans-1, 2-bis(4-pyridyl)ethylene for enhancement of photocurrent of dye-sensitized solar cells. Chem. Commun. 103–105 (2006)
21. Grätzel, M.: Conversion of sunlight to electric power by nanocrystalline dye-sensitized solar cells. J. Photochem. Photobiol. A **164**, 3–14 (2004)
22. Cai, N., et al.: An organic D-π-A dye for record efficiency solid-state sensitized heterojunction solar cells. Nano Lett. **11**, 1452–1456 (2011)
23. Chung, I., et al.: All-solid-state dye-sensitized solar cells with high efficiency. Nature **485**, 486–489 (2012)
24. Schmidt-Mende, L., et al.: Organic dye for highly efficient solid-state dye-sensitized solar cells. Adv. Mater. **17**, 813–815 (2005)

25. Snaith, H.J., et al.: Efficiency enhancements in solid-state hybrid solar cells via reduced charge recombination and increased light capture. Nano Lett. **7**, 3372–3376 (2007)
26. Wang, M., et al.: Efficient and stable solid-state dye-sensitized solar cells based on a high-molar-extinction-coefficient sensitizer. Small **6**, 319–324 (2010)
27. Tennakone, K., et al.: Highly stable dye-sensitized solid-state solar cell with the semiconductor 4CuBr 3S(C4H9)2 as the hole collector. Appl. Phys. Lett. **77**, 2367–2369 (2000)
28. O'Regan, B., Schwartz, D.T.: Large enhancement in photocurrent efficiency caused by UV illumination of the dye-sensitized heterojunction TiO_2/RuLL'NCS/CuSCN: initiation and potential mechanisms. Chem. Mater. **10**, 1501–1509 (1998)
29. G.R. R. A. K., Tennakone, K., Kumarasinghe, A.R., Wijayantha, K.G.U. Sirimanne, P.M.: A dye-sensitized nano-porous solid-state photovoltaic cell. Semicond. Sci. Technol. **10**, 1689 (1995)
30. Lee, B., et al.: Optimizing the performance of a plastic dye-sensitized solar cell. J. Phys. Chem. C **115**, 9787–9796 (2012)
31. Lenzmann, F., Kroon, J.: Recent advances in dye-sensitized solar cells. Advan. OptoElectron. **2007** (2007)
32. Konno, A., et al.: The effect of particle size and conductivity of CuI layer on the performance of solid-state dye-sensitized photovoltaic cells. Curr. Appl. Phys. **5**, 149–151 (2005)
33. Sirimanne, P., et al.: On the photo-degradation of dye sensitized solid-state TiO_2|dye| CuI cells. Semicond. Sci. Technol. **18**, 708 (2003)
34. Schmidt-Mende, L., Grätzel, M.: TiO_2 pore-filling and its effect on the efficiency of solid-state dye-sensitized solar cells. Thin Solid Films **500**, 296–301 (2006)
35. Zhenzhen, Y., et al.: Solid dye-sensitized solar cells prepared through a counter strategy for filling of solid hole transporter. J. Renew. Sustain. Energy **3**, 063101
36. Jung, D., et al.: Design of particles by spray pyrolysis and recent progress in its application. Korean J. Chem. Eng. **27**, 1621–1645 (2010)
37. Ding, J., et al.: TiO_2 nanopowder Co-doped with iodine and Boron to enhance visible-light photocatalytic activity. J. Biomed. Nanotechnol. **5**, 1–7 (2009)
38. Rusop, M., et al.: Properties of CuI films in the power output of TiO/sub 2/|Dye|CuI cells. In: Proceedings of 3rd World Conference on Photovoltaic Energy Conversion, vol. 1, pp. 140–143 (2003)
39. Liang, L., et al.: Porosity effects on electron transport in TiO_2 films and its application to dye-sensitized solar cells. J. Phys. Chem. B **110**, 12404–12409 (2006)
40. Ding, I.K., et al.: Pore-filling of spiro-OMeTAD in solid-state dye sensitized solar cells: quantification, mechanism, and consequences for device performance. Adv. Funct. Mater. **19**, 2431–2436 (2009)
41. Jahromi, H.S., et al.: Effects of pH and polyethylene glycol on surface morphology of TiO_2 thin film. Surf. Coat. Technol. **203**, 1991–1996 (2009)
42. Saito, Y., et al.: Morphology control of mesoporous TiO_2 nanocrystalline films for performance of dye-sensitized solar cells. Sol. Energy Mater. Sol. Cells **83**, 1–13 (2004)
43. Huang, B., et al.: A rapid sonochemical approach to semiconductor thin films: The case of metal iodides. Solid State Ion **179**, 2006–2010 (2008)
44. Perera, V.P.S., Tennakone, K.: Recombination processes in dye-sensitized solid-state solar cells with CuI as the hole collector. Sol. Energy Mater. Sol. Cells **79**, 249–255 (2003)
45. Kroeze, J.E., et al.: Parameters influencing charge separation in solid-state dye-sensitized solar cells using novel hole conductors. Adv. Funct. Mater. **16**, 1832–1838 (2006)

Sound Absorption Properties of a Low Density Date Palm Fibers Panel

A. K. Elwaleed, N. Nikabdullah, M. J. M. Nor, M. F. M. Tahir and R. Zulkifli

Abstract Sound absorption properties of a natural waste of a date palm fiber panel have been presented in this chapter. The measurements were carried out for a single-layer sample using an impedance tube. The experiments were conducted for the panel with and without perforated plate facing. Three air gap thicknesses of 10, 20, and 30 mm were used between the date palm fiber sample and the rigid backing of the impedance tube to study the effect of the air gap on the panel sound absorption. An improvement in the sound absorption coefficient at higher and lower frequency ranges is found when facing the palm date fiber sample with perforated plate. Further investigation was carried out to test the effect of air gap backing and perforated plate facing combination on the sound absorption coefficient of the date palm fiber sample.

1 Introduction

Noise can be defined as unwanted sound and it can be hazardous to hearing. Noise absorption is the process of converting the sound wave energy into heat. Noise absorbing materials can be classified as Helmholtz resonators, porous absorbers, and membrane resonators. Noise is generally controlled using glass wool, foams, fabrics, and polymer fibers, which are non-biodegradable. Increasing environmental concerns over the greenhouse effect have encouraged researchers to look for sustainable materials that can replace synthetic fibers. Natural fibers have gained

A. K. Elwaleed (✉) · N. Nikabdullah
Institute of Space Science, Universiti Kebangsaan Malaysia, 43600 Bangi, Selangor DE, Malaysia
e-mail: elwaleed@vlsi.eng.ukm.my

M. J. M. Nor · M. F. M. Tahir · R. Zulkifli
Department of Mechanical and Materials Engineering, Faculty of Engineering and Built Environment, Universiti Kebangsaan Malaysia, 43600 Bangi, Selangor DE, Malaysia

F. L. Gaol and J. Webb (eds.), *Recent Trends in Nanotechnology and Materials Science*, Engineering Materials, DOI: 10.1007/978-3-319-04516-0_6,

popularity as a potential alternative due to their availability and low cost of extraction from plants. Recently there has been increased research on the potential for using natural fibers as sound absorbing materials. They have been widely used as sound absorbing materials in many applications including building, vehicles, and industry. This represents a major need for human comfort and safety. Many types of natural fibers have been investigated extensively for acoustic absorption purposes, such as bamboo, coconut coir fiber, tea leaf fiber, and rice straws.

The factors affecting sound absorption of fibers are the fiber size, layer thickness, flow resistivity, density, porosity, and tortuosity. However, the sound absorption of a specific layer can be improved by adding an air gap between the layer and the backing or by facing the layer with a perforated surface. The enhancement of the sound absorption coefficient of a low density date palm fiber is presented in this chapter. This is investigated by varying the air gap thickness and facing the date palm layer with a perforated plate.

2 Background

Porous sound absorbing materials are widely used in noise control engineering. Porous materials based on their microscopic configurations can be classified as cellular, fibrous, or granular [1]. Vegetable fiber is one of the varieties of natural fibers obtained from stems, leaves, roots, fruits, and seeds of plants. However, from commercial and technological points of view, cotton, kenaf, sisal, flax, palm, coir, arecanut, and banana fibers acquire utmost significance, since reinforced plastics, strings, cords, cables, ropes, mats, brushes, hats, baskets, and fancy articles such as bags are manufactured with these fibers [2]. Fibrous materials have been widely used as acoustic absorbing materials in many applications such as vehicles and buildings [3]. The date palm is one of the most cultivated palms around the world. It geographically covers the deserts from the Atlantic coastline of Mauritania to India and from the Mediterranean Sea to about 15^{o} north of the equator of the earth in Africa. The main date-producing countries of the world are Iraq, Saudi Arabia, Egypt, Iran, Algeria, Pakistan, and Sudan. The date palm in Sudan is common in northern Sudan along the Nile [4]. Date palms have a fibrous structure with four types of fibers: leaf fibers in the peduncle, baste fibers in the stem, wood fibers in the trunk, and surface fibers around the trunk [5]. Al-Sulaiman [6] evaluated the performance of the date palm fiber as wetted pads in evaporative cooling. Riahi et al. [7] investigated the application of date palm fibers filters as porous medium for tertiary domestic wastewater treatment.

Sound absorbing products used in the building construction industry consist of glass or mineral fiber materials. However, the growing concern about the potential health risks popularly seen as being associated with glass or mineral fiber materials provides an opportunity to develop sound absorption panels made of natural fibers. Researches have been conducted in developing particle composite boards using agricultural wastes. Khedari et al. [8] developed particle composite boards using

combinations of durian peel and coir fiber straw particles as an insulation board in the wooden construction industry. Yang et al. [9] reported that the sound absorption coefficient of rice straw-wood particle composite boards are higher than other wood-based materials in the 500–8,000 Hz frequency range, which is caused by the low specific gravity of composite boards that are more porous than other wood-based materials. From the view of environmental protection, natural bamboo fibers were used for sound absorbing purposes. Impedance tube measurement of bamboo fiber samples, revealed properties similar to that of glass wool. Bamboo material formed into a fiber board yields a superior sound absorption property when compared to plywood material of similar density [10]. Ersoy and Kucuk [11] experimentally investigated the sound absorption feature of tea leaf fiber as an industrial waste material. The good acoustic absorption aspect of that fiber with respect to other absorbers was noticed. Coconut is one of the most important harvests in Malaysia. Coir fiber from coconut husk is one of the hardest natural fibers having high amount of lignin. The sound absorption attribute of coir fiber was investigated previously in Automotive Research Group laboratories, Universiti Kebangsaan, Malaysia. These studies covered experimental observations in a reverberation room [12] and using impedance tube [13].

The acoustic properties of panels can be improved by using air gap and perforated plate design. Micro-perforated panel absorbers were first described by [14]. Davern [15] investigated the effect of the air space layers, perforated plate, and porosity on the acoustic properties of materials. He observed that the porosity of the perforated plate and the density of the porous material significantly affected the acoustic impedance and sound absorption coefficient of the panel, in which case, the frequency band near the resonance frequency achieved high acoustic absorption. The potential use of micro-perforated absorbers and their possible applications were addressed by [16]. Lee and Chen [17] found that the acoustic absorption of multilayer materials is better with a perforated plate backed with airspaces. The enhancement of coir fiber acoustical absorption using perforated plates and air gap layers was studied [18, 19] using a reverberation room and impedance tube, respectively. The research on the acoustical properties of the date palm fibers started at the University of Khartoum [20].

Many models are available for predicting the acoustical characteristics of fibrous materials [21–29]. The best-known empirical model is that of [30], who proposed simple power-law relations obtained by fitting a large amount of experimental data. They developed a simple semi-empirical approach that is still a good and fast approximation to the solution based on the air flow resistivity. Dunn and Davern [22] followed the same method to propose empirical relations between characteristics impedance and propagation constant of foam materials. Qunli [23] developed an empirical model for open cell plastic foam materials based on a gathered large amount of experimental data with a wider range of flow resistivity. Miki [24] derived an empirical model based on Delany and Bazley experimental data with a modification to avoid the convergence of the real part of surface impedance to negative values at low frequencies. Allard [28] introduced a model based on flow resistivity, porosity, tortuosity, and shape factors which are related to viscous and

thermal characteristic lengths. The aim of this research is to study the potential use of the date palm fibers as a sound absorption material and to investigate the effect of using air gap and perforated plate on the sound absorption coefficient.

2.1 Delany and Bazley Model

A number of models are available for predicting the acoustical characteristics of fibrous materials. The most known model was introduced by Delany and Bazley [30]. The sound absorption analysis for the date palm fiber sample used in this study was performed using the Delany and Bazley model. The model predicts the sound absorption coefficient (α) based on the frequency (f) and the flow resistivity of the material. The model was derived by empirical equations for the complex propagation coefficient (Γ) and the complex characteristic impedance (Z_c) of the material which may be written as:

$$Z_c = \rho_o c_o \left[1 + 0.0571 * E^{-0.754} - j * 0.087 * E^{-0.732}\right] \tag{1}$$

$$\Gamma = \frac{\omega}{c_o}\left[1 + 0.0978 * E^{-0.700} - j * 0.189 * E^{-0.595}\right] \tag{2}$$

where

ρ_o = the air density
c_o = speed of sound in air (m/s)
j = unit imaginary number = $\sqrt{-1}$
$E = \frac{\rho_o * f}{\sigma}$
σ = the flow resistivity

The sound absorption coefficient is given as

$$\alpha = 1 - |R|^2 \tag{3}$$

with R defined in the following relationship:

$$\frac{Z_c \coth(\Gamma b)}{\rho_o c_o} = \frac{1 + R}{1 - R}$$

b = the sample thickness.

Flow resistivity of date palm fiber sample was estimated using the following empirical equation (Ballagh 1996):

$$\sigma = 490 \frac{\rho^{1.61}}{d} \tag{4}$$

where

ρ = is the bulk density of the fiber
d = is the date palm fiber diameter.

3 Date Palm Fiber

The date palm fiber used in this research is collected from the sheathing leaf base, which surrounds the stem (Fig. 1). It has a netted structure that is covered by soft or ground tissues. It is collected from the tree and dried in shade at room temperature for a period of 2 days to remove any excess moisture content. The pulp which is present on the individual fiber is removed by combing. The fiber is then scraped to remove the pulp completely. The average values for density and fiber diameter were obtained from 30 randomly selected samples. The average diameter and density of the fibers are 0.408 mm and 919 kg/m^3, respectively.

The samples were prepared using two plastic molds. The molds were fabricated to prepare samples of two different sizes equivalent to the diameters of the impedance tubes to cover the low and high frequency range of measurements. Figure 2 shows the plastic molds and samples of date palm fibers for both sizes. The samples were prepared for the same thickness and density to obtain consistent results. The thickness and the density of the prepared samples are 30 mm and 77 kg/m^3, respectively.

4 Sound Absorption Measurements

Sound absorption properties of a material can be measured using either reverberation rooms or impedance tubes. In this research the experiment was conducted using two impedance tubes of 28 mm and 100 mm diameter, noise generator, two channel data acquisition system 01 dB, two ¼ in microphones type GRAS-40BP in each tube, software package SCS8100 [31] The measurements were made based on ISO 10534-2 standard [32]. The microphones' sensitivity was calibrated using calibrator type GRAS-42AB at 114 dB level and 1 kHz. The photograph of the system is shown in Fig. 3. The noise generator transmitted a random noise into the tubes. Interior sound pressure spectrum was measured by the two microphones and transfer functions between them were calculated. The acoustical absorption coefficient was calculated from these transfer functions and distances between the microphones and date palm fiber sample. The frequency span of the experiment was 100–5,000 Hz with 3 Hz resolution. Before running the experiment the two impedance tube microphones were calibrated relatively to each other using the standard switching technique. This was based on mounting the sample in the sample holder and conducting the measurement to make sure that the sound field inside the tube was well-defined.

Fig. 1 Date palm amplexiaul

Fig. 2 Plastic molds and date palm fiber samples

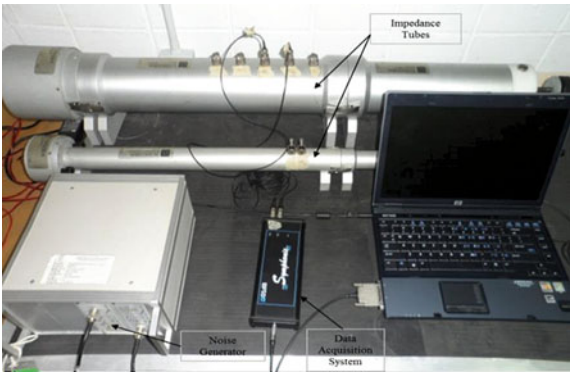

Fig. 3 Sound absorption experimental setup

Three air gap thicknesses of 10, 20, and 30 mm were used between the date palm fiber sample and the rigid backing of the impedance tube The perforated plate (PP) used as a facing for the date palm fiber sample is shown in Fig. 4. The

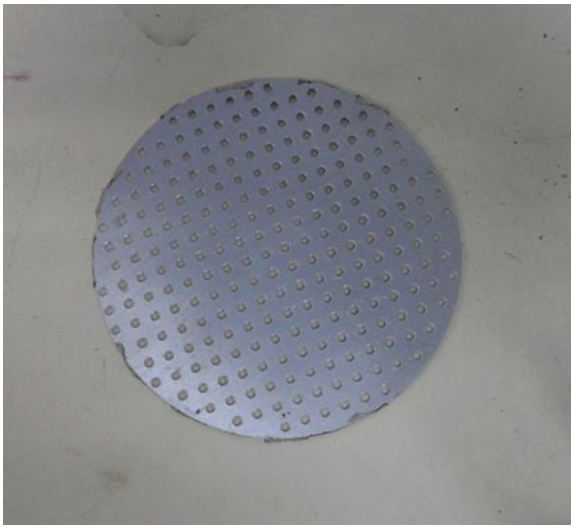

Fig. 4 Aluminum perforated plate (PP)

main purpose of using the PP facing is to enhance the sound absorption of the fiber. The PP was made of aluminum. The experiment was conducted for the panel without air gap, with air gap and with PP facing.

5 Sound Absorption of Date Palm Fiber

5.1 Sound Absorption of a Single Layer

The general behavior of the sound absorption of the low density date palm fiber panel was investigated using impedance tube. The sample positioning inside the tube is shown in Fig. 5. A simulation for the sample was performed using the Delany and Bazley model. The experimental and simulation results of the sound absorption coefficient for the date palm sample are shown in Fig. 6. The experimental results show that the sound absorption coefficient increases with increasing the frequency until the peak at 3,000 Hz. A good agreement, between the experimental and the simulation results, can be observed before the peak. However, after the peak the sound absorption coefficient obtained experimentally decreases with increasing the frequency.

5.2 Effect of Air Gap

In this section the influence of the air gap layer between the date palm fiber sample and the rigid backing of the impedance tube was studied. The configuration is shown in Fig. 7. The effect of varying the air gap distance, between the date palm

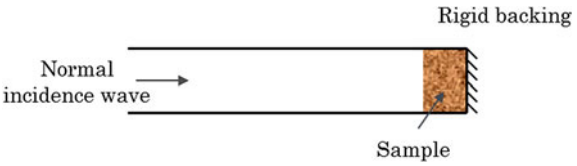

Fig. 5 Sketch of the palm date fibers sample inside the impedance tube with rigid backing

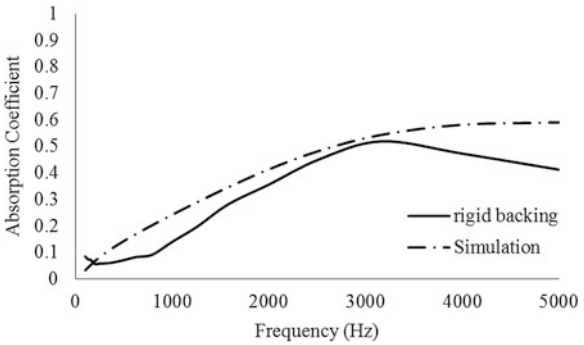

Fig. 6 Experimental and simulation results for the absorption coefficient of the date palm fiber

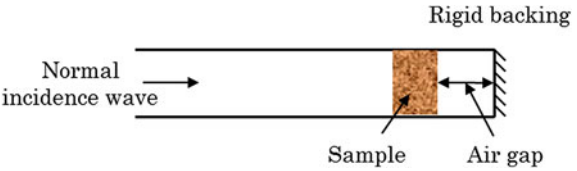

Fig. 7 Sketch of the palm date fibers sample inside the impedance tube backed with an air gap layer

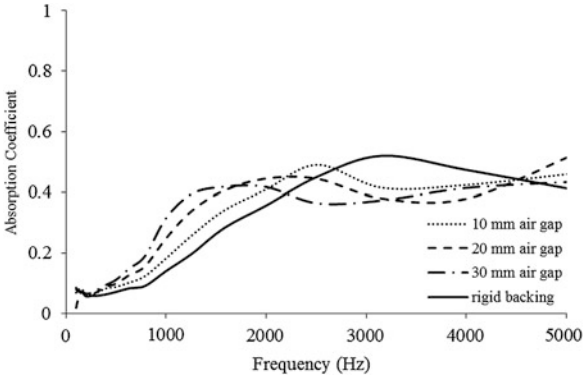

Fig. 8 Sound absorption coefficient for the date palm fiber with and without air-gap

fiber sample and the back wall, on sound absorption coefficient is shown in Fig. 8. It can be seen that introducing air gap between the sample and the rigid backing of the impedance tube can be useful for increasing the absorption coefficient at some lower frequencies range. The general indication is that air gap shifts the resonance absorption toward the low frequency range. Below 2,500 Hz frequency there is an improvement in the sound absorption coefficient for all air gap thicknesses. It can be

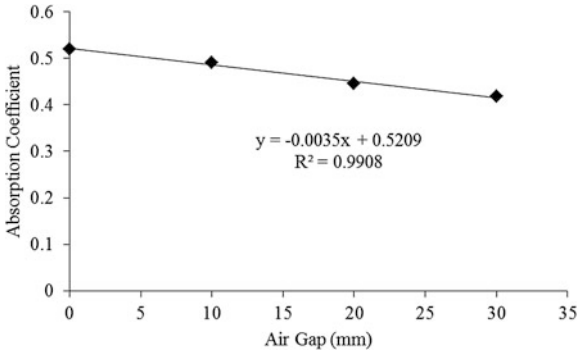

Fig. 9 Sound absorption coefficient for the date palm fiber with and without air-gap

Table 1 Effect of increasing the air gap on the sound absorption coefficient

Air gap (mm)	The peak absorption coefficient	Frequency of peak absorption coefficient	Reduction of peak absorption coefficient (%)	Absorption coefficient at 1,580 Hz	Increase of absorption coefficient at 1,580 Hz (%)
0	0.52	3160	–	0.28	–
10	0.49	2,514	6	0.34	21
20	0.45	2,000	13	0.41	46
30	0.42	1,580	19	0.42	50

observed that the increase in the air gap thickness moved the peaks toward lower frequencies and improved the low frequencies absorption and above the 4,500 Hz. However, that increase coincided with reduction in medium frequency absorption and reduction in the peak. Figure 9 shows the variation of sound absorption peak with the frequency. The trend of the variation was found to be linear with coefficient of regression of 0.99. The percentage reduction of the absorption peak for the three air gap thicknesses is shown in Table 1. The table also shows the increase in the sound absorption coefficient at 1,580 Hz for all air gap thicknesses.

Noise reduction coefficient (NRC), which is a simple quantification of absorption of sound by material, is normally calculated for the range of frequencies below 2,500 Hz. From Fig. 7 it could be observed that the NRC increases by increasing the air gap thickness. As reported by Fatima and Mohanty [33] this increase is due to loss of acoustical wave energy of transmitted wave in the presence of sample-air passage and of reflected wave from rigid backing, through air-sample passage in the propagation of acoustical wave.

5.3 Effect of Perforation

The effect of using perforated plate facing on the sound absorption of the palm date fiber is discussed in this section. Figure 10 shows a sketch of the date palm fiber sample and the perforated plate. The variation in the measured sound

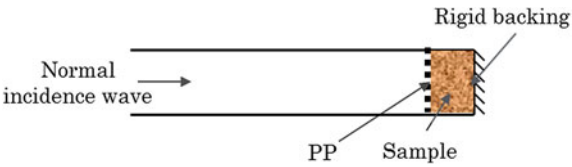

Fig. 10 Sketch of the palm date fibers sample inside the impedance tube with rigid backing and perforated plate facing

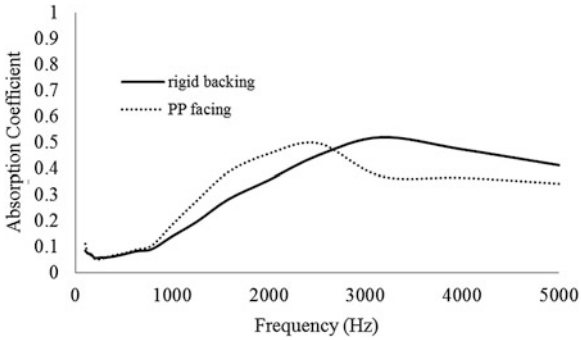

Fig. 11 Sound absorption coefficient for the date palm fiber with and without air-gap

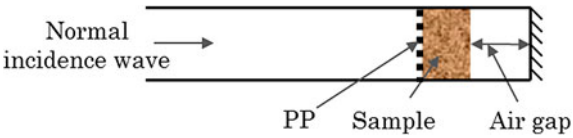

Fig. 12 Combination of the palm date fibers sample, air gap backing, and perforated plate facing inside the impedance tube

absorption coefficient as a function of frequency for the date palm sample, with and without perforated plate facing, is shown in Fig. 11. It can be observed that the sound absorption coefficient increased between 1,000 and 3,000 Hz by shifting the peak toward the lower frequency range. However, the sound absorption coefficient decreased above 3,000 Hz and the peak decreased by 4 %.

Further investigation was carried out to test the effect of air gap backing and perforated plate facing combination on the sound absorption coefficient for the date palm fiber sample. Figure 12 shows a configuration the date palm fiber sample, air gap layer, and the perforated plate. The results from Fig. 13 show the sound absorption for the palm date fiber with rigid backing, PP facing, and a combination of PP facing and 10 mm air gap backing. The results show that the best performance for improving the sound absorption at the low frequency range can be obtained using the palm date fiber combined with the PP facing and the 10 mm air gap backing. However, this is coincided with a decrease in the sound absorption at the medium frequency range.

Increasing the air gap thickness between the date palm fiber and the impedance tube rigid backing results in more improvement in the sound absorption of the date palm fiber in the lower and higher frequency ranges (Fig. 14). It can be observed that increasing the air gap thickness can be useful for increasing the absorption

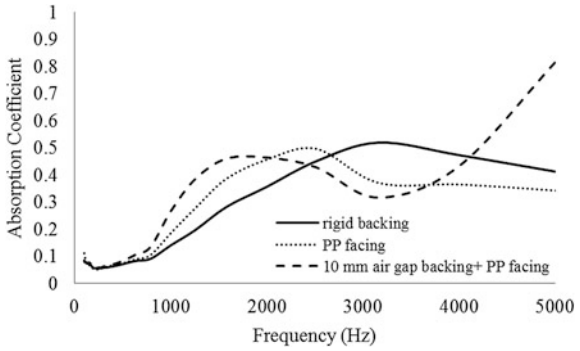

Fig. 13 Sound absorption for the palm date fiber with rigid backing, PP facing and a combination of PP facing and 10 mm air gap backing

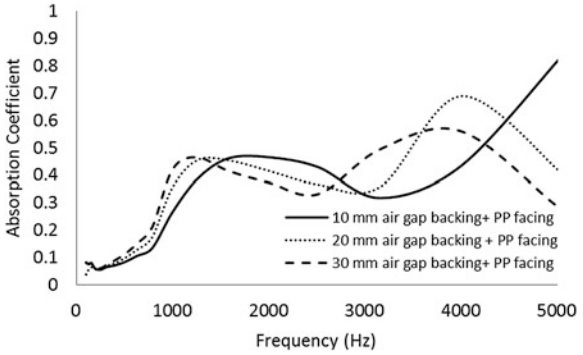

Fig. 14 Absorption coefficient for the palm date fiber with PP facing for different air gap backing thicknesses

coefficient at some lower frequencies range. The general indication is that air-gap shifts the resonance absorption toward the low frequency range. Below 1,500 Hz frequency there is improvement in sound absorption coefficient for all air gap thicknesses. It can be observed that the increase in the air gap thickness moved the peaks toward lower frequencies and improved the low frequencies absorption above 4,000 Hz (Fig. 14). However, this increase coincided with reduction in medium frequency absorption. To compare the performance of the date palm fiber sample the sound absorption coefficient at 1,257 Hz for all air gap thicknesses was selected. At this frequency the increase in air gap by 10, 20, and 30 mm increased the sound absorption coefficient by 31, 61, and 64 %, respectively. Figure 15 shows the variation in the sound absorption coefficient for the different configurations at 1,257 Hz.

Noise reduction coefficient (NRC) was computed to compare the performance of the palm date fiber sample with air gap backing and perforated plate facing. Table 2 shows the data for the noise reduction coefficient for the three air gaps. From the table it can be observed that the NRC increases by increasing the air gap. The overall performance of the palm date fiber in sound absorption increases with increasing the air gap. As can be seen in the table for 250 Hz the sound absorption coefficient is the same and increases by increasing the frequency to 500 and 1,000. However, for the frequency of 2,000 Hz the sound absorption coefficient decreases

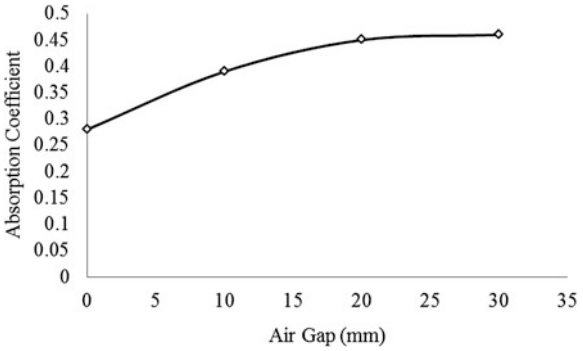

Fig. 15 Sound absorption coefficient for different air gap thicknesses at 1,257 Hz

Table 2 Noise reduction coefficient for the date palm fiber sample of different air gaps

Air gap (mm)	Noise reduction coefficient				
	250 Hz	500 Hz	1,000 Hz	2,000 Hz	NRC
10	0.06	0.08	0.27	0.46	0.218
20	0.06	0.10	0.36	0.42	0.235
30	0.06	0.11	0.42	0.37	0.240

by increasing the air gap. This is due to shift in the peak of the curves toward the lower frequency range as can be observed in Fig. 8. The peak values for the sound absorption coefficient for the 10, 20, and 30 mm are 2,000, 1,260, and 1,200 Hz, respectively. Thus for better performance of sound absorption, the date palm fiber can be used by either increasing the density or increasing the thickness of the samples.

6 Future Research Directions

Although numerous efforts have been made for the utilization of fibrous materials as acoustic absorbing materials, many issues still need more investigations.

For the future work, the following issues should be taken into consideration when using the date palm fiber for the purpose of sound absorption:

- The effect of the date palm density on the sound absorption as the sample tested in this study is of low density.
- The optimum micro-perforation that could provide good sound absorption capabilities.
- The improvement of other material properties such as fire resistance, decay, and moisture
- Resistance, etc., and their effect on sound absorption.

7 Conclusions

In this study, the suitability of using date palm fiber as sound absorption material was investigated. Experiments were conducted using impedance tubes. A constant thickness of a low density date palm sample was considered in this study. The low density of the sample is reflected in the overall sound absorption performance of the date palm fiber. An improvement in the sound absorption in the lower frequency range was achieved by backing the sample with air gap of different thicknesses of 10, 20, and 30 mm. The increase in the air gap thickness moved the peaks toward lower frequencies and improved the low frequencies absorption and above 4,500 Hz. However, this increase coincided with reduction of absorption in medium frequency range and reduction in the absorption peak. A linear relationship was found between sound absorption peaks with the frequency with a coefficient of regression of 0.99.

A further improvement in the sound absorption in the lower frequency range was achieved by facing the sample with a perforated plate. The sound absorption was further enhanced by backing the sample with air gap of different thicknesses of 10 mm, 20 mm, and 30 mm. The increase in the air gap thickness moved the peaks toward lower frequencies and improved the low frequencies absorption and above 4,000 Hz. However, this increase coincided with reduction of absorption in medium frequency range. Noise reduction coefficient increases by increasing the air gap.

Acknowledgments The authors thank the Universiti Kebangsaan Malaysia for sponsoring this research under project GGPM-2012-073.

References

1. Arenas, J.P., Crocker, M.J.: Recent trends in porous sound absorbing materials fornoise control. J. Sound Vib. **44**(7), 12–17 (2010)
2. Murali Mohan Rao, K., Mohana Rao, K.: Extraction and tensile properties of natural fibers: Vakka, date and bamboo. Compos. Struct. **77**(3), 288–295 (2007)
3. Selamet, A., Xu, M.B., Lee, I.J., Huff, N.T.: Dissipative expansion chambers with two concentric layers of fibrous material. Int. J. Veh. Noise Vib. **1**(3/4), 341–357 (2005)
4. Khristova, P., Kordsachia, O., Khider, T.: Alkaline pulping with additives of date palm rachis and leaves from Sudan. Bioresou. Technol. **96**(1), 79–85 (2005)
5. Kriker, A., Debicki, G., Bali, A., Khenfer, M.M., Chabannet, M.: Mechanical properties of date palm fibres and concrete reinforced with date palm fibres in hot-dry climate. Cem. Concr. Comp. **27**, 554–564 (2005)
6. Al-Sulaiman, F.: Evaluation of the performance of local fibers in evaporative cooling. Energ. Convers. Manage. **43**(16), 2267–2273 (2002)
7. Riahi, K., Mammoub, A., Thayer, B.: Date-palm fibers media filters as a potential technology for tertiary domestic wastewater treatment. J. Hazard. Mater. **161**, 608–613 (2009)
8. Khedari, J., Nankongnab, N., Hirunlabh, J., Teekasap, S.: New lowcost insulation particleboards from mixture of durian peel and coconut coir. Build. Environ. **39**(1), 59–65 (2004)
9. Yang, H.-S., Kim, D.-J., Kim, H.-J.: Rice straw–wood particle composite for sound absorbing wooden construction materials. Bioresour. Technol. **86**(2), 117–121 (2003)

10. Koizumi, T., Tsujiuchi, N., Adachi, A.: The development of sound absorbing materials using natural bamboo fibres. In: Brebbia C.A., De Wilde W.P. (ed) High Performance Structures and Composites 4. High Performance Structures and Materials, pp. 157–166. Witpress, (2002)
11. Ersoy, S., Kucuk, H.: Investigation of industrial tea-leaf-fibre waste material for its sound absorption properties. Appl. Acoust. **70**(1), 215–220 (2009)
12. Zulkifli, R., Nor, M.J.M., Tahir, M.F.M., Ismail, A.R., Nuawi, M.Z.: Acoustic properties of multilayer coir fibres sound absorption panel. J. Appl. Sci. **8**(20), 3709–3714 (2008)
13. Fouladi, M.H., Ayub Md., Nor M.J.M.: Analysis of coir fiber acoustical characteristics. Appl. Acoust. **72**, 35–42 (2011)
14. Maa, D.-Y.: Theory and design of micro perforated panel sound-absorbing constructions. Sci. Sinica **18**, 55–71 (1975)
15. Davern, W.A.: Perforated facings backed with porous materials as sound absorbers: an experimental study. Appl. Acoust. **10**, 85–112 (1977)
16. Maa, D.-Y.: Potential of microperforated panel absorber. J. Acoust. Soc. Am. **104**, 2861–2866 (1998)
17. Lee, F.C., Chen, W.H.: Acoustic transmission analysis of multi-layer absorbers. J. Sound Vib. **248**(4), 621–634 (2001)
18. Zulkifli, R., Nor, M.J.M., Ismail, A.R., Nuawi, M.Z., Tahir, M.F.M.: Effect of perforated size and air gap thickness on acoustic properties of coir fibre sound absorption panels. Eur. J. Sci. Res. **28**(2), 242–252 (2009)
19. Fouladi, M.H., Nor, M.J.M., Ayub, Md., Leman, Z.A.: Utilization of coir fiber in multilayer acoustic absorption panel. Appl. Acoust. **71**, 241–249 (2010)
20. Ali, M.M., Mohammed, M.O.: Palm date fibres as sound absorber. Dissertation, University of Khartoum, Khartoum, Sudan (2010)
21. Ballagh, K.O.: Acoustical properties of wool. Appl. Acoust. **48**(2), 101–120 (1996)
22. Dunn, I.P., Davern, W.A.: Calculation of acoustic impedance of multilayer absorbers. Appl. Acoust. **19**(5), 321–334 (1986)
23. Qunli, W.: Empirical relations between acoustical properties and flow resistivity of porous plastic open-cell foam. Appl. Acoust. **25**(3), 141–148 (1988)
24. Miki, Y.: 'Acoustical properties of porous materials, generalization of empirical models. J. Acoust. Soc. Jpn. **11**(1), 19–24 (1990)
25. Biot, M.A.: Theory of propagation of elastic waves in a fluid-saturated porous solid. II. Higher frequency range. J. Acoust. Soc. Am. **28**, 179–191 (1956)
26. Johnson, D.L., Koplik, J.R., Dashen, R.: Theory of dynamic permeability and tortuosity in fluid-saturated porous media. J. Fluid Mech. **176**, 379–402 (1987)
27. Attenborough, K.: The prediction of oblique-incidence behavior of fibrous absorbents. J. Sound Vib. **14**, 183–191 (1971)
28. Allard, J.F.: 'Propagation of sound in porous media'. Elsevier Applied Science, New York (1993)
29. Zhang, X.: Elastic sound absorption theory of fibrous material. Int. J. Veh. Noise Vib. **4**(3), 190–204 (2008)
30. Delany, M.E., Bazley, E.N.: Acoustical properties of fibrous absorbent materials. Appl. Acoust. **3**, 105–116 (1970)
31. Elwaleed, A.K., Mohamed, N.A.N., Nor, M.J.M., Tahir, M.F.M., Zulkifli, R.: A preliminary study on the sound absorption of date palm fibers. In: The 4th International Conference on Noise, Vibration and Comfort (NVC 2012), Kuala Lumpur, Malaysia, pp. 26–28 (2012)
32. International Organization for Standardization: ISO 10534-2: Determination of sound absorption coefficient and impedance in impedance tubes—part 2: transfer function method. Geneva, ISO (1998)
33. Fatima, S., Mohanty, A.R.: Acoustical and fire-retardant properties of jute composite materials. Appl. Acoust. **72**, 108–114 (2011)

Effect of Strain Rate on Tensile Strength and Work Hardening for Al–Zn Magnesium Alloys

N. Abdul Latif, Z. Sajuri, J. Syarif and Y. Mutoh

Abstract The effect of strain rate on mechanical behavior of Al–Zn magnesium alloys was investigated at room temperature under tensile loading with a wide range of strain rate. The quasi-static tensile test was performed in four different strain rates to obtain their effect on tensile properties, work hardening rate, strain hardening exponent, and strength coefficient using a round shape tensile specimen. Two types of Al–Zn magnesium alloys were used in this study i.e., AZ31 and AZ61 magnesium alloys. The yield stress and tensile strength of AZ31 were found to be the strain rate dependent but not so clear for AZ61. The elongations of AZ31 were approximately 15 % for all strain rate levels. The elongation for AZ31 was slightly decreased with increasing strain rate, while that for AZ61 was significantly decreased. For all strain rate levels, the work hardening rate of AZ61 was higher compared to that of AZ31. The strain hardening exponent was decreased with increasing strain rate. In contrast, the strength coefficient was increased with increasing strain rate for both alloys. The change in the fracture mode as observed from the fracture surface implies that the fracture mechanisms in AZ31 change as the strain rate increases. Mechanical properties of AZ61 and AZ31 in this study were relied to the grain size, presence of precipitate, twinning and alloying addition. While, the strain rate dependency of AZ31 and AZ61 tensile strength might be due to the critical resolved shear stress (CRSS) of slip systems.

N. Abdul Latif (✉) · Z. Sajuri · J. Syarif
Department of Mechanical and Materials Engineering,
Faculty of Engineering and Built Environment, Universiti Kebangsaan Malaysia,
43600 Bangi, Selangor DE, Malaysia
e-mail: noradila.abdlatif@gmail.com

Y. Mutoh
Department of Mechanical Engineering, Nagaoka University of Technology,
1603-1, Kamitomioka 940-2188 Nagaoka, Niigata, Japan

N. Abdul Latif
Department of Mechanics, Faculty of Mechanical and Manufacturing Engineering,
Universiti Tun Hussein Onn Malaysia, 86400 Parit Raja, Johor, Malaysia

F. L. Gaol and J. Webb (eds.), *Recent Trends in Nanotechnology and Materials Science*, Engineering Materials, DOI: 10.1007/978-3-319-04516-0_7,

1 Introduction

High specific strength and lightweight properties promote wider applications of magnesium alloys in automotive and aerospace industries. The lightweight property of magnesium alloys has attracted the manufacturer to replace component of denser materials such as steel, cast iron and aluminium for weight reduction. In addition, magnesium alloys also possess excellent mechanical, physical, and chemical properties [1–3]. However, practical use, the collision with other objects (by accident or crash) at different impact velocities could happen to the magnesium alloy components in automotive and aerospace applications. The impact could cause damage and leads to catastrophic failure of the materials. Thus, it is important in particular to identify the effect of loading rate on mechanical properties of magnesium alloys to ensure the reliability and durability.

Several studies on the effect of tensile loading rate on mechanical behavior of magnesium alloys have been reported. For example, Ahmad and Wei have investigated the tensile properties of die-cast magnesium alloy AZ91D at various strain rates. They reported that tensile strength is strain rate dependent and increases with increasing strain rate [1]. Ulacia et al. have been investigated the mechanical behavior of an AZ31 magnesium sheet at high and low strain rates at elevated temperatures [4]. They also found that the strength of the sheet increased with increasing strain rate [1, 4].

Mechanical properties of magnesium alloys are influenced by grain size, presence of precipitate hardening, texture, alloying additions, etc. [5, 6]. The Al–Mg alloys possess a high strength and formability, which are mainly due to the solid strengthening and strain hardening [7]. Similarly, aluminum content in magnesium alloys is also known to influence the strength of the material with the presence of precipitates (second-phase particles) in the microstructure by the solid solution alloying [8]. At room temperature, magnesium alloys have a limited slip system activated, while the other slips system would be present at elevated temperatures. The deformation of crystallographic basal slip and twinning for the hexagonal closed packed (h.c.p) crystal structure of magnesium alloy would occur at room temperature [9–11]. It leads better hardening of magnesium alloys with many dislocation pile ups against precipitates, grain boundaries, and twinning for delayed fracture. The difficulty of deformation is tended to the increase the dislocation density and then to induce hardening for the alloy [1, 2, 5, 12]. High strain rate was led to increase the presence of twinning and dislocation density, which are the obstacles for dislocation slip to induce a high work hardening [5]. However, details of hardening behavior under a wide range of strain rate for magnesium alloys have not yet been clarified. In this study, the effect of strain rate on tensile properties (i.e., tensile strength and elongation), work hardening behavior, strain hardening exponent, and strength coefficient of AZ31 and AZ61 magnesium alloys were investigated in detail.

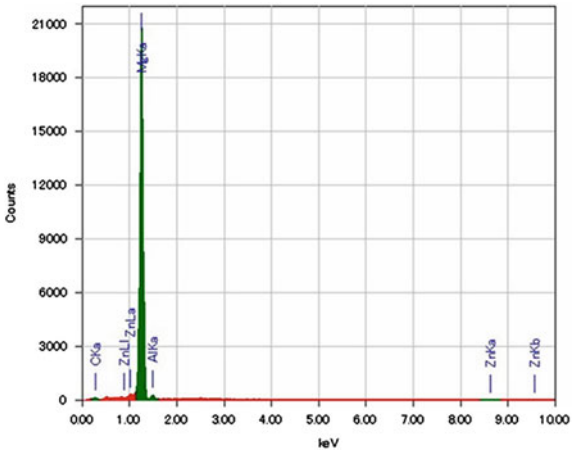

Fig. 1 EDS analysis of AZ31

2 Experimental Procedure

Two types of extruded magnesium alloys, AZ31 and AZ61, were used for the quasi-static tensile tests with various strain rates. The aluminum contents in AZ31 and AZ61 are approximately 3 % and 6 %, respectively. In both alloys, the content of zinc is approximately 1 %. EDS analysis was carried out to identify element contents of the AZ31 and AZ61 as shown in Figs. 1 and 2, respectively. The aluminum content in AZ61 was higher compared to that of the AZ31 but the zinc content was almost similar. The tensile test specimens with dumb-bell shape were cut from the extruded round bar of 16 mm in diameter. The gage length and diameter of the gage part of the specimen were 10 mm and 3 mm, respectively, as shown in Fig. 3. All specimens were polished by using 400–1,500 grit emery papers to obtain the smooth surface before the test.

A Universal Testing Machine with a capacity of 100 kN was used for the quasi-static tensile tests, as shown in Fig. 4. The tensile test specimen was fixed to the jig as shown in Fig. 5. All tests were performed at room temperature and in lab air with strain rates of 1×10^{-4} s^{-1}, 1×10^{-3} s^{-1}, 1×10^{-2} s^{-1} and 1×10^{-1} s^{-1}. The strain was measured during the test until the specimen break by using a high resolution extensometer. After the tensile tests, the fracture surfaces were observed by using a scanning electron microscope (SEM) to identify the mode of fracture.

The data (force, area of cross-section, elongation, and engineering strain) obtained from the quasi-static tensile test at room temperature were used to calculate the true stress, σ and true strain, ε. The true stress and true strain were calculated using the following Eqs. (1) and (2).

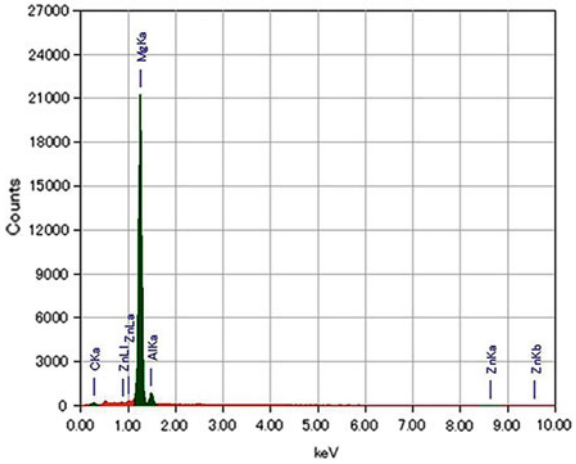

Fig. 2 EDS analysis of AZ61

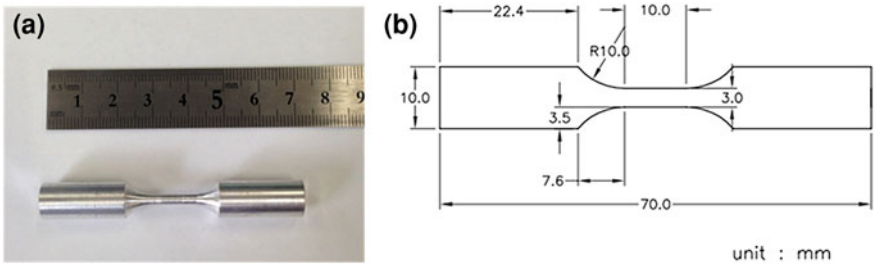

Fig. 3 Round dumb-bell specimen. **a** Macro-view of the specimen **b** dimensions of the specimen

$$\sigma = \frac{F}{A_T} \tag{1}$$

where, F is the force and A_T the area of cross-section at the force, F and

$$\varepsilon = \ln\left(1 + \frac{dL}{L_O}\right) \tag{2}$$

where dL is the elongation and L_O the original gage length.

Based on the stress and strain obtained, the work hardening rate for both the materials were identified by using the Eq. (3) [5]:

$$\frac{d\sigma}{d\varepsilon} = \frac{\sigma_2 - \sigma_1}{\varepsilon_2 - \varepsilon_1} \tag{3}$$

$d\sigma$ the increment of true stress
$d\varepsilon$ the increment of true strain.

Fig. 4 Universal testing machine with a capacity of 100 kN

By referring to the ASTM E 646-97, the tensile strain hardening exponent and strength coefficient were determined by the following power law hardening Eq. (4), which is called as Hollomon equation.

$$\sigma = K\varepsilon_p^n \tag{4}$$

where, σ is the true stress, K the strain hardening coefficient (stress intercept at $\varepsilon_p = 1$), ε_p the true plastic strain, and n the strain hardening coefficient (slope of the line) [13–16].

The plotted graph of log true σ—log true ε_p curve was considered by using the tensile data ranged between yield strength and ultimate tensile strength of the nominal stress–strain curve. Thus, the strain hardening exponent and strength coefficient can be evaluated by using the Eq. (5) [13, 14].

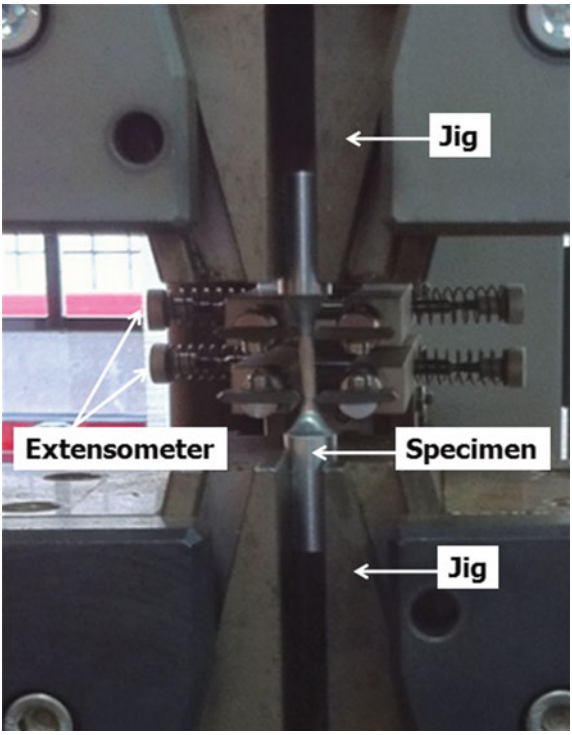

Fig. 5 Fixing a specimen to the jig

$$\log \sigma = \log K + n \log \varepsilon_p \tag{5}$$

Metallography method was applied to the AZ31 and AZ61 for providing the grain structure. Before etching, the as-received alloy sample should be polish to obtain the mirror surface. Then, the etching solution with 2 ml acetic anhydride acid, 2.2 g picric acid, 3 ml distilled water, and 35 ml ethanol was used for etching the AZ magnesium alloys. The microstructure of both the alloys was observed by using an optical microscope. The equiaxial grain structure was observed for both the AZ31 and AZ61, as shown in Fig. 6. As can be seen from the figure, the grain size of AZ31 was larger than that of AZ61. The average grain sizes of AZ31 and AZ61 were summarized in Table 1. The microstructure of AZ31 indicated significant twinning compared to that of AZ61, which would result from the extruding process. In general, the smaller grain size contributes to suppression of twinning, while it contributes to improvement of strength and ductility [9, 17].

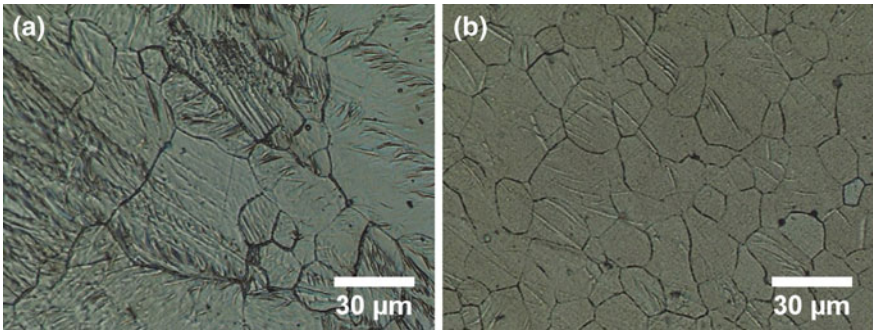

Fig. 6 Microstructure of **a** AZ31 and **b** AZ61

Table 1 Average grain size of AZ31 and AZ61

	Average grain size (µm)
AZ31	24.4
AZ61	15.0

3 Results and Discussion

Quasi-static tensile test was performed to obtain the tensile strength and hardening behavior of extruded AZ31 and AZ61 magnesium alloys. The results according to this test have cover in several subtopics in this section. The subtopics are tensile test, work hardening, strain hardening exponent, strength coefficient, and fracture surface observation. The detailed explanation of results have discussed in each subtopics.

3.1 Tensile Test

The nominal stress–strain curves of the AZ31 and AZ61 magnesium alloys are shown in Fig. 7. Relationships between yield stress, tensile strength, elongation, and strain rate are shown in Fig. 8. Tensile strength of the AZ61 magnesium alloy was higher compared to the AZ31, which might be due to the aluminum content [9]. The smaller grain size of the AZ61would also contribute to the higher tensile. The responses to the change in strain rate for both the materials were also different.

The yield stress and ultimate tensile strength of the AZ31 were increased with increasing strain rate and then became almost constant at strain rates higher than 1×10^{-2} s^{-1}, as seen from Fig. 8. This trend was similar to the result obtained by Ahmad and Wei for die-cast magnesium alloy AZ91D [1]. A study for the material of AZ31 + 0.5 Ca was done by Trojanova et al. and that for AZ61 magnesium alloys by Yoshida et al. They found a rapid rise of flow stress at higher strain rates

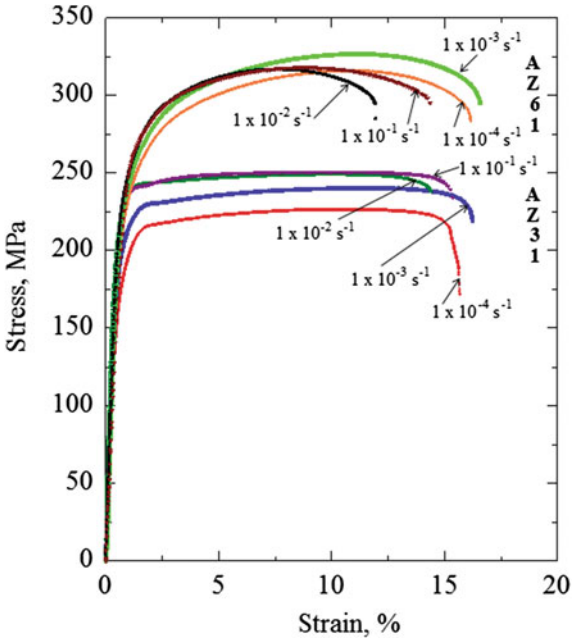

Fig. 7 Stress-strain curves for the AZ31 and AZ61

for magnesium alloys [18, 19]. Similar strain rate dependency of yield and tensile strength has been also reported by Srivatsan et al. who studied the tensile behavior of the rapidly solidified magnesium alloy [20]. This strain rate dependency might be due to the critical resolved shear stress (CRSS) of nonbasal slip systems for magnesium alloy [4, 21, 22]. The lower tensile strength was caused by the basal slip activation of CRSS at the low strain rate [22, 23]. Meanwhile, the higher tensile strength for AZ31 at high strain rate would result from the nonbasal system activated by CRSS [18, 22, 24, 25]. The elongations of AZ31 were approximately 15 % at all strain rates with some scatter.

In contrast to the case of AZ31, the tensile strength of AZ61 magnesium alloy was not significantly affected by the strain rate and almost constant regardless of strain rate with scatter. For the strain dependency of yield strength, the yield strength of AZ61 increased with increasing strain rate, which trend was almost similar to that of AZ31, as seen from Fig. 8. The AZ61 exhibited higher work hardening rate compared to that of AZ31 as shown in Fig. 7. Both yield strength and tensile strength of AZ61 were higher than those of AZ31, as seen from Fig. 8. Finer grain size and solution treatment in AZ61 would mainly contribute to the higher strength of AZ61 even less or no presence of twinning and slip in AZ61 [11]. Basal slip can easily occur in large grain size. It has been reported that the true stress increases in larger grain size due to the presence of large amount twinning, which would be induced by basal slip [26]. The contribution of twinning

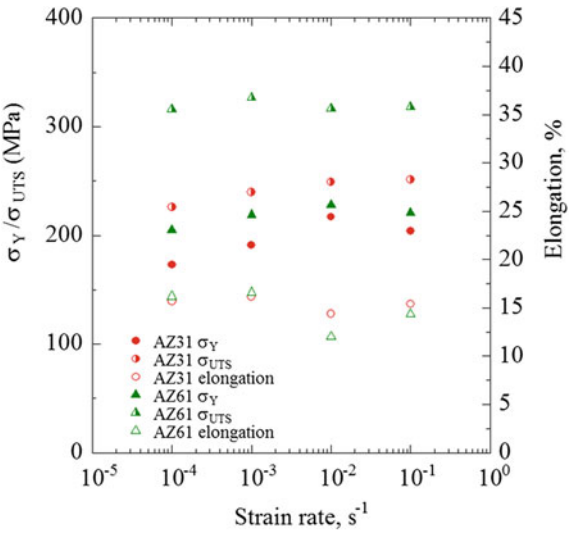

	Strain rate s^{-1}	σ_y MPa	σ_{UTS} MPa	ε %
AZ31	1×10^{-4}	173	226	15.7
	1×10^{-3}	191	240	16.2
	1×10^{-2}	217	249	14.4
	1×10^{-1}	204	251	15.4
AZ61	1×10^{-4}	205	316	16.2
	1×10^{-3}	219	327	16.6
	1×10^{-2}	228	317	12.0
	1×10^{-1}	221	318	14.4

Fig. 8 Effect of strain rate on tensile properties for the AZ31 and AZ61

deformation for AZ31 would increase with increasing the uniform total elongation, which would be the main reason for the high work hardening seen in the nominal stress–strain curve [9, 27].

The elongation of AZ61 was almost constant with some scatter regardless of strain rate similar to AZ31, while that at 1×10^{-2} s^{-1} was rather lower than those at other strain rates. The similar strain rate dependency of elongation for AZ31 has reported [10]. It is known that at higher strain rate, the dislocation movement or slip deformation cannot follow the higher rate of loading and then elongation or fracture strain could be reduced. However, in the present range of strain rate, it is speculate that since the elongations were almost constant and did not depend on strain rate, dislocation movement can follow the higher strain rate of loading. In general, the elongation might increase with decreasing the grain size [17] and with decreasing volume fraction of the second-phase particle and the inclusion [28, 29]. As seen from Table 1, the average grain size of AZ31 is about 10 μm larger than

that of AZ61. As seen from Fig. 6, the second-phase particles and inclusions were not observed for both the materials. Therefore, the elongations for both the materials were almost the same.

3.2 Work Hardening

In this study, work hardening rate was used to show the ability of work hardening for the Al–Zn magnesium alloys. The h.c.p crystal structure of magnesium alloy would influence the work hardening behavior through the effects of strain rate, temperature, texture, chemical composition, and so on [30]. Work hardening occurs due to the dislocation and twinning generation against the crystal structure of alloys [5]. Figure 9 shows the variation of true stress and work hardening rate against true strain for both the Al–Zn magnesium alloys.

Figure 9a shows the relationships between work hardening rate and true strain for the AZ31 magnesium alloy. It was found from the figure that for all the strain rate conditions, the work hardening significantly occurred in the early stage of plastic deformation. This is due to the deformation slip being hindered by the presence of twinning in the AZ31. Twinning has provided a high dislocation slip by producing more barriers into grains. Inside the twinning barrier, higher dislocation density was induced, which makes slip deformation difficult [11, 18, 26, 30]. However, the alloy has a high dislocation density would be tends to the less ductility. Thus, the hardening process was then diminished just after the yielding, which indicated the poor strain hardening behavior of the material.

In contrast, work hardening rates for the AZ61 specimens were higher compared to those of the AZ31 as found from Fig. 9b. The work hardening process in the AZ61 continued after yielding point up to the level of ultimate tensile strength. The higher work hardening rate for the AZ61 would be attributed to more dislocation pile-up due to blocking at the $Mg_{17}Al_{12}$ precipitates, twinning, and grain boundaries as compared to the AZ31 in which precipitates were very limited due to the composition of the alloy [2, 27, 30–33]. However, the work hardening rate at the strain rate of 1×10^{-1} s^{-1} for the AZ61 was found to be slightly higher at the beginning compared to those at the lower strain rates.

3.3 Strain Hardening Exponent and Strength Coefficient

In Fig. 9, the difference of work hardening rate was not clearly seen between the different strain rate levels for both the alloys. Thus, the log σ—log ε_p curve as shown in Fig. 10 was used to evaluate the strain hardening exponent and the strength coefficient for both the alloys. These values indicate to the mechanical behavior which corresponds to the stress–strain behavior after yielding. Likewise, it can be used to study the deformation mechanisms [15, 34].

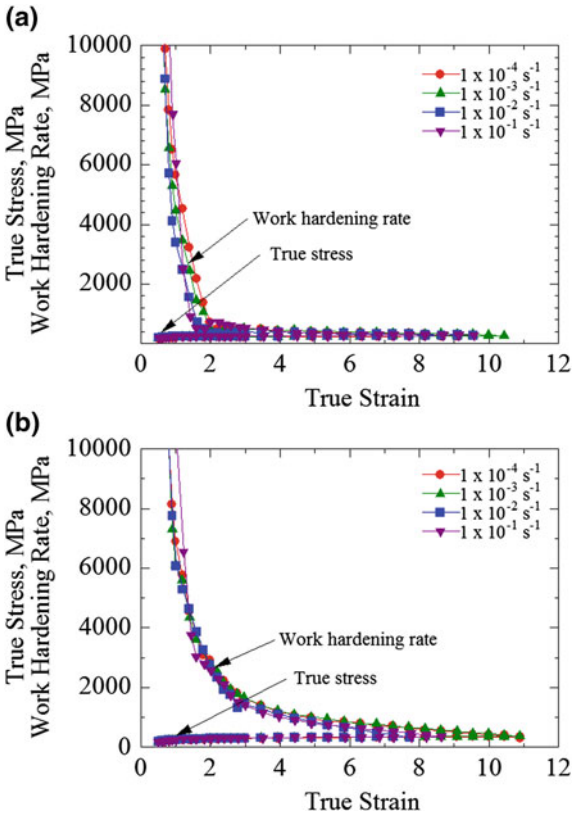

Fig. 9 Work hardening rate of **a** AZ31 and **b** AZ61

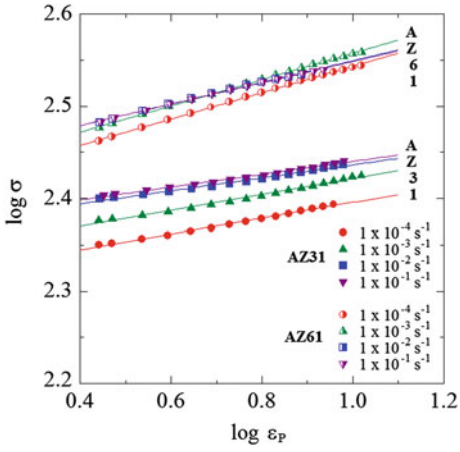

Fig. 10 The log true σ—log true ε_p curves for AZ31 and AZ61

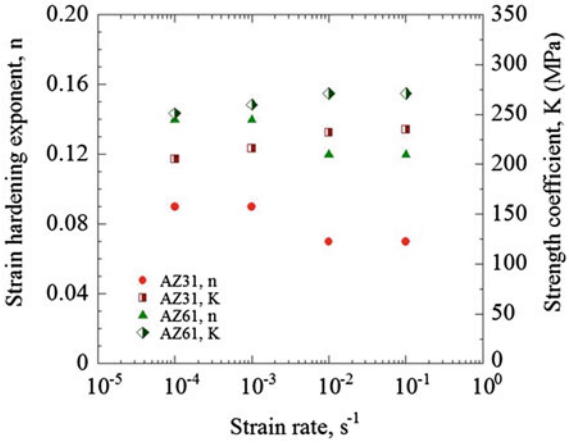

	Strain rate s^{-1}	n	K MPa
AZ31	1×10^{-4}	0.09	204.7
	1×10^{-3}	0.09	216.4
	1×10^{-2}	0.07	232.2
	1×10^{-1}	0.07	234.8
AZ61	1×10^{-4}	0.14	251.3
	1×10^{-3}	0.14	259.8
	1×10^{-2}	0.12	270.6
	1×10^{-1}	0.12	271.1

Fig. 11 Strain hardening exponent and strength coefficient of AZ31 and AZ61

The strain hardening exponent, n, and strength coefficient evaluated, K, evaluated for a wide range of strain rate are plotted as shown in Fig. 11. The strain hardening exponent marginally decreased with increasing strain rate, while the strength coefficient increased with increasing strain rate for both the alloys [35]. The larger strain hardening exponent at lower strain rate implies that the more hardening mechanism could be activated at lower strain rates, while the high strength coefficient was observed at higher strain rates for both alloys. The AZ61 seemed to be a high strength alloy with the high strain hardening exponent and strength coefficient compared to those of the AZ31. At room temperature, the hardening mechanism of both alloys would depend on the strain rate [24]. This phenomena of strain rate dependence could also explain the strain rate dependency of work hardening rate according to the dislocation collision [2, 5, 31–33]. In addition, the difficulty of dislocation slip thru the twinning boundaries would also contribute to the increase of strength with increasing strain rate [30].

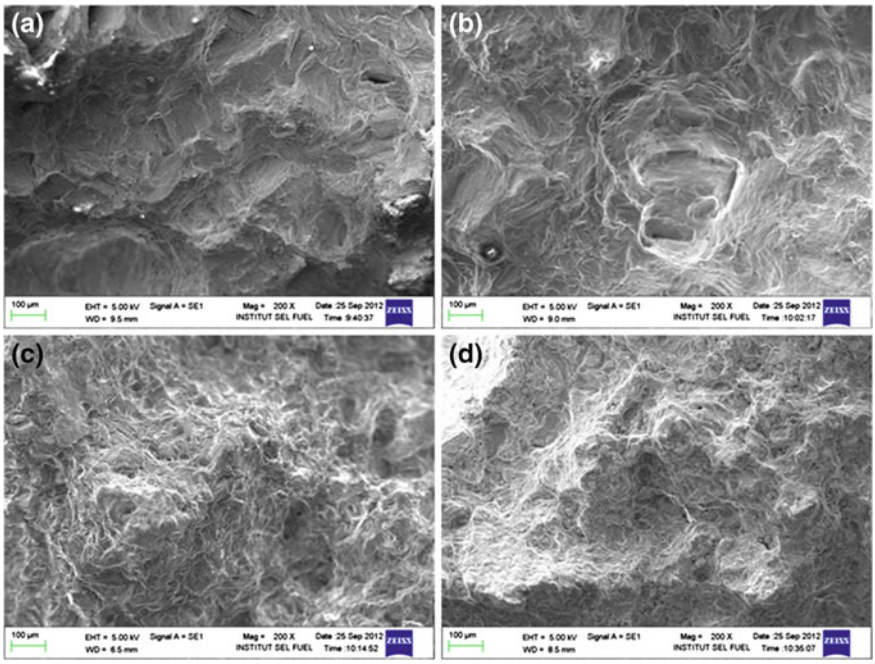

Fig. 12 Fracture surface of **a** AZ31 at strain rate of 1×10^{-4} s^{-1} **b** AZ31 at strain rate of 1×10^{-1} s^{-1} **c** AZ61 at strain rate of 1×10^{-4} s^{-1} **d** AZ61 at strain rate of 1×10^{-1} s^{-1}

3.4 Fracture Surface of Al–Zn Magnesium Alloys

Examples of SEM fractographs of the tested specimens are shown in Fig. 12a–d. The fractographs revealed that the AZ31 specimens tested at low strain rates exhibited intergranular fracture with clear surface steps as shown in Fig. 12a. These fracture steps and planar surfaces are believed to be the h.c.p. basal plane of crystal structure [36]. The surface morphology was changed in the specimens tested at high strain rate of 1×10^{-1} s^{-1} as observed in Fig. 12b where a relatively ductile mode could be observed, which implied that the fracture mechanism in the AZ31 might be changed with strain rate. Fracture surfaces of the AZ61 specimens, as seen in Fig. 12c and d, tend to indicate more ductile manner of fracture, where a large amount of dimples and microcavities could be observed. The small dimples found in AZ61 would be caused by fine grains [37]. The difference of fracture surface features between two materials would be due to less twinning deformation in AZ61 compared to that in AZ31.

4 Conclusion

Quasi-static tensile tests of extruded AZ31 and AZ61 magnesium alloys were carried out to investigate the effect of strain rate on tensile properties of magnesium alloys. Based on the results obtained, the following conclusions are summarized:

a. Tensile strength and work hardening of the AZ61 were higher compared to those of the AZ31. The higher tensile strength and work hardening in AZ61 would mainly due to the difficulty of dislocation slip thru the grain size, precipitate hardening of alloy and alloying addition.
b. Tensile strength was dependent on strain rate and significantly increased with increasing strain rate for the AZ31 but not so significant for the AZ61.
c. The yield strength of both the AZ31and the AZ61increased with increasing strain rate. The strain rate dependency of yield strength would be mainly due to the CRSS by activation of slip systems.
d. The elongations of the AZ31 and AZ61 were almost at the same level and constant regardless of strain rate.
e. Strain hardening exponent for both the alloys decreased with increasing strain rate, while the strength coefficient increased with increasing strain rate.
f. Strain hardening exponent and strength coefficient for the AZ61 were higher than those of the AZ31.
g. The fracture surface morphology of AZ31 and AZ61 indicated that the fracture occurred in ductile fracture manner. The fracture surface of the AZ61 indicated more significant influence of the h.c.p basal plane of crystal structure of magnesium alloy.

Acknowledgment The authors acknowledge the supports from the Universiti Kebangsaan Malaysia, Ministry of Higher Education Malaysia (ERGS/1/2011/TK/UKM/02/9), Nagaoka University of Technology, Fuel Cell Institute and Universiti Tun Hussein Onn Malaysia.

References

1. Ahmad, I.R., Wei, S.D.: Appl. Mech. Mater. **24–25**, 325–330 (2010)
2. Kainer, K.U.: Magnesium—Alloys and Technologies WILEY-VCH GmbH & Co. KGaA (2003)
3. Mordike, B.L., Ebert, T.: Mater. Sci. Eng. A **302**, 37–45 (2001)
4. Ulacia, I., Dudamell, N.V., Gálvez, F., Yi, S., Pérez-Prado, M.T., Hurtado, I.: Acta Mater. **58**, 2988–2998 (2010)
5. Li, B., Joshi, S., Azevedo, K., Ma, E., Ramesh, K.T., Figueiredo, R.B., Langdon, T.G.: Mater. Sci. Eng. A **517**, 24–29 (2009)
6. Pérez, P., Garcés, G., Adeva, P.: Comp. Sci. Technol. **64**, 145–151 (2004)
7. Gurugubelli, S.N., Gupta, A.V.S.S.K.S., Bhargava, N.R.M.R.: Int. J. Mater. Eng. Innovat. **3**, 32–49 (2012)

8. Agnew, S.R., Mehrotra, P., Lillo, T.M., Stoica, G.M., Liaw, P.K.: Acta Mater. **53**, 3135–3146 (2005)
9. Chamos, A.N., Pantelakis, S.G., Haidemenopoulos, G.N., Kamoutsi, E.: Fatigue Fract. Eng. Mater. Struct. **31**, 812–821 (2008)
10. Kim, W.J., Chung, S.W., Chung, C.S., Kum, D.: Acta Mater. **49**, 3337–3345 (2001)
11. Li, Y., Enoki, M.: Mater. Trans. **48**, 1215–1220 (2007)
12. Marya, M., Hector, L.G., Verma, R., Tong, W.: Mater. Sci. Eng., A **418**, 341–356 (2006)
13. ASTM E 646 – 00, United States
14. Dieter, G.E. Mechanical Metallurgy. McGraw Hill, New York (1928)
15. Kleemola, H.J., Nieminen, M.A.: Metall. Trans. **5**, 1863–1866 (1973)
16. Roesler, J., Harders, H., Beaker, M.: Mechanical Behaviour of Engineering Materials: Metals, Ceramics, Polymers and Composites. Springer, Berlin (2007)
17. Barnett, M.R.: Mater. Sci. Eng. A **464**, 8–16 (2007)
18. Trojanová, Z., Lukáč, P., Podrábský, T., Pešička, J.: Mater. Eng. **19**, 12–17 (2012)
19. Yoshida, Y., Arai, K., Itoh, S., Kamado, S., Kojima, Y.: Sci. Technol. Adv. Mater. **6**, 185–194 (2005)
20. Srivatsan, T.S., Vasudevan, S., Petraroli, M.: J. Alloy. Compd. **461**, 154–159 (2008)
21. Barnett, M.R.: Metall. Mater. Trans. A: Phys. Metall. Mater. Sci. A **34**, 1799–1806 (2003)
22. Kurukuri, S., Bardelcik, A., Worswick, M.J., Mishra, R.K., Carter, J.T.: Proc. EPJ Web Conf. (2012)
23. Styczynski, A., Hartig, C., Bohlen, J., Letzig, D.: Scripta Mater. **50**, 943–947 (2004)
24. Kapoor, R., Singh, J.B., Chakravartty, J.K.: Mater. Sci. Eng., A **496**, 308–315 (2008)
25. Zhao, F., Li, Y.L., Suo, T., Huang, W.D., Liu, J.R.: Trans. Nonferrous Metal. Soc. China (English Edition) **20**, 1316–1320 (2010)
26. Koike, J., Kobayashi, T., Mukai, T., Watanabe, H., Suzuki, M., Maruyama, K., Higashi, K.: Acta Mater. **51**, 2055–2065 (2003)
27. Barnett, M.R.: Mater. Sci. Eng., A **464**, 1–7 (2007)
28. Edelson, B.I., Baldwin, W.M.: Trans. Am. Soc. Met. **55**, 230 (1962)
29. Ohji, K., Ogura, K., Mutoh, Y.: Strength and Structure of Solid Materials. Noordhoff International Publishing, Netherlands pp. 99–113 (1976)
30. Yablinsky, C.A., Cerreta, E.K., Gray Iii, G.T., Brown, D.W. Vogel, S.C.: Metall. Mater. Trans. A: Phys. Metall. Mater. Sci. 37, 1907–1915 (2006)
31. Kapoor, R., Nemat-Nasser, S.: Mech. Mater. **27**, 1–12 (1998)
32. Kim, H.L., Chang, Y.W.: Metal. Mater. Int. **17**, 563–568 (2011)
33. Tanski, T.: Achiev. Mater. Manuf. Eng. **54**, 260–274 (2012)
34. Zhang, Z., Sun, Q., Li, C., Zhao, W.: J. Mater. Eng. Perform. **15**, 19–22 (2006)
35. Kulkarni, P., Prabhakar, S.: Proceedings of the 4th European LS-DYNA Users Conference, pp. 27–34 (2003)
36. Zhang, H.X., Wang, W.X., Wei, Y.H., Li, J.Y., Wang, J.L.: Trans. Nonferrous Met. Soc. China **12**, 1225–1233 (2011)
37. Zhou, L., Nakata, K., Liao, J., Tsumura, T.: Mater. Des. **42**, 505–512 (2012)

Surface Morphology and Nanoindentation of Low Temperature Hybrid Treated of AISI 316L

Askar Triwiyanto, Patthi Husain, Silvia Anggraeni and Mokhtar Ismail

Abstract This chapter measures surface mechanical properties of hybrid-treated layers at low temperature using nanoindentation method. The tools to characterize the treated layers including its roughness were performed by FESEM (Field Emission Scanning Electron Microscope) and USPM (Universal Scanning Probe Microscope). These hybrid-treated samples have shown an increase in hardness and elastic modulus compared to the untreated sample. Moreover, all treated samples have improvement on E/H ratio which shows a decrement to plastic deformation and degrade the disparity of properties, while maintaining the elastic range of deformation.

1 Introduction

Recently, nanotechnology has been promoted globally as a promising industry. Since the surface-to-volume ratio of a material is a key point in nanotechnology, surface engineering has become the premier position in today's manufacturing industry. The combination between surface engineering and nanotechnology is currently a focus of research issue [1].

Surface engineering itself may be defined as [2]:

> The design of surface and substrate together as a functionally graded system to give a cost-effective performance enhancement of which neither is capable on its own.

This is by definition a highly interdisciplinary activity. The successful implementation of surface engineering requires an integrated approach at the design stage, involving collaboration between design and surface engineers, as is increasingly being realized by managers in diverse industry sectors. In addition to being able to solve problems, surface engineering technologies have the ability to

A. Triwiyanto (✉) · P. Husain · S. Anggraeni · M. Ismail
Universiti Teknologi PETRONAS, Tronoh, Malaysia
e-mail: asmsceng@gmail.com

F. L. Gaol and J. Webb (eds.), *Recent Trends in Nanotechnology and Materials Science*, Engineering Materials, DOI: 10.1007/978-3-319-04516-0_8,

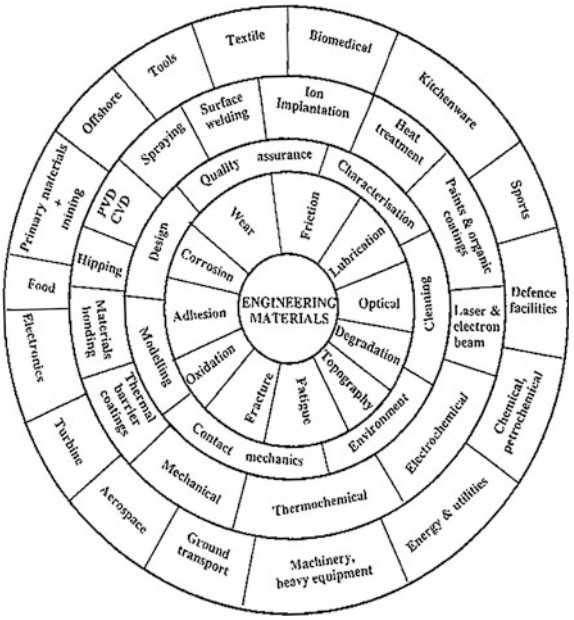

Fig. 1 Surface engineering road map: a multisectoral, interdisciplinary technology

supply *added value* and thus add profit. The aim of surface engineering is to manipulate appropriate technologies to achieve optimal surface property designs for specific applications in the most cost-effective manner [3]. Surface engineering thus has the ability to act as a bridge, transferring technology, and expertise between end-user sectors that would not normally benefit from this cross-fertilization. Figure 1 show the interaction between design, properties, surface engineering technologies, and industry sectors has been summarized using the "road map" concept [3].

On the other hand, surface and near-surface mechanical properties of thin films and coatings can be critical to their final performance. The rapidly expanding field of depth-sensing nanoindentation provides a quantitative method for mapping the mechanical properties, such as hardness and elastic modulus of the near-surface region [4]. The determination of the mechanical properties of nanostructured materials is critical to the continuing development of thin film technology. In particular, the correlations between the mechanical response, residual stress state and deposition conditions have been documented for several systems but are not well understood [5–8].

According to this issue, the nanomechanical properties studies are needed to develop a fundamental understanding of surface and interfacial phenomena on a small scale, such as the micro/nanostructures used in MEMS, NEMS, magnetic storage systems, and other industrial applications [9].

This work deals with the characterization of hybrid-treated layer on austenitic AISI 316L stainless steels using FESEM (Field Emission Scanning Electron Microscope), USPM (Universal Scanning Probe Microscope) and Nanoindentation after low temperature thermochemical treatments. By using these methods, the improvement of its mechanical properties due to the diffusion of carbon and nitrogen at low temperature treatments was confirmed. The hardness of expanded austenite is initially determined by the Oliver and Pharr method [10]. In order to achieve proper measurement, the use of very high applied load is avoided to minimize the substrate effect where higher penetration of indenter probably overtook the diffusion zone and entering the substrate bulk region.

2 Thermochemical Surface Engineering of Austenitic Stainless Steel

Austenitic stainless steels are the most popular materials in the stainless steel family used in various applications due to their excellent corrosion resistance and good forming characteristics. Nevertheless, these types of materials have low hardness as well as poor wear resistance due to the inherent austenitic structure. To overcome these problems, efforts have been made in the past decades to modify the surfaces of these materials so as to improve their surface hardness and wear resistance. Nitriding treatment was proposed by various investigators [11–15], but problems arise due to the sensitization effect caused by the formation of chromium nitrides when these materials are treated at a nitriding temperature above 500 °C [11].

Early investigations in the mid-1980s suggested that applying low temperature nitriding would suppress the formation of chromium nitrides and produce a thin nitrided layer with high hardness and acceptable corrosion resistance [12, 13]. Since then, significant progress has been made toward achieving combined improvements in wear and corrosion resistance of austenitic stainless steels by low temperature thermochemical treatments [14, 16]. The two major low temperature thermochemical processes developed for austenitic stainless steels are nitriding and carburizing [14, 17]. The former is normally carried out at temperatures below 450 °C and the later below 500 °C. The purpose of using low temperatures is to suppress the formation of chromium nitrides and carbides in the alloyed layers, such that chromium is retained in solid solution for corrosion protection [15, 18]. Hardening of the nitrided layer and the carburized layer is due to the incorporation of nitrogen and carbon, respectively, in the austenite lattice, forming a structure termed expanded austenite, which is supersaturated with nitrogen and carbon, respectively [17, 19]. More recently, a hybrid process has also been developed, which combines the nitriding and carburizing actions in a single process cycle by introducing nitrogen and carbon simultaneously into the austenite lattice to form a hardened zone comprising a nitrogen expanded austenite layer on top of a carbon

expanded austenite layer [20–22]. There exist some synergetic effects between nitrogen and carbon: Under similar processing conditions, the hybrid-treated layer is thicker, harder, and possesses better corrosion resistance than the individual nitrided layer and carburized layer.

The most popular technology used to achieve the aforementioned low temperature thermochemical treatments of stainless steels is plasma technology, namely plasma nitriding [16, 23], plasma carburizing [24, 25], and plasma hybrid treatments [21, 22]. Due to the formation of a native oxide film on stainless steel surface when exposed to air or residual oxygen before and during the treatment process, it is rather difficult to facilitate nitrogen and carbon mass transfer from the treatment media to the component surface. However, during plasma processing, due to the sputtering effects of energetic ions, the oxide film can be removed easily and effective mass transfer is obtained. This makes the plasma technology unique for surface treatment of stainless steels. During nitriding, ammonia (NH_3) in the furnace atmosphere decomposes into hydrogen and nitrogen at the surface, enabling nitrogen atoms to be adsorbed at the steel surface and to diffuse further into the steel as shown in Fig. 2. In nitrocarburizing, it is additionally necessary to have a carbonaceous gas transferring carbon to the steel surface.

An alternative is using the more conventional gaseous processes like gas nitriding [26] and gas carburizing [27]. These have proven feasible and industrially acceptable for performing low temperature nitriding and carburizing of stainless steels, provided that the component surface is activated before the gaseous process by special chemical treatments and the oxide film formed during the gaseous process is disrupted by introducing certain special gas components [26]. As it is shown in Fig. 2, the medium will determine the way in which the diffusing elements are delivered to the metal surface. A number of different media are available (solid, liquid, gas, and plasma), and a detailed account of the media used for carburizing will be given in a following section.

From these definitions it becomes clear that two main factors will govern the process, namely: the exchange or absorption reaction with the medium and the diffusion in the metal (ASM 1977). Once in the metal, the transport of the absorbed substance takes place by diffusion, and follows Fick's laws:

$$J = -D[dC/dx] \tag{1}$$

$$J = -D[\partial C/\partial x] \tag{2}$$

$$\partial C/\partial t = \left[\partial^2 C/\partial x^2\right]/\partial x^2 \tag{3}$$

where J is the flux of diffusing substance, D is the diffusion coefficient, and $\partial C/\partial x$ is the concentration gradient [27]. Therefore, the transport of the substance in solution is driven by its concentration gradient and the diffusion coefficient which, at the same time, depends on the temperature, the chemical composition, and phase structure of the substrate.

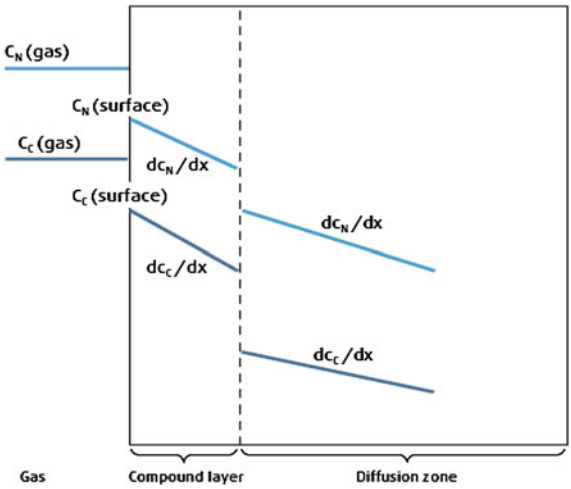

Fig. 2 Concentration of nitrogen and carbon and gradients concentration

3 Experimental Method

The substrate material used throughout the experimental series with standard metallographical surface preparation was to be made prior to the treatment were AISI 316L type austenitic stainless steel of following chemical compositions (in wt.%): 17.018 Cr, 10.045 Ni, 2.00 Mo, 1.53 Mn, 0.03 C, 0.048 Si, 0.084 P, 0.03 S, and balance Fe. This steel was supplied in the form of 2 mm thick hot-rolled plate. Samples of 20 mm $\times$ 70 mm size rectangular coupon were cut from the plate. The sample surface was ground on 320, 600, 800, 1000, 1200 grit SiC papers, and then polished using 1 μm Al_2O_3 pastes to the mirror finish. Before treating, the polished samples need to be wash with detergent and degreased in acetone and thoroughly wash in distilled water and further subject to ultrasonic cleaning in acetone for 10 min Prior to treating, the specimens were soaked in concentrated HCl (2 M) solution for 15 min duration with the purpose to remove the native oxide film that commonly forms on stainless steel and protects the metal matrix from corrosion. This oxide layer is believed to act as a barrier for diffusional nitrogen transport [28, 29]. Hybrid treatments were performed at 400 and 450 °C in a horizontal tube furnace which involving reactive gases both NH_3 (for nitriding) and CH_4 (for carburizing) for a total duration of 8 h. The gas flows were controlled by Aalborg flowmeter and the linear flow rate of gas mixture through the alumina retort were conditioned by gas mixing tank. In this system, the sample were be placed in the quartz boat of about 12 cm in the center of isothermal zone of electric resistance tube furnaces, treatment condition were set according to Table 1.

After thermochemical treatments, the specimens were quenched in water. The cross-sectioned treated specimens were first characterized by metallographic examination. To reveal the microstructure, the polished surfaces were etched in Marble's solution (4 g $CuSO_4$ + 20 ml HCl + 20 ml distilled water). The structure and morphology of specimens were characterized using FESEM (Zeiss Supra

Table 1 Treatment conditions and their corresponding layer thicknesses

Treatment	Time (h)	Temp (°C)	Gas (%)			Layer Thickness (μm)
			CH_4	NH_3	N_2	
Hybrid process 316L	8	400	5	20	75	3.421
Hybrid process 316L	8	450	5	20	75	6.425

Table 2 Instrumented hardness settings

Variable	Value
Type of experiment	Depth versus load
Type of indentor	Berkovich pyramid
Maximum load	300 mN
Maximum depth	200 nm
Dwelling time at maximum load	5 s
Loading rate	3.99 mN/s

55VP) and USPM (NanoNavi: E-sweep) to reveal 3D surface topographical profile at higher resolutions. Indentation measurements were performed by using rigid indenters. The nanoindentation test instrument model NanoTest 600 also known as depth-sensing indentation was employed to analyze a nanomechanical property. The nanoindentation test is, nowadays, commonly used to determine the local mechanical properties, as it allows measuring both the hardness and the elastic modulus at a micrometer or nanometre scale [30, 31]. When the indentation device is associated to an accurate *X–Y* motorized table, large regular indentation arrays can be performed in order to build hardness or elastic modulus maps, which is particularly interesting to study materials with heterogeneous mechanical properties [32–34]. In the NanoTest unit, forces are generated by means of a coil and magnet system located at the top of a pendulum arrangement and displacements of the probe into the surface are monitored with a sensitive capacitor plate arrangement. And in the recent measurement, the nanoindentation techniques were set as described in Table 2.

4 Results and Discussion

4.1 Layer Morphology and surface Topography Analysis

Different morphologies of harden layers as describes in Table 1 were observed as a result of the various treatment conditions and the thicknesses of the layers produced in different specimens. According to the micrograph in Fig. 3, expanded austenite layer is recognized as a featureless surface layer. For a similar treatment duration, the plasma process is reported [35, 36] to produce about 18 μm thick layer which is much higher compared to that of the present conventional hybrid treatment in horizontal tube furnace. In plasma process, the native oxide layer was

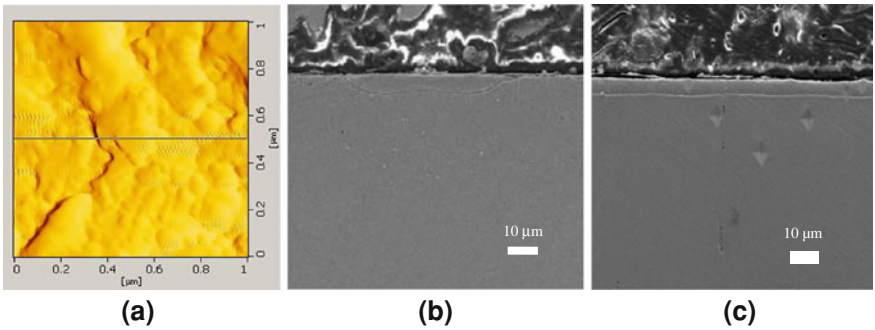

Fig. 3 **a** Top view image from USPM, Cross-sectional optical micrograph, **b** hybrid 400 °C sample and **c** hybrid 450 °C sample

removed mostly by bombardment of the plasma gas which is completely absent in conventional process. This is one of the reasons why conventional horizontal tube furnace produced small layer thickness compared to the corresponding plasma nitriding. Previous investigation revealed that nitriding at 450 °C became effective after treatment for 6 h where a continuous treated layer was produced [37].

The two specimens processed under hybrid treatment conditions as shown in Fig. 1, actually produced duplex layers although not clearly revealed in the present micrograph, this separation of dual structures is observable under SEM.

4.2 Nanoindentation Measurement Profile

The nanoindentation tests on AISI 316L untreated and hybrid-treated samples have confirmed a considerable increase in hardness 4 to 5 order and a small rise in the elastic modulus of the material after the hybrid thermochemical treatments as described in Table 3. The curves in Fig. 4 has shown that there was an agreement with previous investigation which explained the resilience and toughness of the material are of significant importance, and the ratio of hardness to elastic modulus has been reported to be a more appropriate index than the mere hardness, to rank the wear resistance [38, 39]. Meanwhile, the best tribological performances have been reported for combinations of high surface hardness and relatively low elastic modulus, to reduce the tendency to plastic deformation and reduce the mismatch of properties, while keeping deformation within the elastic range which is an agreement with recent findings as described in Table 3 due to the high nitrogen and/or carbon contents in the layers resulting from deposition process as described elsewhere [20], a characteristics relief is usually observed which results in an increase in the surface roughness.

Hardness and Elastic modulus values were determined by nanoindentation test using a Nano Test 600 apparatus from Micromaterials instruments (Wrexham, UK) equipped with Berkovich indenter.

Table 3 Roughness, indentation hardness and elastic modulus for each hybrid treatment

Treatment	Roughness, Ra (μm)	Hardness (GPa)	Elastic Modulus (GPa)	E/H
Untreated	0.12	2 ± 0.2	210 ± 2	97.22
Hybrid 400 °C	0.22	7.892 ± 0.7	167.518 ± 4.2	21.226
Hybrid 450 °C	0.28	8.471 ± 0.5	173.64 ± 3.1	20.50

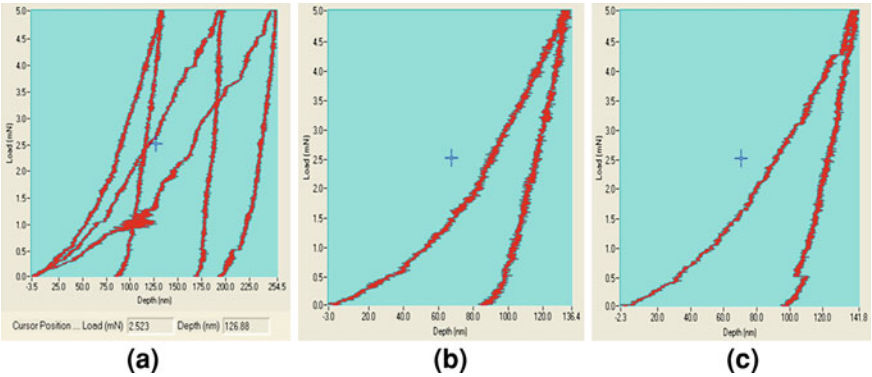

Fig. 4 Depth-sensing indentations performed on **a** hybrid-treated layer, **b** hybrid 400 °C and **c** hybrid 450 °C

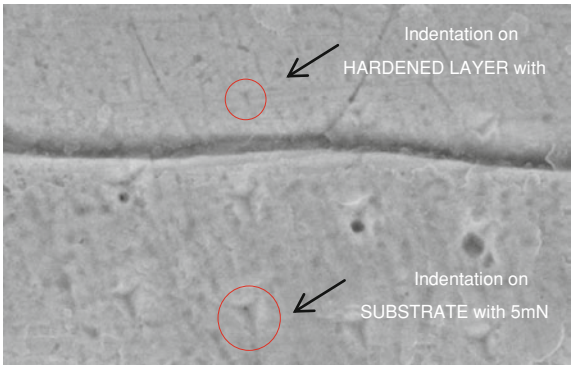

Fig. 5 Depth-sensing indentations performed on hardened layer and substrate (*red circles*)

The hardness and elastic modulus values have been extracted from the elastic unloading curves according to the equivalent indenter method. Regular arrays of 6 × 6 indentations covering a 24.32 × 21.89 μm^2 area were realized in order to probe about 3 areas which consist of substrate, interface and harden layer, respectively. Observation on Fig. 5 shows that indentation size on substrate is bigger than indentation on hardened layer which indicating that the hardened layer has higher hardness level than substrate which shows an agreement with previous work [40, 41].

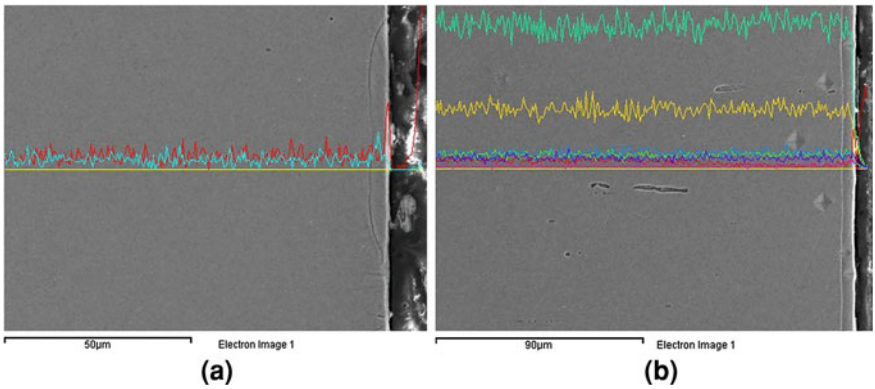

Fig. 6 Elemental profile of carbon and nitrogen on **a** hybrid 400 °C and **b** hybrid 450 °C

4.3 Elemental Profile of Nitrogen and Carbon on Surface Treated Layer

From the micrographs, it can be obviously observed that the typical nitrogen and carbon profiles measured by EDS with line scan mode for hybrid at different temperature such as 400 °C, and 450 °C. It can be seen from Fig. 6 that hybrid layers at higher temperature gave more carbon beyond nitrided layer, but some carbon remains in the subsurface layer. This figure shows that very high amount of nitrogen near the surfaces, while maximum carbon concentration appears beneath as if carbon was "pushed" to the middle of the layer by incoming nitrogen. A high nitrogen peak was detected at the surface, thus proving the push-in effect of dissolved carbon by nitrogen during the hybrid process for all specimens have also been reported in the literature [42].

5 Conclusion

The microstructure of layer produced in horizontal tube process is not uniform in thickness under the same treatment conditions according to micrograph from FESEM. The layer thickness of hybrid treated at 450 °C is 6.425 µm while at 400 °C gave much smaller thicknesses which is 3.421 µm for the same processing conditions. The elemental compositions on the surface had also changed after the hybrid process where nitrogen concentration is gradually decreasing from surface to the substrate core with distance increasing due to a low diffusion rate in the substrate at low temperature. However, some carbon remains in the subsurface layer. USPM observation of all treated surfaces shows a higher surface roughness after treatments. Nanoindentation tests reveal a higher elastic modulus and hardness for all treated samples compared to the untreated. It is found that all treated

samples have improvement of E/H ratio which show a decrement to plastic deformation and degrade the disparity of properties, while maintaining the elastic range of deformation.

Acknowledgment The authors would like to express their gratitude to Universiti Teknologi PETRONAS for supporting this research under STIRF Grant No. 49/2011.

References

1. Seal, S., Dahotre, N.B.: J. Met. **56**(1), 34 (2004)
2. D. Melford: A Study of Surface Engineering in the UK. London, CEST (1989)
3. Bell, T.: Towards a universal surface engineering road map. Surf. Eng. **16**(2), 89–90 (2000)
4. Doerner, M.F., Nix, W.D.: A method for interpreting the data from depth-sensing indentation instruments. J. Mater. Res. **1**(4), 601–609 (1986)
5. LaFontaine, W.R., Paszkiet, C.A., Korhonen, M.A., Li, G.-Y.: J. Mater. Res. **6**, 2084 (1991)
6. Vanlandingham, M.R., Dagastine, R.R., Eduljee, R.F., McCullough, R.L., Gillespie, J.W. Jr.: Compos. A Appl. Sci. Manuf. **30**, 75–83 (1999)
7. Tangyungong, P., Thomas, R.C., Houston, J.E., Michalske, T.A., Crooks, R.M., Howard, A.J.: Phys. Rev. Lett. **71**, 3319 (1993)
8. Strojny, A., Gerberich, W.W.: Submitted to MRS bulletin. In: Proceedings from Spring MRS'98
9. Bhushan, B.: Introduction to Tribology, p. 560. Wiley, NY (2002)
10. Oliver, W.C., Pharr, G.M.: An improved technique for determining hardness and elastic modulus using load and displacement sensing indentation experiments. J. Mater. Res. **7**, 1564–1583 (1992)
11. Rolinski, E.: Effect of plasma nitriding temperature on surface properties of austenitic stainless steel. Surf. Eng. **3**, 35–40 (1987)
12. Ichii, K., Fujimura, K., Takase, T.: Structure of the ion-nitrided layer of 18-8 stainless steel. Tech. Rep. Kansai Univ. **27**, 135–144 (1986)
13. Zhang, Z.L., Bell, T.: Structure and corrosion resistance of plasma nitrided stainless steel. Surf. Eng. **1**, 131–136 (1985)
14. Bell, T., Sun, Y.: Low temperature plasma nitriding and carburising of austenitic stainless steels. Heat Treat. Met. **29**(3), 57–64 (2002)
15. Sun, Y., Li, X.Y., Bell, T.: X-ray diffraction characterisation of low temperature plasma nitrided austenitic stainless steels. J. Mater. Sci. **34**, 4793–4802 (1999)
16. Rie, K.-T., Broszeit, E.: Plasma diffusion treatment and duplex treatment—recent development and new applications. Surf. Coat. Technol. **76–77**, 425–436 (1995)
17. Lewis, D.B., Leyland, A., Stevenson, P.R., Cawley, J., Matthews, A.: Metallurgical study of low temperature plasma carbon diffusion treatments for stainless steels. Surf. Coat. Technol. **60**, 416–423 (1993)
18. Sun, Y., Li, X.Y., Bell, T.: Low temperature plasma carburising of austenitic stainless steels for improved wear and corrosion resistance. Surf. Eng. **15**, 49–54 (1999)
19. Thaiwatthana, S., Li, X.Y., Dong, H., Bell, T.: Mechanical and chemical properties of low temperature plasma surface alloyed 316 austenitic stainless steel. Surf. Eng. **18**, 140–144 (2002)
20. Tsujikawa, M., Yoshida, D., Yamauchi, N., Ueda, N., Sone, T., Tanaka, S.: Surface material design of 316 stainless steel by combination of low temperature carburizing and nitriding. Surf. Coat. Technol. **200**, 507–511 (2005)

21. Sun, Y., Haruman, E.: Influence of processing conditions on structural characteristics of hybrid plasma surface alloyed austenitic stainless steel. Surf. Coat. Technol. **202**, 4069–4075 (2008)
22. Li, X.Y., Buhagiar, J., Dong, H.: Characterisation of dual S phase layer on plasma carbonitrided biomedical austenitic stainless steels. Surf. Eng. **26**, 67–73 (2010)
23. Stinville, J.C., Villechaise, P., Templier, C., Riviere, J.P., Drouet, M.: Plasma nitriding of 316L austenitic stainless steel: experimental investigation of fatigue life and surface evolution. Surf. Coat. Technol. **204**, 1947–1951 (2010)
24. Sun, Y.: Kinetics of low temperature plasma carburizing of austenitic stainless steels. J. Mater. Process. Technol. **168**, 189–194 (2005)
25. Tsujikawa, M., Noguchi, S., Yamauchi, N., Ueda, N., Sone, T.: Effect of molybdenum on hardness of low-temperature plasma carburized austenitic stainless steel. Surf. Coat. Technol. **201**, 5102–5107 (2007)
26. Gemma, K., Obtruka, T., Fujiwara, T., Kwakami, M.: Prospects for rapid nitriding in high Cr austenitic alloys. In: Bell, T., Akamatsu, K. (eds.) Stainless Steel 2000, pp. 159–166. Maney Publishing, Leeds (2001)
27. Committee on gas carburizing, ASM.: Carburizing and Carbonitriding, 1st edn. Metals Park, American Society for Metals, Ohio (1977)
28. Doerner, M.F., Nix, W.D.: A method for interpreting the data from depth-sensing indentation instruments. J. Mater. Res. **1**(4), 601–609 (1986)
29. Yamauchi, N., Ueda, N., Demizu, K., Okamoto, A., Sone, T., Oku, K., Kouda, T., Ichii, K., Akamatsu, K.: Stainless Steel 2000. In: Proceedings of International Current status seminar on thermochemical Surface Engineering Maney Publishing, Osaka, p. 247, (2001)
30. Oliver, W.C., Pharr, G.M.: J. Mater. Res. **7**, 1564 (1992)
31. Fischer-Cripps, A.C.: Nanoindentation. Springer, New York (2004)
32. Ulm, F.J., Vandamme, M., Bobko, C., Alberto Ortega, J., Tai, K., Ortiz, C.: J Am. Ceram. Soc. **90**, 2677 (2007)
33. Randall, N.X., Vandamme, M., Ulm, F.J.: J. Mater. Res. **24**, 679 (2009)
34. Tromas, C., Arnoux, M.: X. Milhet. Scripta Mater. **66**, 77 (2012)
35. Li, X.Y., Buhagiar, J., Dong, H.: Characterisation of dual S phase layer on plasma carbonitrided biomedical austenitic stainless steels. Surf. Eng. **26**, 67–73 (2010)
36. Michalski, J., Tacikowski, J., Nakonieczny, A., Wach, P.: Nitriding without the compound layer and with continuous in-process variation of the nitriding potential. Int. J. Microstruct. Mater. Prop. **2**(1) 45–53 (2007)
37. Sun, Y., Haruman, E., Malik, H., Sutjipto, A.G.E., Mridha, S., Widi, K.: Low temperature nitriding of austenitic stainless steel. Solid State Phenom. **118**, 125–130 (2006)
38. Leyland, A., Matthews, A.: On the significance of the H/E ratio in wear control: a nanocomposite coating approach to optimised tribological behaviour. Wear **246**(1–2), 1–11 (2000)
39. Leyland, A., Matthews, A.: Design criteria for wear-resistant nanostructured and glassy metal coatings. Surf. Coat. Technol. **177–178**, 317–324 (2004)
40. Mridha, Shahjahan: Gas nitriding of En40B steel with highest growth rate of the case and reduced white layer formation. Int. J. Microstruct. Mater. Prop. **2**(1), 54–63 (2007)
41. Oumarou, N., Jehl, J-Ph., Kouitat, R., Stempfle, Ph.: On the variation of mechanical parameters obtained from spherical depth sensing indentation. Int. J. Surf. Sci. Eng. **4**(4/5/6), 416–428 (2010)
42. Triwiyanto, Askar, et al.: Microstructure and nanoindentation characterization of low temperature hybrid treated layer on austenitic stainless steel. IOP Conf. Ser. Mater. Sci. Eng. **46**, 012043 (2013)